Title
Examination of the space-time variability and uncertainty of snow water storage over the Western U.S. and Andes

Author
Fang, Yiwen

Publication Date
2023

Peer reviewed|Thesis/dissertation

UNIVERSITY OF CALIFORNIA

Los Angeles

Examination of the space-time variability and uncertainty of snow water storage over the Western U.S. and Andes

A dissertation submitted in partial satisfaction of the

requirements for the degree Doctor of Philosophy

in Civil Engineering

by

Yiwen Fang

2023

ABSTRACT OF THE DISSERTATION

Examination of the space-time variability and uncertainty of snow water storage over the Western U.S. and Andes

by

Yiwen Fang

Doctor of Philosophy in Civil Engineering

University of California, Los Angeles, 2023

Professor Steven A. Margulis, Chair

Seasonal snow water is a key component of the food-energy-water nexus in many regions, supporting one sixth of the global population. Given its importance, characterizing seasonal snow is critical to close terrestrial water budgets, especially for mountainous regions where as much as 70% of the water supply for humans originates from snowmelt. However, it is an ongoing challenge to characterize snow water equivalent (SWE) from existing snow products in snow-dominated mountain regions.

In Chapter 2 of this thesis, a novel Western U.S. (WUS) snow reanalysis dataset (WUS-SR) that is continuous in space and time was developed at high-resolution (~ 500 m) over water years (WYs) 1985 to 2021. The snow dataset has been significantly verified with > 25,000 station-years of independent in situ and airborne data. Overall, WUS-SR peak SWE is well correlated against in situ peak SWE with correlation coefficient of 0.77, and against lidar-derived SWE taken near April 1st with correlation coefficients ranging from 0.75 to 0.91.

In Chapter 3, the newly derived WUS-SR dataset wass used for examining the role of snow on streamflow drought. The analysis in this thesis shows that WY 2021 stands out as an unpredictable year with extremely low streamflow in the WUS, with only moderately low upstream snow conditions. Although snowmelt played a key role in the streamflow drought, the 2021 streamflow drought was a compound event modulated by contributors linking snow, soil moisture, and streamflow.

In Chapter 4, the WUS-SR along with a previously derived Andes snow reanalysis were used as reference datasets in an intercomparison of other global products. Climatological snow storage is quantified as 269 km^3 in the WUS and 29 km^3 in the Andes from the reanalysis datasets. Existing high- and moderate-resolution products agree with the WUS-SR, whereas coarse-resolution products generally underestimate snow with large uncertainty in both WUS and Andes. Snow products with resolutions greater than 5 km did not resolve the orographic-rainshadow patterns that are important to downstream water resources. In addition to precipitation as the main driver of snow uncertainty, product spatial resolution, LSM mechanisms such as rain-snow partitioning and snowmelt generation play important roles.

This dissertation of Yiwen Fang is approved.

William W. Yeh

Dennis P. Lettenmaier

Timu Gallien

Steven A. Margulis, Committee Chair

University of California, Los Angeles

2023

Table of Contents

List of Figures

List of Tables

Acknowledgements

I would like to express my deep gratitude to Steve, for being the best and most incredible advisor. I am grateful for your extensive support, mentorship, and kindness through these years. Your encouragement helps me become a better researcher and person.

Thanks to all the coauthors for dedicating their time to brainstorming ideas, providing meaningful comments, attending regular meetings, and editing the draft. Yufei Liu, Manon von Kaenel, Dongyue Li, and Haorui Sun all provided insights into the Chapters presented here. For the other fellows in our research group, Jacob Schaperow and Maya Hildebrand, you are both terrific scientists to work with. I would like to thank my committee members for your supports and efforts over the years. I am grateful for all the colleagues at Boelter Hall 6722, and other fellows in the Department of Civil and Environmental Engineering, Geography, Atmospheric and Oceanic Science for sharing their experience and research with me. I would like to thank the staff in the Department of Civil and Environmental Engineering for all the supports.

I would like to express my special thanks to Professor Chi Li in the Department of Ethnomusicology and members of the Chinese Music Ensemble. The experience as a performer made me feel valuable and confident.

Lastly and most importantly, thanks to my family for always loving me, trusting and supporting me, and being open-minded. Thanks to my friends for your companionship, sharing happiness, and exploring the world together.

This work is supported by NSF Grant # 1641960, NASA IDS Grant # 80NSSC20K1293, and NASA Grant # 80NSSC21K1627.

Vita

EDUCATION

University of California Los Angeles (UCLA) Los Angeles, U.S.

- M.S. of Civil Engineering *June 2018*

Hohai University Nanjing, China

- B.S. of Hydrology and Water Resources *June 2017*

SELECTED PUBLICATIONS

Fang, Y., Liu, Y., & Margulis, S. A. (2022). A western United States snow reanalysis dataset over the Landsat era from water years 1985 to 2021. Scientific Data, 9(1), 1-17. *doi:10.1038/s41597-022-01768-7*

Margulis, S. A., **Fang, Y.**, Li, D., Lettenmaier, D. P., & Andreadis, K. (2019). The utility of infrequent snow depth images for deriving continuous space-time estimates of seasonal snow water equivalent. Geophysical Research Letters, 46(10), 5331-5340. *doi:10.1029/2019GL082507*

Liu, Y., **Fang, Y.**, & Margulis, S. A. (2021). Spatiotemporal distribution of seasonal snow water equivalent in High Mountain Asia from an 18-year Landsat–MODIS era snow reanalysis dataset. The Cryosphere, 15(11), 5261-5280. *doi:10.5194/tc-15-5261-2021*

Fang, Y., Y. Liu, and S. A. Margulis. 2022. Western United States UCLA Daily Snow Reanalysis, Version 1. Boulder, Colorado USA. NASA National Snow and Ice Data Center Distributed Active Archive Center. *doi:10.5067/PP7T2GBI52I2* [Dataset]

TEACHING EXPERIENCE

UCLA, Department of Civil and Environmental Engineering | Teaching Assistant/Associate

Introduction to Hydrology	Fall 2018
Applied Numerical Analysis & Modeling	Summer 2018, Spring 2019-2022

SELECTED PRESENTATIONS

Fang, Y., von Kaenel, M., Dong, L., Liu, Y., & Margulis, S. A. (2023, January). Characterizing the unusual Western U.S. snow-streamflow drought in 2021 using a novel snow reanalysis dataset and in situ measurements. In 103rd AMS Annual Meeting 2023. AMS. [Invited].

Fang, Y., Liu, Y., & Margulis, S. A. (2020, December). A New Landsat-era Snow Reanalysis Dataset over the Western United States. In AGU Fall Meeting 2020. AGU.

Fang, Y., & Margulis, S. A. (2020, October) Characterizing snowpack and snowmelt for water and hydropower management in California. In Water-Energy Technologies U.S.-China Clean Energy Research Center (CERC-WET). Berkeley, California.

CHAPTER 1

Introduction

1.1 Background and Motivation

Seasonal snow is a critical element of the terrestrial water cycle that provides freshwater to more than one billion people (~17% of the total population) globally (Immerzeel et al., 2020; Rhoades et al., 2022). Snowmelt in spring plays an important role in downstream water resources management especially for mountainous domains. For example, in the Western U.S. (WUS), 53% of runoff comes from snowmelt on average and the percentage reaches as high as 70% in snow-dominated regions (Li et al., 2017).

Knowledge of space-time variability and uncertainty of snow water storage and how it may be changing for snow-dominated regions is crucial for water availability and resources management. Intensified snow drought severity and duration have been observed in the WUS, and a low-to-no snow future is projected (Huning & AghaKouchak, 2020; Siirila-Woodburn et al., 2021). Large uncertainty of snow water storage in existing snow products have been found in the WUS, where this uncertainty propagates to the streamflow impacting water security, agriculture, and wildlife habitat (Kim et al., 2021). In the Andes, over 62% of the eastern basins have observed snow loss (Saavedra et al., 2018). Snowmelt from the Andes provides water for populated cities in Chile and Argentina, whereas the uncertainty of snow storage in the Andes has not been well characterized.

Characterizing snow water storage in mountainous regions is challenging due to 1) lack of representative in situ measurements; 2) lack of high-resolution spaceborne snow water

equivalent (SWE) measurements to capture the spatial heterogeneity and deep snowpacks; 3) large uncertainty of snow water storage from existing global products.

Bayesian snow estimation methods embedded in a data assimilation framework provide a pathway forward by leveraging remotely-sensed measurements to constrain model-based snow estimates at high resolution over large domain. The newly developed snow reanalysis framework (Margulis et al., 2015, 2019) has been verified and applied in the Sierra Nevada, the Andes, portions of the Upper Colorado River basin and High Mountain Asia (Baldo & Margulis, 2018; Cortés & Margulis, 2017; Girotto et al., 2014; Liu et al., 2021; Margulis et al., 2016).

1.2 Objective and Organization of Dissertation

The overarching objective of this dissertation is to characterize the spatial and temporal snow distribution over mountainous regions. To achieve the objective, a novel high-resolution snow dataset over the WUS is generated from water years (WYs) 1985 to 2021 using a newly developed Bayesian snow reanalysis framework (Margulis et al., 2015, 2019). In the framework, model-based snow estimates are updated by assimilation of Landsat fractional snow covered area images. Using the verified snow reanalysis dataset, the following scientific questions are addressed in this dissertation:

1) What is the role of snow in streamflow drought in the WUS?
2) How well do existing global and regional snow products characterize the spatial and temporal distribution of snow water storage in the WUS and Andes?

The dissertation is organized into five Chapters. **Chapter 2** describes the methods and inputs applied to generate the WUS snow reanalysis (WUS-SR) dataset, and verification against independent in situ snow measurements and airborne snow observatory snow estimates. The dataset generated in Chapter 2 is used to answer the above-mentioned scientific questions in

Chapter 3 and 4. **Chapter 3** quantifies the severity of snow-streamflow drought and specifically analyzes the role of snow in streamflow drought over the WUS in WY 2021 as a case study. The knowledge gained in Chapter 3 is beneficial to understand and mitigate future droughts like 2021. **Chapter 4** uses high-resolution snow reanalysis datasets including WUS-SR generated from Chapter 1 and the previously generated Andes snow reanalysis dataset (Cortes and Margulis 2017) as reference datasets to quantify snow storage uncertainties over space and time. Insights gained in Chapter 4 provide knowledge of potential uncertainties for snow-related studies and guidelines on future snow dataset generation. **Chapter 5** summarizes key findings from Chapter 2 to 4 and proposes future work to improve snow characterization with the ultimate goal of global mountain application.

1.3 Bibliography

Baldo, E., & Margulis, S. A. (2018). Assessment of a multiresolution snow reanalysis framework: A multidecadal reanalysis case over the upper Yampa River basin, Colorado. *Hydrology and Earth System Sciences*, *22*(7), 3575–3587. https://doi.org/10.5194/hess-22-3575-2018

Cortés, G., & Margulis, S. (2017). Impacts of El Niño and La Niña on interannual snow accumulation in the Andes: Results from a high-resolution 31 year reanalysis. *Geophysical Research Letters*, *44*(13), 6859–6867. https://doi.org/10.1002/2017GL073826

Girotto, M., Margulis, S. A., & Durand, M. (2014). Probabilistic SWE reanalysis as a generalization of deterministic SWE reconstruction techniques: PROBABILISTIC SWE REANALYSIS. *Hydrological Processes*, *28*(12), 3875–3895. https://doi.org/10.1002/hyp.9887

Huning, L. S., & AghaKouchak, A. (2020). Global snow drought hot spots and characteristics. *Proceedings of the National Academy of Sciences*, *117*(33), 19753–19759. https://doi.org/10.1073/pnas.1915921117

Immerzeel, W. W., Lutz, A. F., Andrade, M., Bahl, A., Biemans, H., Bolch, T., Hyde, S., Brumby, S., Davies, B. J., Elmore, A. C., Emmer, A., Feng, M., Fernández, A., Haritashya, U., Kargel, J. S., Koppes, M., Kraaijenbrink, P. D. A., Kulkarni, A. V., Mayewski, P. A., … Baillie, J. E. M. (2020). Importance and vulnerability of the world's water towers. *Nature*, *577*(7790), Article 7790. https://doi.org/10.1038/s41586-019-1822-y

Kim, R. S., Kumar, S., Vuyovich, C., Houser, P., Lundquist, J., Mudryk, L., Durand, M., Barros, A., Kim, E. J., Forman, B. A., Gutmann, E. D., Wrzesien, M. L., Garnaud, C., Sandells, M., Marshall, H.-P., Cristea, N., Pflug, J. M., Johnston, J., Cao, Y., … Wang, S. (2021). Snow Ensemble Uncertainty Project (SEUP): Quantification of snow water equivalent uncertainty across North America via ensemble land surface modeling. *The Cryosphere*, *15*(2), 771–791. https://doi.org/10.5194/tc-15-771-2021

Li, D., Wrzesien, M. L., Durand, M., Adam, J., & Lettenmaier, D. P. (2017). How much runoff originates as snow in the western United States, and how will that change in the future? *Geophysical Research Letters*, *44*(12), 6163–6172. https://doi.org/10.1002/2017GL073551

Liu, Y., Fang, Y., & Margulis, S. A. (2021). Spatiotemporal distribution of seasonal snow water equivalent in High Mountain Asia from an 18-year Landsat–MODIS era snow reanalysis dataset. *The Cryosphere*, *15*(11), 5261–5280. https://doi.org/10.5194/tc-15-5261-2021

Margulis, S. A., Cortés, G., Girotto, M., & Durand, M. (2016). A Landsat-Era Sierra Nevada Snow Reanalysis (1985–2015). *Journal of Hydrometeorology*, *17*(4), 1203–1221. https://doi.org/10.1175/JHM-D-15-0177.1

Margulis, S. A., Fang, Y., Li, D., Lettenmaier, D. P., & Andreadis, K. (2019). The Utility of Infrequent Snow Depth Images for Deriving Continuous Space-Time Estimates of Seasonal Snow Water Equivalent. *Geophysical Research Letters*, *46*(10), 5331–5340. https://doi.org/10.1029/2019GL082507

Margulis, S. A., Girotto, M., Cortés, G., & Durand, M. (2015). A Particle Batch Smoother Approach to Snow Water Equivalent Estimation. *Journal of Hydrometeorology*, *16*(4), 1752–1772. https://doi.org/10.1175/JHM-D-14-0177.1

Rhoades, A. M., Hatchett, B. J., Risser, M. D., Collins, W. D., Bambach, N. E., Huning, L. S., McCrary, R., Siirila-Woodburn, E. R., Ullrich, P. A., Wehner, M. F., Zarzycki, C. M., & Jones, A. D. (2022). Asymmetric emergence of low-to-no snow in the midlatitudes of the American Cordillera. *Nature Climate Change*, *12*(12), Article 12. https://doi.org/10.1038/s41558-022-01518-y

Saavedra, F. A., Kampf, S. K., Fassnacht, S. R., & Sibold, J. S. (2018). Changes in Andes snow cover from MODIS data, 2000–2016. *The Cryosphere*, *12*(3), 1027–1046. https://doi.org/10.5194/tc-12-1027-2018

Siirila-Woodburn, E. R., Rhoades, A. M., Hatchett, B. J., Huning, L. S., Szinai, J., Tague, C., Nico, P. S., Feldman, D. R., Jones, A. D., Collins, W. D., & Kaatz, L. (2021). A low-to-no snow future and its impacts on water resources in the western United States. *Nature Reviews Earth & Environment*, *2*(11), Article 11. https://doi.org/10.1038/s43017-021-00219-y

CHAPTER 2

A western United States snow reanalysis dataset over the Landsat era from water years 1985 to 2021

Water stored in mountain snowpacks (i.e., snow water equivalent, SWE) represents an important but poorly characterized component of the terrestrial water cycle. The Western United States snow reanalysis (WUS–SR) dataset is novel in its combination of spatial resolution (~500 m), spatial extent (31° – 49° N; 102° – 125° W), and temporal continuity (daily over 1985 – 2021). WUS–SR is generated using a Bayesian framework with model-based snow estimates updated through the assimilation of cloud-free Landsat fractional snow-covered area observations. Over the WUS, the peak SWE verification with independent in situ measurements show correlation coefficient, mean difference (MD), and root mean squared difference (RMSD) of 0.77, -0.15 m, and 0.28 m, respectively. The effects of forest cover and Landsat image availability on peak SWE are assessed. WUS–SR peak SWE is well correlated (ranging from 0.75 to 0.91) against independent lidar-derived SWE taken near April 1st, with MD < 0.15 m and RMSD < 0.38 m. The dataset is useful for characterizing WUS mountain snow storage, and ultimately for improving snow-derived water resources management.

2.1 Background & Summary

Water stored in seasonal snowpacks, typically expressed in the form of snow water equivalent (SWE), provides a key resource relevant to water supply, hydropower generation, agricultural irrigation, river navigation, and urban usage in many areas of the globe. In the Western U.S. (WUS) it is estimated that more than half of runoff comes from seasonal snowmelt (Li et al., 2017; Sturm et al., 2017). Knowledge of SWE and its space-time variability impacts food, water and energy security, the financial stability of hydropower utilities, and public safety (Hamilton et al., 2020; Huning & AghaKouchak, 2020a; Yan et al., 2020).

In situ SWE data, even in the WUS where it is arguably most readily collected operationally, remains extremely sparse. Moreover, snow exhibits significant spatial heterogeneity due to variability in snowfall, redistribution and ablation controlled by local meteorological conditions, landcover, forest cover, and other physiographic characteristics (Larson et al., 2009), especially in mountainous regions with high terrain complexity. The in situ snow stations that do exist are typically located in forest clearings, mid-elevations and flat terrain that do not necessarily sample the underlying heterogeneity of SWE (Molotch & Bales, 2006; Nolin et al., 2021). Hence, in situ networks tend to provide an incomplete picture of the spatial patterns of SWE and how point-scale SWE integrates to basin-scale water volumes.

Remotely-sensed (satellite or airborne) observations of snow provide the potential to sample spatially-distributed characteristics of snow. The historically available satellite-borne measurements most closely related to SWE use Passive Microwave (PM, e.g., AMSR-E, SSMI) measurements to infer SWE or snow depth. However, PM measurements are typically obtained at coarse resolutions (tens of kilometers and thus incapable of resolving finer scale heterogeneity) and are highly sensitive to snowpack stratigraphy and microstructure, wet snow,

and forest coverage (introducing significant uncertainty and bias into SWE estimates (Andreadis & Lettenmaier, 2006). Recent and future airborne and spaceborne concepts aim to measure snow depth (from lidar, Markus et al., 2017; T. H. Painter et al., 2016; photogrammetry; radar, Lievens et al., 2019), or SWE (from P-band, Yueh et al., 2018; C-band; X-band, Shi & Dozier, 2000; Ku-band radar, Nghiem & Wu-Yang Tsai, 2001). These newer methods show promise but cannot yet provide a long-term spatially-distributed SWE record.

To leverage remotely-sensed and in situ datasets relevant to snow processes, data assimilation combined with snow and land surface models (LSMs) can be used to constrain model estimates based on snow related observations. Global reanalysis products including ERA5 (Hersbach et al., 2020), ERA5-land (Muñoz-Sabater et al., 2021), JRA55 (Kobayashi et al., 2015), GLDAS (Rodell et al., 2004), MERRA2 (Gelaro et al., 2017), and GlobSnow v3.0 (Luojus et al., 2021) estimate terrestrial snow accumulation and melt with commonly used LSMs (e.g., VIC, SiB, Catchment, Noah) at scales of ~ 0.1° to 1°. Though coarse resolutions are typical in global applications, they do not provide the desired resolution to capture spatial variations, especially in complex terrain (Wrzesien et al., 2019). Additionally, several studies have found large uncertainties in SWE volumes derived from various input forcings and models applied over global snow covered mountains (Kim et al., 2021; Xu et al., 2019). Snow-focused products over the U.S. using data assimilation include the Snow Data Assimilation System (SNODAS, National Operational Hydrologic Remote Sensing Center, 2004) product and the University of Arizona SWE dataset (UA, Zeng et al., 2018). SNODAS daily SWE estimates are available from 2004 at the spatial resolution of 1 km × 1 km. UA daily SWE estimates start from 1982 at the spatial resolution of 4 km × 4 km. Hence, SNODAS has a more limited temporal coverage (less than 20 years), and UA is at relatively coarse resolution that can be suboptimal for assessing

spatial variability in mountainous domains. In the mountainous WUS, historical space–time continuous snow estimates at high to moderate resolution and with low uncertainty are needed.

To fill this gap, we use a Bayesian data assimilation approach that leverages high-resolution remotely-sensed visible and near infrared (Vis-NIR) measurements that provide information on fractional snow-covered area (fSCA) and how its seasonal evolution is related to SWE. Specifically, the approach yields a new snow reanalysis dataset across the WUS (Fig. 2.1) over the Landsat–era (water years (WYs) 1985 to 2021). The dataset is publicly available at National Snow and Ice Data Center (https://doi.org/10.5067/PP7T2GBI52I2, Fang et al., 2022). The daily snow reanalysis framework accounts for a priori uncertainties in meteorological forcings and other snow model parameters and reduces the uncertainty via a Bayesian data assimilation approach as described in more detail in the Methods section. The snow reanalysis SWE estimates are verified against independent in situ SWE measurements and lidar-based SWE products. Previous applications of the method over the Sierra Nevada have demonstrated the ability to characterize historical snow droughts, characterize snowfall estimates from SWE accumulation patterns, and improve streamflow predictions (Huning & AghaKouchak, 2020b; Li et al., 2019; Margulis, Cortés, Girotto, Huning, et al., 2016; Pflug et al., 2022).

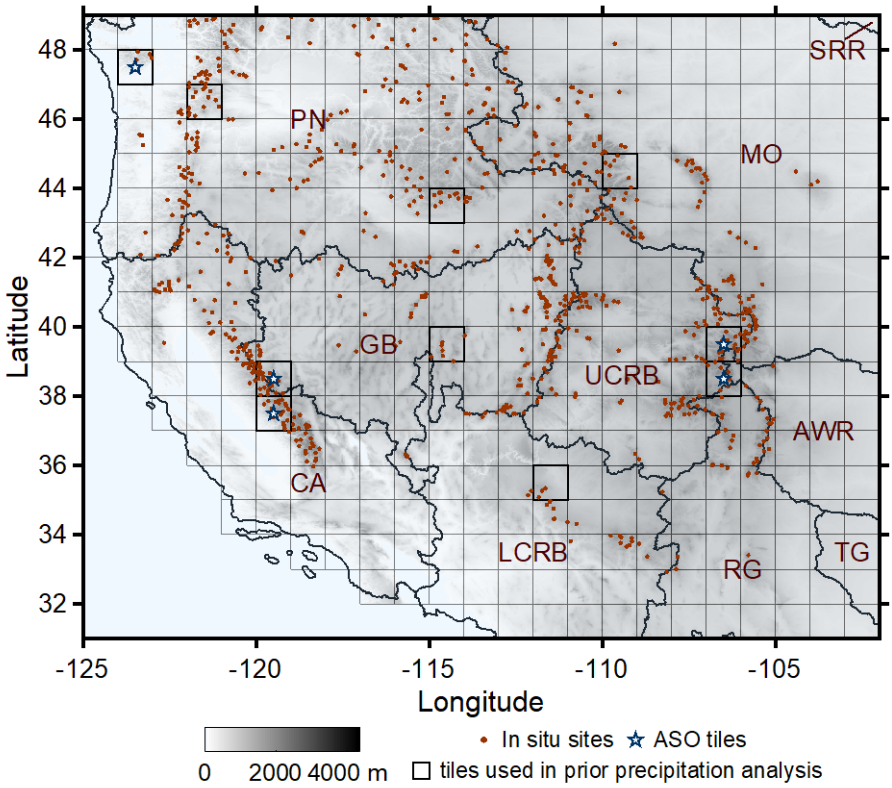

Figure 2.1 Map of elevation (meters) over the WUS domain with snow reanalysis tiles (1° × 1° squares) and Hydrologic Unit Codes 2 (HUC2) basins. HUC2 basins include California (CA), Pacific Northwest (PN), Great Basin (GB), Upper Colorado River Basin (UCRB), Missouri (MO), and other basins, i.e., Lower Colorado River Basin (LCRB), Rio Grande (RG), Texas Gulf (TG), Arkansas-White-Red (AWR), and Souris-Red-Rainy regions (SRR). The tiles highlighted in bold black outlines (in total 10) are used for prior precipitation uncertainty analysis as described in the Section 2.2. Snow Telemetry network (SNOTEL) sites and tiles with ASO SWE estimates (used for verification) are illustrated with red dots and white stars, respectively.

2.2 Methods

2.2.1 Snow Reanalysis Framework

A Bayesian "snow reanalysis" framework (Margulis, Cortés, Girotto, & Durand, 2016; Margulis et al., 2015; Margulis, Liu, et al., 2019, Fig. 2.2) is applied to generate a new Landsat-

era dataset over the WUS, herein referred to as the Western U.S. – Snow Reanalysis (WUS–SR). The dataset contains space–time continuous SWE and fractional snow-covered area (fSCA) estimates constrained by remotely-sensed (Landsat) fSCA using a particle batch smoother (PBS) data assimilation technique.

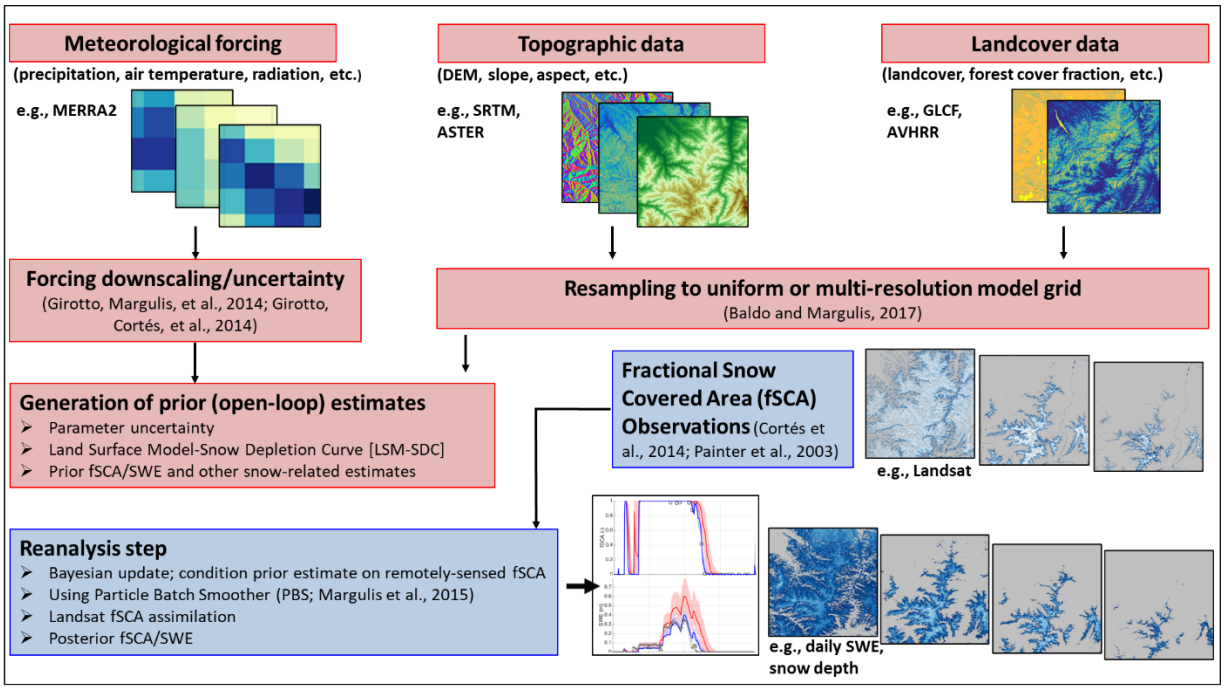

Figure 2.2 Flowchart for the Bayesian snow reanalysis framework used to generate the WUS–SR dataset (adapted from Margulis, Liu, et al. (2019)).

The snow reanalysis framework generates an ensemble of (equally likely) prior snow estimates using a land surface model (LSM) driven by meteorological forcing, topographic data and landcover data (red boxes in Fig. 2.2). Uncertainty is expressed via perturbations related to precipitation (snowfall), the snow depletion curve and snow albedo in each ensemble member (described in the Uncertainty Parameters and Measurement Error section). The reanalysis step assimilates Landsat-derived fSCA measurements to provide posterior snow estimates (blue boxes in Fig. 2.2). More specifically, the a priori (equal) weights are updated to posterior weights that reflect the likelihood that a given ensemble member fits the fSCA measurements (Margulis, Liu,

et al., 2019). The posterior weights, when combined with the prior ensemble estimates (e.g., SWE) can be used to derive posterior estimates (ensemble statistics) of the relevant states. The resulting posterior SWE and fSCA make up the published dataset.

While the snow reanalysis framework could be applied with any LSMs and their static and dynamic model inputs, in creating the WUS–SR, we use the same setup as described in Margulis, Liu, et al. (2019). In summary, a spatially-distributed version of the SSiB–SAST LSM (Sun & Xue, 2001; Xue et al., 2003; Sun et al., 1999) using the BATS (Dickinson et al., 1993) snow albedo model and coupled with the Liston (2004) Snow Depletion Curve (SDC) model is used. The SSiB–SAST LSM models a three-layer snowpack when snow depth is above 5 cm and uses a one-layer scheme when snow depth is below 5 cm. SWE at each layer is computed by mass balance with components including snowfall, rainfall, snowmelt, runoff and evaporation at the snow surface layer (Xue et al., 2003). Snow density, and therefore snow depth, is determined by the SAST compaction process as described in Sun & Xue (2001). For computational reasons, a uniform spatial resolution of 16 arcseconds (~500 m) is chosen with hourly outputs aggregated to the daily time step using an ensemble of 50 members. The SDC provides the mechanism whereby modeled estimates of SWE (and its sub-grid heterogeneity) provide predicted estimates of fSCA. For the reanalysis, the LSM–SDC model is applied separately at each pixel to the bare snow and forest covered fractions. It is assumed that Landsat sensors cannot see snow under the forest canopy. Therefore, only the predicted fSCA over bare soil is compared to the Landsat fSCA measurements in the assimilation step for each grid, while the update is applied to both bare and forested pixel fractions to obtain the grid-averaged SWE (Margulis, Liu, et al., 2019). The Bayesian update is applied in a batch over one WY at a time, where the batch of fSCA

measurements from that year are used together to derive the posterior weights and estimates. Table 2.1 summarizes the models and methods used in the snow reanalysis framework.

Table 2.1 Modules used in the snow reanalysis framework

	Model/ Methods	Notes
Prior step	SSiB-SAST	Land Surface Model (LSM) framework; surface (snow) energy balance fluxes; BATS snow albedo module
	Liston Snow Depletion Curve (SDC)	Sub-grid distribution and pixel averaged SWE, ablation, and fSCA
Posterior step	Data assimilation (PBS)	Ensemble-based Bayesian updated via assimilation of Landsat fSCA measurements

2.2.2 Land Surface Model Inputs

To generate the WUS–SR dataset, globally-available datasets are used as inputs. This includes the MERRA2 (Gelaro et al., 2017) near-surface meteorological forcing data, 30-m Shuttle Radar Topography Mission (SRTM, Farr et al., 2007) digital elevation model (DEM) for topographic data (with gaps filled by the Advanced Spaceborne Thermal Emission and Reflection, ASTER (NASA, 2001), version 2), 1-km Advanced Very High Resolution Radiometer (AVHRR, Hansen et al., 2000) landcover data and 30-m Global Land Cover Facility (recently updated to the Landsat Tree Canopy Version 4, TCC, Sexton et al., 2013) forest cover fraction data. The TCC data is available in 2000, 2005, 2010, and 2015 where each timestamped year represents multi-year average forest cover conditions during that period. Rather than implementing time-varying forest cover, the time-averaged forest cover over these 4 composites is applied for the whole reanalysis period. All inputs are downscaled or aggregated to the chosen model resolution. For example, the 1-km AVHRR dataset is first interpolated to the 30 m

resolution of the raw SRTM DEM at the nearest grid and then aggregated to the 480-m model resolution.

The meteorological forcings used in this dataset include 2-m air temperature, 2-m specific humidity, 10-m zonal and meridional wind speed, surface pressure, surface precipitation, and surface downwelling shortwave (Margulis, Liu, et al., 2019). The raw MERRA2 precipitation is perturbed to account for the expected bias and uncertainty in snowfall inputs (see more detail in the Uncertainty Parameters and Measurement Error section). In addition to precipitation, the bias and uncertainties of MERRA2 air temperature, dew point temperature (computed from MERRA2 specific humidity), and shortwave radiation are represented via ensemble perturbations. Hourly snowfall is computed by downscaled and bias-corrected air temperature and precipitation using a rain–snow threshold of 2°C. When air temperature is below the threshold, precipitation is classified as snowfall. Table 2.2 summarizes the static and dynamic inputs used to generate the dataset, as well as assimilated data described in the next section.

Table 2.2 Static and dynamic model inputs and assimilated data

Inputs	Dataset	Resolution
Static Inputs	SRTM	1 arcsecond × 1 arcsecond
	ASTER DEM	1 arcsecond × 1 arcsecond
	AVHRR landcover	1 km × 1 km
	GLCF forest cover	30 m × 30 m
Meteorological Forcing	MERRA2	0.5° × 0.625°
Assimilated Data	Landsat Imagery	30 m × 30 m

2.2.3 Assimilated Landsat fSCA Data

The timeseries of derived Landsat fSCA (raw resolution of ~30 m aggregated to 16 arcseconds), over the course of a WY is used as the measurement constraint in the Bayesian particle batch smoother (PBS) update. The retrieval of Landsat fSCA is obtained through applying linear spectral unmixing methods described in Painter et al. (2003) and Cortés et al. (2014) using Vis-NIR reflectance measured from three Landsat satellites: 1) Landsat 5 Thematic Mapper (TM) from 1985 to 2011; 2) Landsat 7 enhanced Thematic Mapper (ETM +) from 1999 to present, and 3) Landsat 8 Operational Land Images (OLI) from 2013 to present. Orbital characteristics of the Landsat platform provide swath images every 16 days (~23 images per year). Adjacent swaths contain some overlap such that some locations may have up to ~46 fSCA images from a single satellite per year. This is the typical number of available measurements from 1985–1999 (when only Landsat 5 is available) and in 2012 (when only Landsat 7 is available). In the other years, where two satellites are available (i.e., 1999–2011 and 2013–present), the number of available measurements is doubled. The failure of Landsat 7 Scan Line Corrector (starting in 2003) removes ~22% of its image areas, thus reducing the number of measurements per year (USGS(USGS, 2004)). However, the number of measurements described above provide only an upper limit on those used in the WUS–SR. Cloud contamination can significantly reduce the number of available (assimilated) measurements. Following the cloud screening methods described in Margulis, Liu, et al. (2019) and Liu et al. (2021), the internal Landsat cloud mask is used to attempt to exclude images with cloud cover fraction greater than 40%. For those images included, the internal cloud masks are used to screen out any cloudy pixels. Thus, areas identified as contaminated by clouds are removed before assimilation which reduces the available number of measurements. Though errors introduced by omission or

commission are inevitable, they are implicitly accounted for in the snow reanalysis framework as described in the Section 2.2.4.3 section below.

Fig. 2.3 shows that the total numbers of cloud-free fSCA measurements are much fewer in WYs 1992 and 2012 when only one Landsat platform is available over 10 months of the WY compared to WYs 2002 and 2018 when two Landsat satellites are available over the full WY. The number of available fSCA measurements is associated with satellite swaths that may cause spatial artifacts in posterior estimates within a WY. Grid cells with no fSCA measurements (no assimilation) or limited fSCA measurements may yield inconsistent results with grid cells that have abundant fSCA measurements. In the PN, spatial artifacts in the SWE estimates are more frequently observed when only one Landsat is available, where cloudy days are more common in the melting season. The method is capable of jointly assimilating other fSCA data (e.g., MODIS, Margulis, Liu, et al., 2019) or other relevant snow data (e.g., snow depth, Margulis, Fang, et al., 2019). The dataset presented herein is chosen to use Landsat-only data to provide a long-term homogeneous snow reanalysis product.

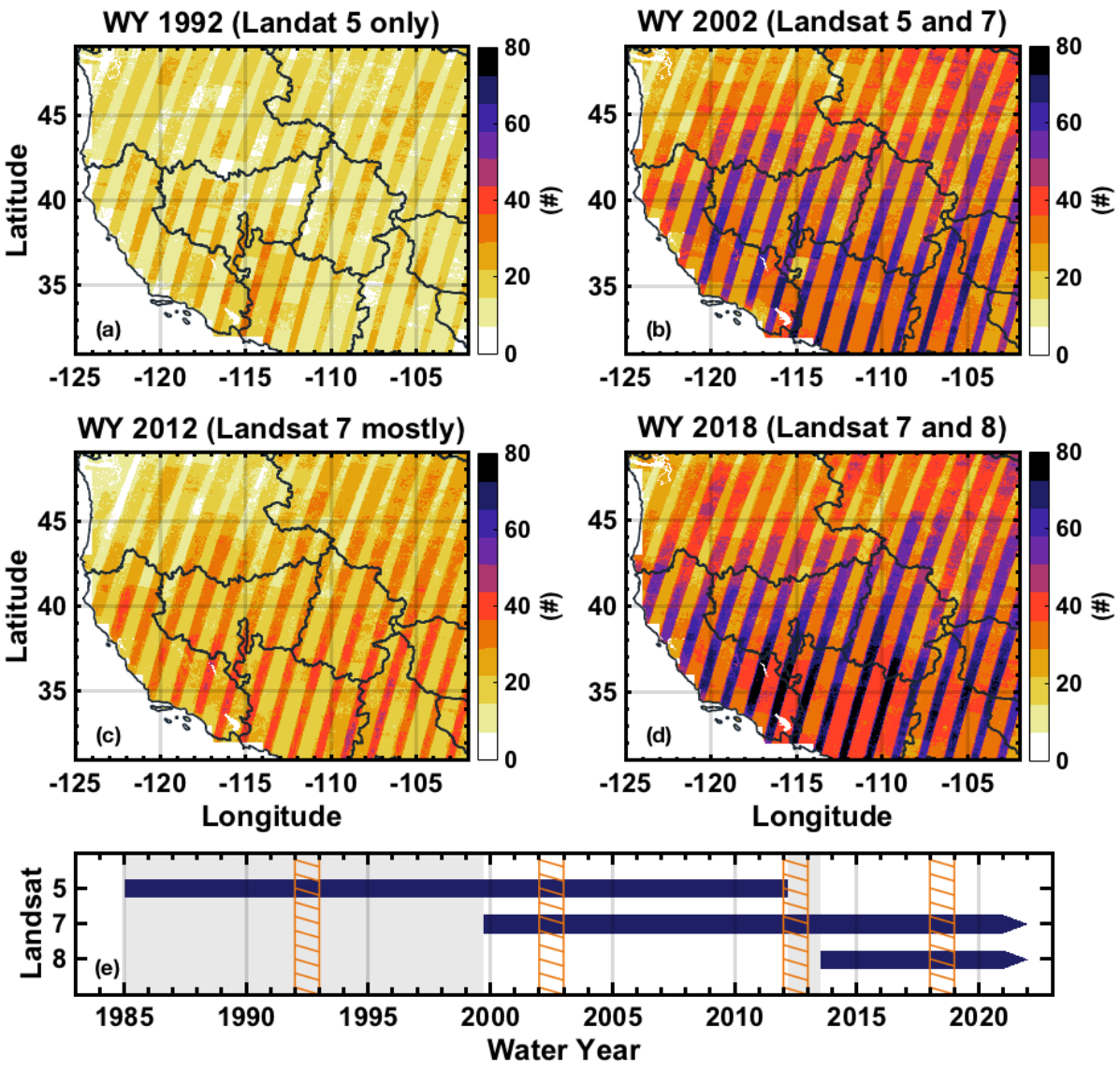

Figure 2.3 Illustration of the number of cloud-free Landsat measurements used in the WUS–SR for four WYs (top four panels) and Landsat mission timelines (bottom panel). Landsat images with diagnosed cloud fractions of 40% are excluded entirely and those will less than 40% use the Landsat cloud mask to screen out cloudy measurements. The four illustrative WYs include: (**a**) WY 1992 and (**c**) 2012 when one Landsat satellite is in orbit, and (**b**) WY 2002 and (**d**) 2018 when two Landsat satellites are in orbit. The stripes showing a larger number of measurements are the overlapping areas between adjacent Landsat tiles. The temporal coverage of measurements in (**e**) shows the Landsat 5, 7 and 8 mission timelines. Periods with only one Landsat satellite are shaded with a gray background. The orange hatched areas indicate the four WYs present in maps in the top panels.

2.2.4 Uncertainty Parameters and Measurement Error

The ensemble Bayesian framework described above is applied by considering and modeling key sources of uncertainty and error. These include uncertainty in meteorological inputs and model parameters controlling snow albedo and sub-grid distribution, and fSCA measurement errors as described in more detail below and which follow those in Margulis, Liu, et al. (2019).

2.2.4.1 Perturbed Meteorological Forcings

The a priori meteorological forcing uncertainties are embedded in the prior ensemble via perturbations to the nominal (MERRA2) inputs using parameters randomly generated from specified distributions. The uncertainty and bias correction models used are similar to those that have been successfully applied to the Sierra Nevada (Margulis, Cortés, Girotto, & Durand, 2016), Andes (Cortés & Margulis, 2017), and High Mountain Asia (Liu et al., 2021) to downscale and perturb forcings. Forcing downscaling uses a topographic correction approach following Girotto, Margulis, et al. (2014). The raw MERRA2 forcings are first (bilinearly) interpolated to the snow reanalysis grid followed by an elevation correction using differences between the (coarser resolution) MERRA2 and (higher resolution) reanalysis DEMs. Downscaled precipitation, air temperature, dew point temperature and shortwave inputs are bias-corrected and perturbed using the formulation (Margulis, Liu, et al., 2019):

$$PPT_j = b_j \cdot PPT_{MERRA2} \quad (1)$$

$$T_{a,j} = T_{a,MERRA2} + \varepsilon_{T_{a,j}} \quad (2)$$

$$T_{d,j} = T_{d,MERRA2} + \varepsilon_{T_{d,j}} \quad (3)$$

$$SW_j = \left(1 - \gamma_j\right) \cdot SW_{MERRA2} \quad (4)$$

where PPT, T_a, T_d, and SW represent the precipitation, air temperature, dew point temperature, and shortwave radiation forcings respectively, the subscript j represents the perturbed forcing realization within the ensemble and $MERRA2$ represents the downscaled MERRA2 forcings using the downscaling described above. The random variable b represents a lognormally distributed multiplicative precipitation perturbation. The random variable ε_{Ta} and ε_{Td} represent normally distributed additive error perturbations of air temperature and dew point temperature, respectively. The random variable γ represents a normally distributed multiplicative shortwave perturbation that varies with solar index (*SI,* ratio of MERRA2 solar radiation over clear sky solar radiation) to account for varying errors under clear-sky vs. cloudy-sky conditions (Margulis, Liu, et al., 2019).

The moments of the precipitation parameter b distribution are estimated based on the same methodology described in Liu & Margulis (2019) from a sub-sample of 10 tiles across the WUS spanning a range of physiography and climatology (Fig. 2.1 in bold boxes). The precipitation uncertainty is quantified by running the snow reanalysis framework using a uniform (i.e., "uninformative") distribution for the parameter $b \sim U(0.1, 5)$ at the 10 tiles. After assimilating fSCA measurements using the PBS approach, a log-normal distribution is fitted to the posterior b values from all pixels and replicates in those 10 tiles (Table 2.3). The fitted distribution is then treated as the prior distribution for the full WUS–SR domain.

The derivation of uncertainty models for air temperature, dew point temperature and shortwave uncertainty analysis followed Girotto, Margulis, et al. (2014) by comparing downscaled MERRA2 forcings to in situ measurements across the WUS. The uncertainties of MERRA2 forcings are quantified based on in situ Snow Telemetry network (SNOTEL) and Soil Climate Analysis Network (SCAN) air temperature, shortwave, and dew point temperature

measurements. For air temperature and dew point temperature, the differences between downscaled MERRA2 and in situ data (i.e., distribution of temperature errors ε_{Ta} and ε_{Td}) are fitted with normal distributions separately. The in situ solar radiation measurements and downscaled MERRA2 data are used to fit normal distributions (Table 2.3) to the multiplicative parameter γ whose mean and standard deviation are polynomial functions of the *SI*.

Table 2.3 summarizes the fitted parameters of the uncertainty models. The multiplicative precipitation factor b follows a lognormal distribution with mean of 1.80 and coefficient of variation (CV) of 0.69, which corrects the underestimation in raw MERRA2 precipitation used as input to the LSM. The normally distributed air temperature error ε_{Ta}, has a positive mean of 0.85 K, while the dew point temperature error ε_{Td} has mean of -1.37 K. The quantified mean parameters identify (and correct) a cold and dry bias in the MERRA2 data before running the LSM-SDC to generate prior snow estimates.

2.2.4.2 Perturbed Model Parameters

The snow reanalysis framework additionally acknowledges sub-grid snow heterogeneity (resulting in fractional snow-covered area) and the uncertainties in snow albedo that result from different dust conditions.

The sub-grid distribution of snow cover and SWE is captured by the Liston (2004) SDC model with the free parameter representing the coefficient of variation (β) of the lognormal distribution. The free parameter β itself is treated as a uniformly distributed ($\sim U(0.05, 0.8)$, Margulis, Liu, et al., 2019) uncertainty parameter.

The uncertainties in snow albedo in the visible band are accounted for in the BATS snow albedo (α_{vis}) model:

$$\alpha_{vis,j} = (1 - C_{vis,j} f_{age}) \alpha_{VO} \quad (5)$$

where C_{vis} is a uniformly distributed (~U(0.2, 0.45), Margulis, Liu, et al., 2019) uncertainty parameter chosen to span clean to dusty snow conditions (Table 2.3). The variable f_{age} represents the fraction of snow albedo reduction due to snow aging. The fresh snow albedo α_{VO} is set to 0.95. Such an approach does not include any explicit information on dust, but instead tries to realistically span the uncertainty when dust may be present.

Table 2.3 Distributions of meteorological forcings and model parameter perturbations with details described in the Uncertainty Parameters and Measurement Error section. Std. Dev. represents standard deviation and CV represents the coefficient of variation.

Parameters	**Distribution**	**Uncertainty Parameter Distributions Statistics**		
Meteorological Forcings				
b (PPT)	Log normal	**Mean** 1.80	**CV** 0.69	
ε_{Ta} (T_a)	Normal	**Mean** 0.85 K	**Std. Dev.** 1.39 K	
ε_{Td} (T_d)	Normal	**Mean** -1.37 K	**Std. Dev.** 1.20 K	
γ (SW)	Normal	**Mean** 0.2548 $3.66 \cdot SI^3 - 1.88 \cdot SI^3 + 1.39 \cdot SI - 0.05$ 0	**Std. Dev.** 0.39 $-0.39 \cdot SI + 0.58$ 0.19	**SI** < 0.5 0.5 to 1 >1
Model Parameters				
C_{vis} (α_{vis})	Uniform	**Minimum** 0.2	**Maximum** 0.45	
β (SDC)	Uniform	**Minimum** 0.05	**Maximum** 0.8	

2.2.4.3 Measurement Error

The data assimilation framework requires specification of fSCA error standard deviation as an input. The measurement error of retrieved Landsat fSCA is specified as 10% at ~500 m, which is consistent with previous work(Liu et al., 2021; Margulis, Liu, et al., 2019). The

measurement errors between different fSCA measurements are assumed to be uncorrelated in space and time.

2.3 Data Records

The raw gridded 16 arcsecond (~ 500 m) daily snow reanalysis dataset over the WUS (WUS–SR) is publicly available at the National Snow and Ice Data Center (https://doi.org/10.5067/PP7T2GBI52I2)(Fang et al., 2022) in netCDF format. It starts from WY 1985 (Oct. 1st, 1984) to WY 2021 (Sept. 30th, 2021) and will be extended for future WYs when available (Table 2.4). The output files store daily maps of posterior SWE, fSCA, and snow depth within a 1° by 1° tile (Fig. 2.1) for a given WY. The results presented in this paper show the ensemble median of SWE (an output that is determined from the discrete PDF of posterior weights). The ensemble mean, standard deviation, and interquartile range of outputs are also provided in the dataset. Ancillary or derived data products (e.g., non-seasonal snow mask) are available upon request.

Table 2.4 Spatial and temporal information of the WUS–SR dataset.

Spatial Information	
Coverage	Northernmost: 49° N; Southernmost: 31° N Easternmost: 102° W; Westernmost: 125° W
Resolution	16 arcseconds (~ 500 m)
Distribution tile dimension	1° by 1°
Geographic coordinate system	WGS 84
Temporal Information	
Coverage	Oct. 1st, 1984 – Sep. 30th, 2021 (i.e., WYs 1985-2021)
Output Resolution	Daily

2.4 Technical Verification

Fig. 2.4 shows a sample of the seasonal cycle and spatial distribution of SWE over HUC2 basins and the entire WUS domain in WY 2019. No SWE or snow depth measurements are assimilated in deriving the WUS–SR dataset. Thus, in situ SWE and snow depth measurements, and ASO SWE and snow depth estimates are used as independent verification datasets. Landsat fSCA measurements are assimilated into the snow reanalysis framework assuming a measurement error (standard deviation) of 10%(Margulis, Liu, et al., 2019). Though Landsat fSCA cannot be used for independent verification, the WUS–SR posterior fSCA estimates, which are fitted to these measurements using a likelihood function, are expected to have comparable bulk error. The snow reanalysis framework has been successfully applied previously to generate datasets over the Sierra Nevada, Andes, and High Mountain Asia (Margulis, Cortés, Girotto, & Durand, 2016; Cortés & Margulis, 2017; Liu et al., 2021).

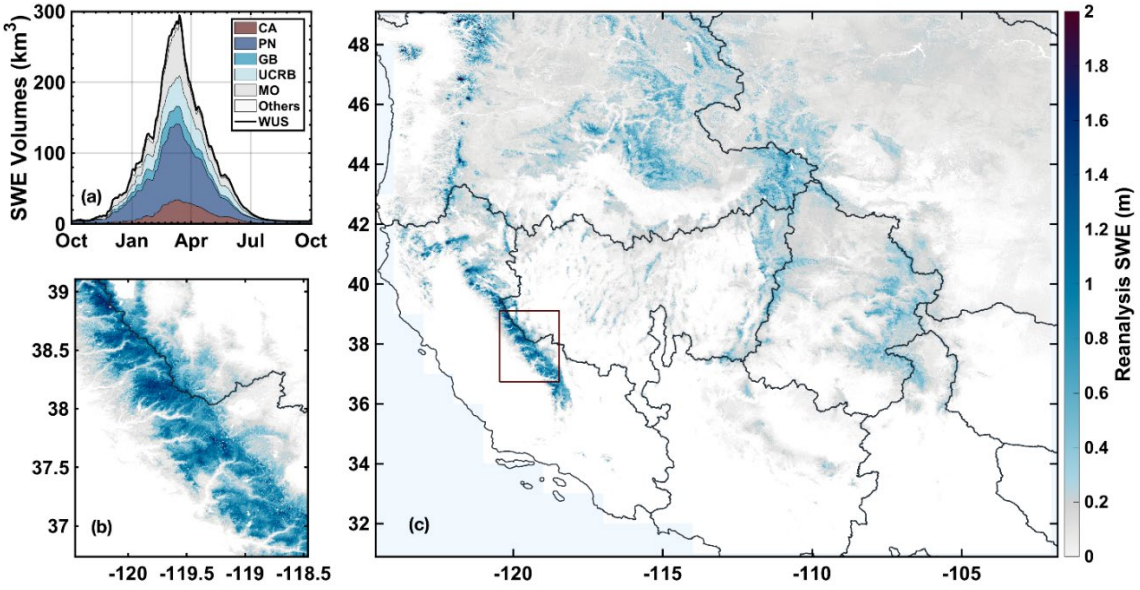

Figure 2.4 Illustrative results from the WUS–SR SWE estimates in WY 2019. (**a**) Seasonal cycle of SWE volume (km^3) integrated over HUC2 basins. (**b**) Spatial distribution of SWE (meters) over part of the Sierra Nevada on March 1st, WY 2019. (**c**) Spatial distribution of WUS SWE (meters) on March 1st, 2019. The boxed area in (c) represents that shown in (**b**).

2.4.1 Verification with in situ Data

In this section, grid-averaged reanalysis SWE and snow depth are compared with point-scale in situ measurements. It should be acknowledged a priori that there are inevitable representativeness issues in the comparison between point-scale in situ data and grid-averaged snow reanalysis data. The WUS–SR estimates are modeled with assumed sub-grid heterogeneity within each ~500 m grid cell (which is modeled via a lognormal distribution) meant to account for the complex sub-grid variations in terrain (elevation, slope, aspect), forest cover, and meteorological forcings. Given that in situ stations are often sited in non-representative regions of a grid cell (i.e., in sheltered flat forest clearings), it is unlikely that the grid-averaged SWE/snow depth (spanning ~ 250,000 m^2) should match the point-scale in situ SWE/snow depth (spanning ~ 10 m^2). Nevertheless, in situ measurements, from the SNOTEL and CA Department of Water Resources (CADWR) networks, represent the best available data that covers much of the WUS and extends back several decades. While not expected to match each other, the verification herein is meant to illustrate consistency between the in situ measurements and WUS–SR estimates.

2.4.1.1 Peak SWE comparison with in situ data

In situ SWE measurements from WY 1985 to 2021 are taken from 1) the SNOTEL network (https://www.wcc.nrcs.usda.gov/snow/) managed by the U.S. Natural Resources Conservation Service (NRCS), and 2) CADWR (https://cdec.water.ca.gov/dynamicapp/staSearch from sensor type: "SNO ADJ (82)"), collections of automated snow pillows in the WUS. For in situ verification, we pair each in situ site with the closest snow reanalysis grid based on the geolocation of these two datasets. The precision of in situ coordinate values varies from 0.000001° (< 1 m) to 0.01° (> 1 km). Considering the potential for geolocation mismatch, the

nine nearest pixels (Girotto, Cortés, et al., 2014; Margulis, Cortés, Girotto, & Durand, 2016; Margulis et al., 2015) are additionally used to compare in situ and WUS–SR peak SWE. In this latter approach, the differences between in situ peak SWE and the neighboring WUS–SR grid cell peak SWE with the smallest difference among the nine nearest snow reanalysis grids are used. To compare the SWE on the same day, peak SWE day determined by in situ SWE is used to extract peak SWE from both datasets throughout the paper.

Figure 2.5 presents the density scatter plots comparing in situ peak SWE values against collocated grid-cell posterior peak SWE values. Peak SWE values less than 1 cm are screened out from the comparison. In total, 928 in situ sites are used in the comparison with the WUS–SR SWE estimates. To understand the performance of the WUS–SR dataset across different regimes in the WUS, verification is conducted for each HUC2 basin. The comparison is quantified using correlation coefficient (*R*), mean difference (*MD*), and root mean square difference (*RMSD*). Table 2.5 summarizes the number of total site-years, and statistics for both prior and posterior reanalysis SWE against in situ SWE within each HUC2 basin and over the WUS.

Compared with the performance of the prior peak SWE estimates (i.e., not constrained by Landsat fSCA), posterior SWE estimates show a better correlation (higher *R*) with less bias and random error (lower *MD* and *RMSD*) than the prior SWE over most of the HUC2 basins. Posterior SWE in CA has the highest correlation against in situ SWE ($R = 0.82$). The correlations with in situ SWE over the entire WUS are improved from 0.74 (prior) to 0.77 (posterior). Posterior peak SWE in UCRB has lower bias and uncertainty compared against in situ data with a relatively small *MD* of 0.06 m in absolute value (reduced by 62% from prior *MD*) and *RMSD* of 0.19 m (reduced by 27%). Over the WUS, in situ peak SWE is (on average) larger than the WUS–SR peak SWE (negative *MD*). Sub-grid topographic variability, snow-forest interactions,

and wind-driven snow redistribution may all cause differences seen between grid-averaged peak SWE and point-scale in situ peak SWE. The statistics for PN indicate comparable correlation of in situ and both prior and posterior snow reanalysis, however the *MD* and *RMSD* do not get improved from posterior to prior. Fewer cloud-free fSCA measurements are available in PN, which limits the improvement of snow reanalysis SWE via data assimilation.

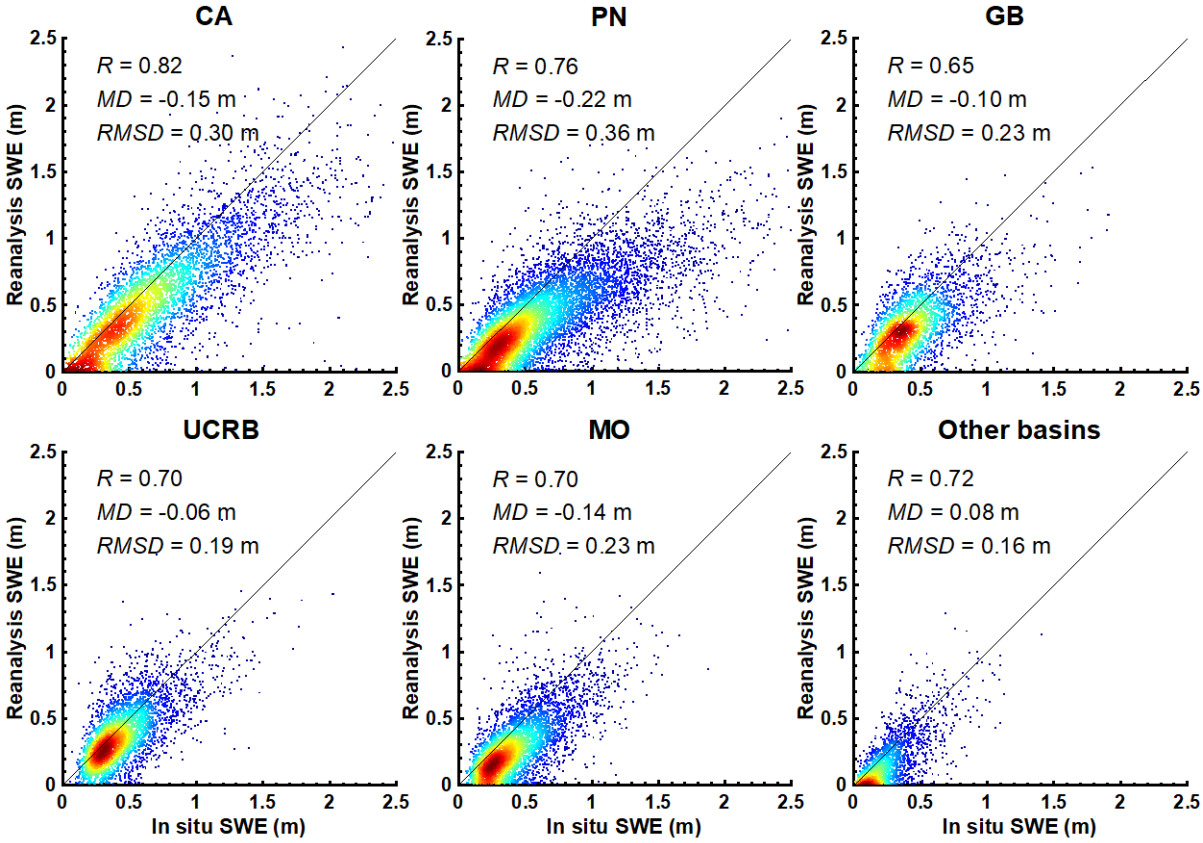

Figure 2.5 Density scatter plot of in situ (snow pillow) peak SWE and collocated posterior (grid-average) peak SWE grouped by HUC2 basins over WYs 1985 to 2021. The solid black line is the 1:1 line. The correlation coefficient (*R*), mean difference (*MD*), and root mean square difference (*RMSD*) are shown for each HUC2 basin. In situ data with peak SWE values greater than 1 cm are included in the comparison.

Table 2.5 Number of in situ sites and comparison metrics between in situ (snow pillow) peak SWE and collocated grid-averaged snow reanalysis prior and posterior (post.) peak SWE grouped by HUC2 basins. Comparison statistics including correlation coefficient (*R*), mean difference (*MD*), and root mean square difference (*RMSD*). *MD* is computed by subtracting snow reanalysis SWE from in situ SWE. A negative *MD* represents that the snow reanalysis peak SWE is less than mean of in situ peak SWE.

HUC2	# Sites	# Site-years	*R*		*MD* (m)		*RMSD* (m)	
			Prior	Post.	Prior	Post.	Prior	Post.
CA	183	4911	0.75	0.82	-0.19	-0.15	0.36	0.30
PN	280	8566	0.76	0.76	-0.11	-0.22	0.31	0.36
GB	114	2776	0.49	0.65	-0.25	-0.10	0.34	0.23
UCRB	134	3823	0.51	0.70	-0.16	-0.06	0.26	0.19
MO	139	4114	0.47	0.70	-0.15	-0.14	0.27	0.23
Others	78	1736	0.59	0.72	0.19	0.08	0.25	0.16
WUS Total	928	25926	0.74	0.77	-0.16	-0.15	0.31	0.28

To acknowledge the potential geolocation mismatch, Fig. 2.6 provides verification of in situ peak SWE and posterior reanalysis peak SWE using an approach comparing to the best match among the nine nearest pixels. The WUS-wide correlation coefficient (*R*), *MD* and *RMSD* of posterior peak SWE and in situ peak SWE is 0.91, -0.08 m, 0.18 m, respectively. Compared to the approach used in Fig. 2.5, the posterior reanalysis peak SWE in Fig. 2.6 (as expected) is more correlated with in situ peak SWE (*R* values above 0.9), and has lower *MD* (< 0.13 m) and *RMSD* (< 0.24 m) over the WUS and at all HUC2 basins. Posterior reanalysis peak SWE is still lower than the in situ peak SWE at most of the sites, with the largest *MD* found in the PN. The PN has fewer cloud-free fSCA measurements, which may lead to larger errors than in regions with fewer cloud-contaminated images. The *MD* in CA is -0.07 m, which is within the range of -0.12 to 0.01 m as reported in Margulis *et al.*(Margulis, Cortés, Girotto, & Durand, 2016), where the original 90-m Sierra Nevada SWE reanalysis was compared against in situ peak SWE using the same approach.

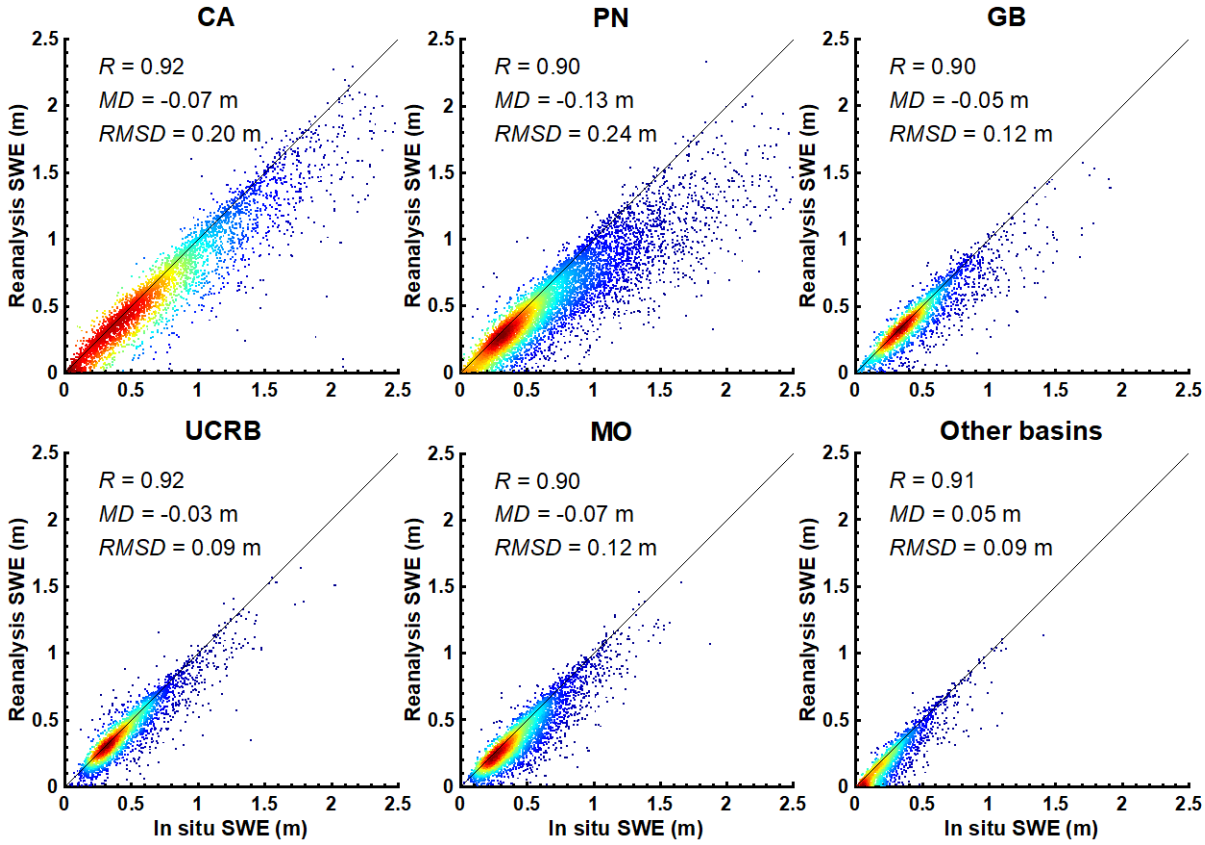

Figure 2.6 Same as the density scatter plot in Fig. 2.5 but using posterior (grid-average) peak SWE from the best match among nine closest neighbor pixels.

Figure 2.7a shows that the differences between posterior peak SWE and in situ peak SWE are sensitive to forest fraction exceeding 40%. The median *RMSD* remains stable at ~ 0.18 m for forest fractions below 40%, and gradually increases to ~ 0.38 m when forest fraction increases to over 60%. The larger *RMSD* at higher forest fraction pixels might be caused by 1) larger disparities between in situ sites (that tend to be in forest clearings) and collocated pixels with large averaged forest coverage fraction and/or 2) larger estimation errors in WUS–SR peak SWE in areas with large forest coverage. Aside from forest coverage effects, the difference between in situ and posterior peak SWE is impacted by the number of fSCA measurements as illustrated in Fig. 2.7b. When over 40 fSCA measurements (after cloud screening) are available,

the median of absolute difference is as low as ~ 0.11 m. As the number of annual fSCA measurements is reduced, the median and spread of the absolute difference of peak SWE for each year increased. Figure 2.7c show that the peak SWE days determined by in situ data is highly correlated to peak SWE days determined by posterior WUS–SR SWE (R = 0.73). Overall, in situ SWE peaks later than the WUS–SR SWE with a *MD* value of -10 days.

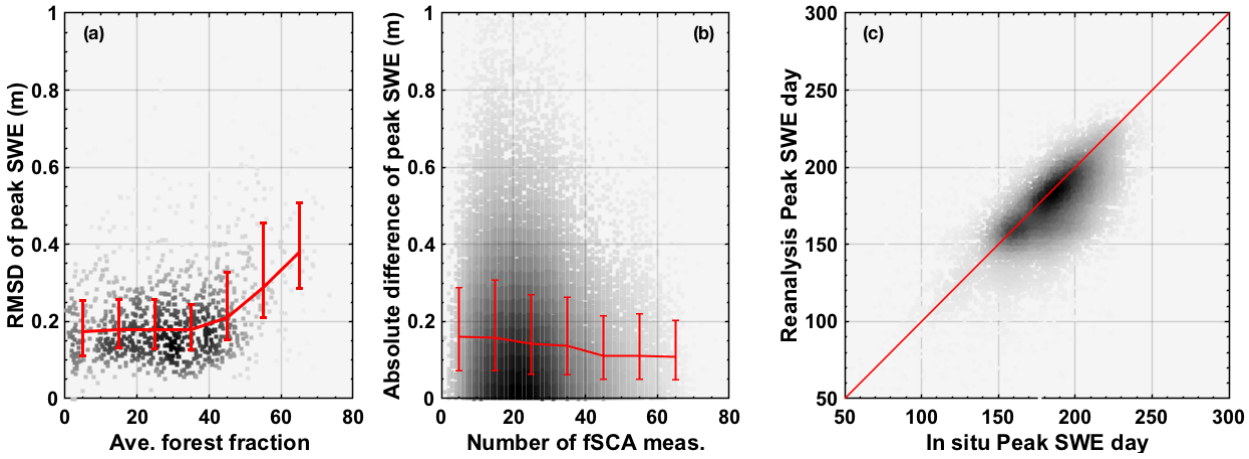

Figure 2.7 (**a**) *RMSD* of peak SWE as a function of averaged forest fraction for each site. *RMSD* is determined at each site from the 37-year peak SWE from in situ and posterior WUS–SR. (**b**) Absolute difference of peak SWE over the number of fSCA measurements (after cloud screening) for each year and site. The absolute difference of peak SWE is computed using in situ and posterior peak SWE. (**c**) Density scatterplot of peak SWE day from in situ and posterior WUS–SR for each year and site.

2.4.1.2 Temporal (daily) SWE comparison with in situ data

Figure 2.8 shows the spatial distribution of verification statistics at in situ sites by comparing posterior daily SWE against in situ daily SWE greater than 2.54 mm.

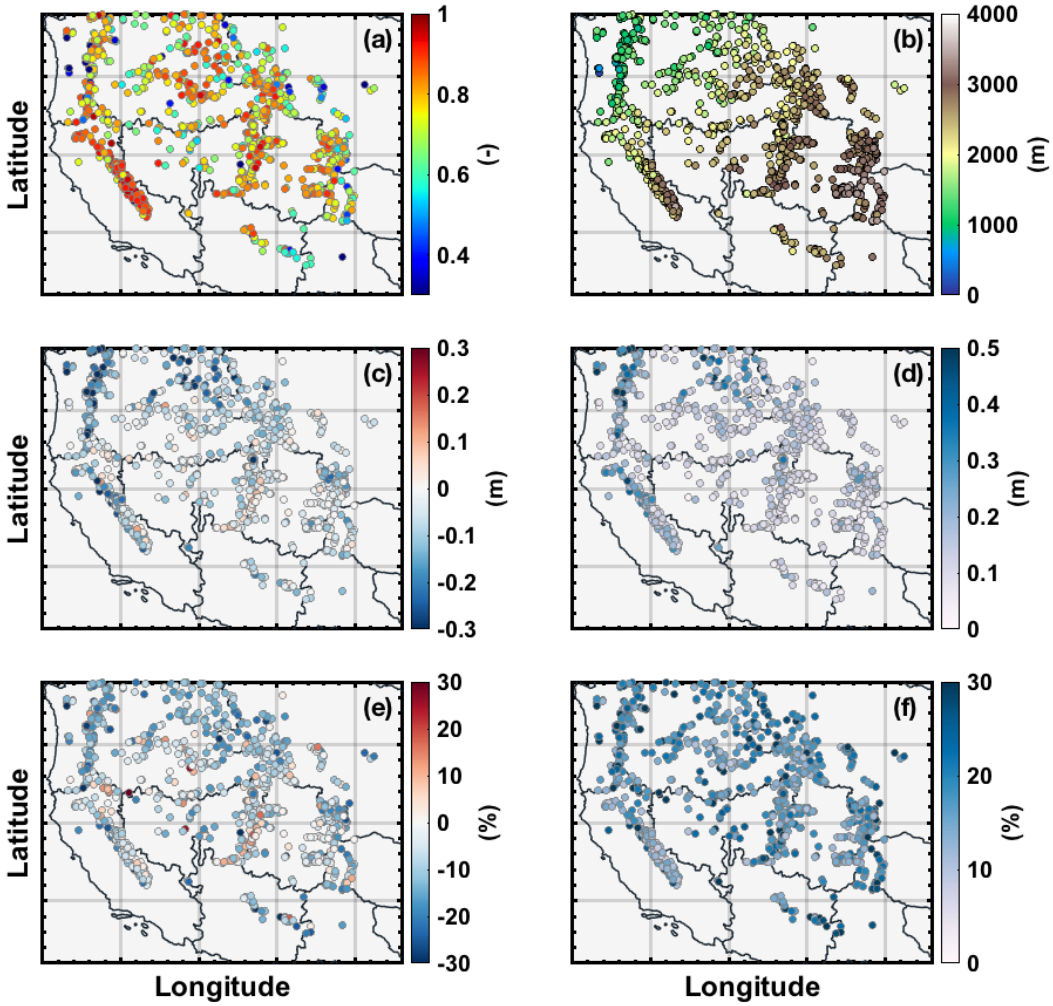

Figure 2.8 Spatial distribution of evaluation statistics determined via comparison of in situ daily SWE and collocated posterior SWE over WYs 1985 to 2021. Statistics include (**a**) *R*, (**c**) *MD* in meters, (**d**) *RMSD* in meters, (**e**) *MD* as percentage of peak SWE, and (**f**) *RMSD* as percentage of peak SWE. For reference, the in situ site elevations in meters are shown in (**b**). Daily SWE values less than 2.54 mm are excluded.

Over the entire WUS, posterior daily SWE at in situ sites have high correlations (median of 0.79), small *MD* (median of -0.08 m) and *RMSD* (median of 0.17 m) against in situ SWE. The comparison suggests that posterior daily SWE agrees reasonably well with daily in situ SWE, especially in CA and UCRB with higher correlations and relatively lower *MD* and *RMSD*. Daily posterior SWE is slightly lower than point-scale in situ SWE (Fig. 2.6b. negative *MD* in blue) at

most of the sites. At some in situ sites in the western PN, posterior SWE shows higher differences. Figure 8 (e) and (f) show that low *MD* and *RMSD* expressed as percent of peak SWE are observed at some sites with high *MD* and *RMSD* due to deep snow. For sites with both large absolute and percent of differences, some of these differences may represent larger errors caused by fewer available fSCA measurements after clouds screening. Finer resolutions may be needed to capture large sub-grid SWE values.

2.4.1.3 Peak snow depth comparison with in situ data

In situ snow depth measurements are taken from the same sources as SWE (i.e., NRCS and CADWR from sensor type: "SNOW DP (18)"). Similar verification steps as with peak SWE (Fig. 2.5) are conducted for snow depth as shown in Fig. 2.9. Compared to the SWE measurements, however, in situ snow depth measurements appear to be of lower quality with some station-years showing snow depth with persistently high values throughout the year, non-physical oscillations in the measurements, and other erroneous behavior that are clearly inconsistent with the corresponding SWE measurements. Hence, extra screening is applied to the data before being used for verification. In situ snow depth measurements that changed by more than 1 m in a single day were assumed erroneous and excluded from the analysis. Further, assuming snow density is within the range of 200 to 500 kg/m^3 at the peak day, snow depth measurements outside 2-5 times the corresponding SWE measurements were removed. To avoid incorrectly diagnosing peak snow depth day from snow depth measurements with missing data after screening, the in situ peak SWE day was used to determine the in situ snow depth used for comparison with posterior reanalysis estimates. Overall, posterior peak snow depth is correlated with in situ peak snow depth (R = 0.72) and has an *MD* of -0.36 m and *RMSD* of 0.66 m over the WUS. Compared to the results from peak SWE verification, the correlation coefficient between

in situ and posterior peak snow depth is about the same at all HUC2 basins, with the highest value (R = 0.81) in CA. The *MD* and *RMSD* values for peak snow depth are around 2 to 3 times larger than those in peak SWE, partially caused by larger snow depth values than SWE and perhaps the poorer quality of in situ snow depth measurements.

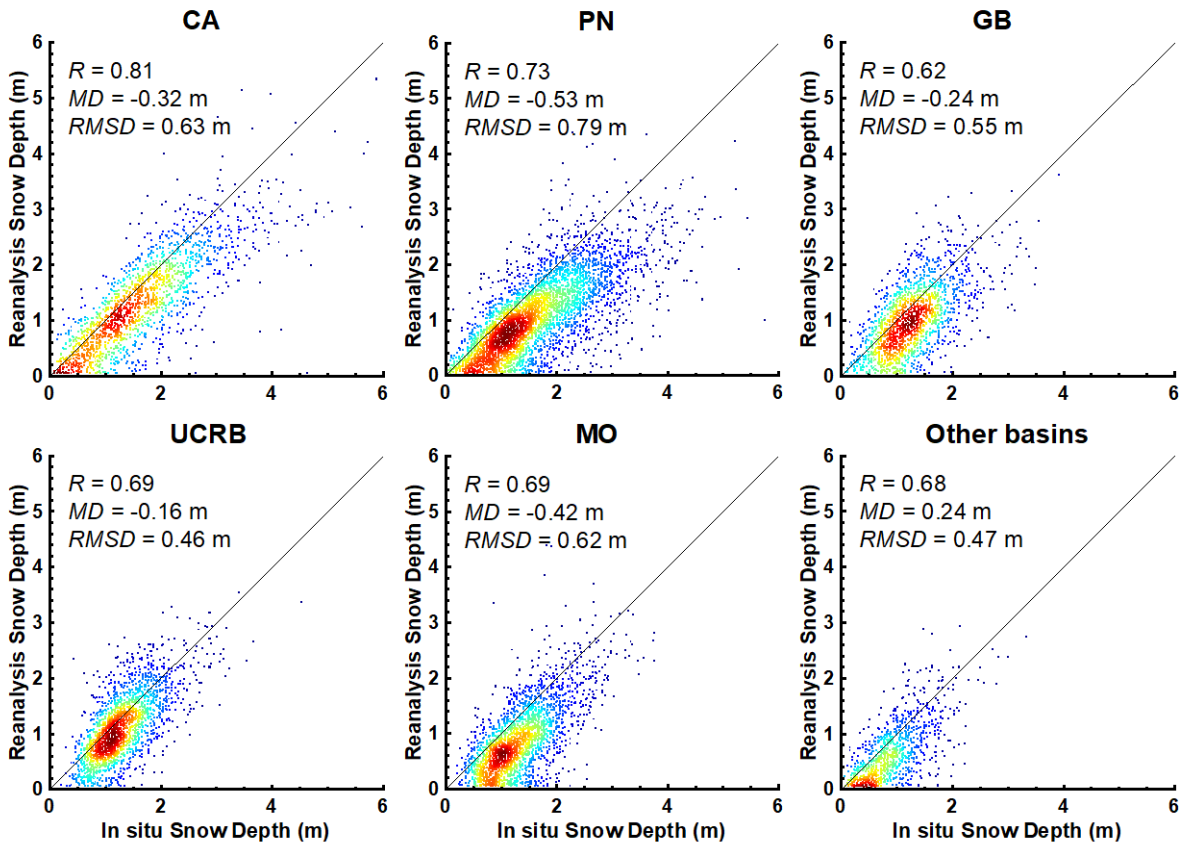

Figure 2.9 Same as Fig. 2.5 but for peak snow depth. Peak day is determined by in situ peak SWE. In situ data with peak snow depth values greater than 5 cm are included in the comparison.

2.4.2 Verification with Airborne Snow Observatory (ASO) Data

The WUS–SR estimates are further verified against gridded SWE and snow depth estimates from ASO (Painter et al., 2016). The lidar-based ASO measures snow depth via an airborne laser scanner (ALS) based on the differences in elevations between a snow-off day and snow-on days. ASO SWE is estimated from the high-resolution snow depth measurements and

modeled snow density (Painter et al., 2016). For comparison, the 50-m ASO SWE and snow depth snapshots are aggregated to the WUS–SR SWE model resolution. ASO data is available over select sites in California, Colorado, and Washington starting from 2013. While abundant snapshots are available in the Tuolumne River Basin in California, limited snapshots (commonly once per year) were taken at most of the ASO sites. ASO snow depth is a relatively accurate measurement with measurement error less than 0.02 m at a 50 m × 50 m grid. Model error (5% - 8% (Painter et al., 2016) could exist in modeled snow density, which is expected to propagate to ASO SWE estimates.

ASO SWE and snow depth estimates are compared with prior and posterior ensemble median SWE and snow depth maps on coincident days (Fig. 2.10 and 2.11). Table 2.6 and 2.7 reports the statistical metrics for comparisons closest to April 1st at sampled ASO basins: USCATB (Tuolumne River Basin, California), USWAOL (Olympic Mountains, Washington), and USCOCM (Aspen/Castle-Maroon, Colorado).

2.4.2.1 SWE map comparison

For the California domain (USCATB), posterior SWE is highly correlated with ASO SWE (ranging from 0.81 to 0.91) compared against prior SWE (ranging from 0.50 to 0.71). A negative *MD* indicates that the WUS–SR SWE is less than ASO SWE (on average) in Tuolumne. The difference significantly decreases from prior to posterior estimates in most years, along with decreased *RMSD*. WY 2015 was a historically dry year, in which posterior SWE shows no bias compared with ASO SWE, with a small *RMSD* of 0.07 m. Posterior SWE in WY 2017 has the highest correlation (0.91) with ASO SWE compared with a lower correlation (0.56) in prior SWE. *MD* drops from -0.13 m to -0.04 m, and *RMSD* decreases by half from prior to posterior in WY 2017. Fig. 2.10 (top row) illustrates that Tuolumne-averaged posterior SWE (1.23 m) is

comparable with ASO SWE (1.27 m), suggesting that the posterior WUS–SR SWE and ASO are in good agreement with respect to the basin-wide mean SWE. The prior underestimates SWE at high elevations in the northern parts and southern edges of Tuolumne basins whereas it overestimates shallow SWE near the basin outlet. The performance of the spatially distributed posterior SWE is considerably improved over the prior compared with ASO SWE. Though *MD* in WY 2019 increases from -0.06 m to -0.14 m (from prior to posterior), *RMSD* in that year decreases from 0.34 m to 0.27 m. The differences between prior SWE and ASO SWE are large in absolute values, while large positive differences are offset by negative differences causing a low *MD* for prior SWE in WY 2019.

Non-seasonal SWE in portions of the PN (USWAOL) site is a potential error source in both ASO SWE and WUS–SR SWE. Snow depth retrieved from ASO may be erroneous at glacier pixels due to the lack of snow-off flights. The snow reanalysis framework does not include explicit modeling of glaciers. Therefore, non-seasonal snow pixels are removed when comparing the ASO SWE with WUS–SR SWE. This paper generates the WUS–SR non-seasonal snow mask following the method described in Liu *et al.*(Liu et al., 2021). To summarize the method herein, a pixel is considered as a non-seasonal snow pixel if the annual minimum SWE exceeds 10% of the annual maximum SWE at least once over the dataset period. After applying the non-seasonal snow mask, the mean posterior SWE is 0.51 m which is slightly lower than 0.55 m in ASO SWE. Though the correlation coefficient is high (over 0.8) between prior snow reanalysis SWE and ASO SWE, the *MD* and *RMSD* in absolute value is over 0.50 m and 0.60 m respectively, which are both reduced significantly (by 94% and 44% respectively) in the posterior.

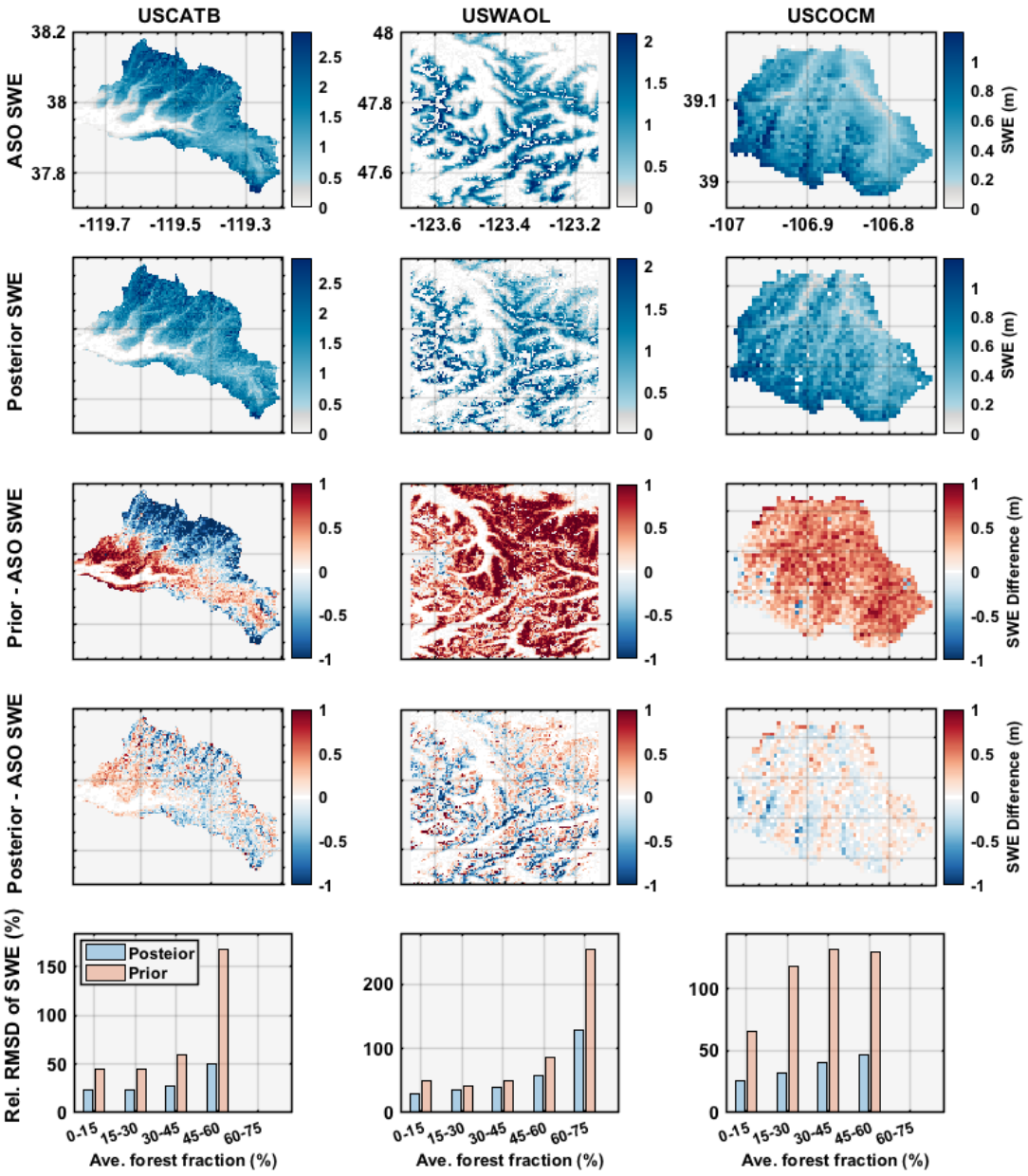

Figure 2.10 Comparison of ASO SWE with prior and posterior SWE at three ASO sites (top four rows): Tuolumne River Basin, California, (USCATB) in WY 2017 (left column); Olympic Mountains, Washington, (USWAOL) in WY 2016 (middle column); Aspen/Castle-Maroon, Colorado (USCOCM) in WY 2019 (bottom column). The prior maps are not shown, but instead included implicitly via the difference maps. The bottom row shows the relative *RMSD* between ASO and WUS–SR SWE as a function of forest fraction. *RMSD* (computed from pixels with both ASO and WUS–SR SWE greater than 1 cm) is computed for each forest fraction bin and then normalized by bin-averaged ASO SWE to get relative *RMSD*.

Table 2.6 SWE comparison statistics between ASO SWE estimates and prior and posterior (post.) snow reanalysis SWE on ASO measurement days (Day of Water Year; DOWY) closest to April 1st. USCATB represents the Tuolumne River Basin (California); USWAOL represents the Olympic Mountains (Washington); USCOCM represents Aspen/Castle-Maroon (Colorado).

ASO basins	Year	DOWY	*R*		*MD* (m)		*RMSD* (m)	
			Prior	Post.	Prior	Post.	Prior	Post.
USCATB	2015	185	0.54	0.81	-0.05	0.00	0.09	0.07
	2016	184	0.59	0.83	-0.24	-0.15	0.37	0.25
	2017	183	0.56	0.91	-0.13	-0.04	0.63	0.32
	2018	205	0.63	0.82	-0.18	-0.11	0.30	0.22
	2019	175	0.62	0.84	-0.06	-0.14	0.34	0.27
	2020	196	0.71	0.88	0.03	0.05	0.14	0.13
	2021	211	0.50	0.82	-0.12	0.03	0.18	0.13
USWAOL	2016	181	0.81	0.81	0.53	-0.03	0.68	0.38
USCOCM	2019	189	0.45	0.75	0.41	0.01	0.47	0.17

In Colorado (USCOCM), the mean of posterior SWE (0.55 m) is comparable with ASO SWE (0.54 m). The *MD* is reduced by 98% (to 0.01 m) and *RMSD* is reduced by 64% (to 0.17 m) from prior to posterior estimates. Although the posterior correlation coefficient is significantly improved over the prior, it is lower than the values seen at the USCATB and USWAOL sites. In Colorado, snow albedo has been shown to be affected by dust, black carbon, and other light-absorbing particles in recent decades(Deems et al., 2013). In the current snow reanalysis framework, the impact of dust on snow albedo is modeled through an unconstrained uncertainty parameter. Future work could be done to apply a more explicit treatment of dust impacts on snow albedo to yield potentially improved results.

The effect of forest fraction on the performance of reanalysis SWE estimates is further illustrated using ASO SWE in Figure 10. The Olympics basin has denser forest fraction with a mean of 58%, while the Tuolumne and Aspen/Castle-Maroon basins have mean forest fractions of 17% and 20%, respectively. At all three ASO basins, the relative RMSD of posterior SWE

increases with the forest fraction. This is expected since Landsat-derived fSCA is only available over bare areas and/or forest gaps within a pixel. As forest cover increases, less useful information is available, while information is maximized at 0% of forest cover. However, the improvement in prior to posterior SWE estimates increases with forest coverage. This is likely related to the increased complexity of modeling SWE in dense forest areas where the larger uncertainty in forest areas is still reduced with the assimilation of fSCA.

2.4.2.2 Snow depth map comparison

Similar to the SWE comparison, posterior snow depth is verified against the ASO snow depth measurements (Fig. 2.11, Table 2.7). The spatial distribution of snow depth differences is comparable to the SWE differences with a correlation coefficient (R) of 0.85 and 0.76 in Washington and Colorado, respectively, and a value above 0.82 in California. In California, the *MD* of posterior snow depth is reduced by over 30% and *RMSD* is reduced by over 20% compared to the statistics of prior snow depth over WY 2015 to 2018, and WY 2021. In WY 2019 and 2020, while the posterior *MD* values are larger than the prior *MD* (positive and negative differences cancel each other out), the *R* values are as high as 0.9, and the *RMSD* values are reduced by 28% and 30%, respectively. In Washington, the posterior *MD* is close to 0 with *RMSD* significantly reduced by over 50% from the prior to the posterior estimates. In Colorado, despite the absolute values of *MD* and *RMSD* for posterior snow depth being more than twice the values of posterior SWE statistics (due to the larger dynamic range), the estimation of posterior snow depth is significantly improved from the prior snow depth with *MD* and *RMSD* reduced by 60% and 40%, respectively.

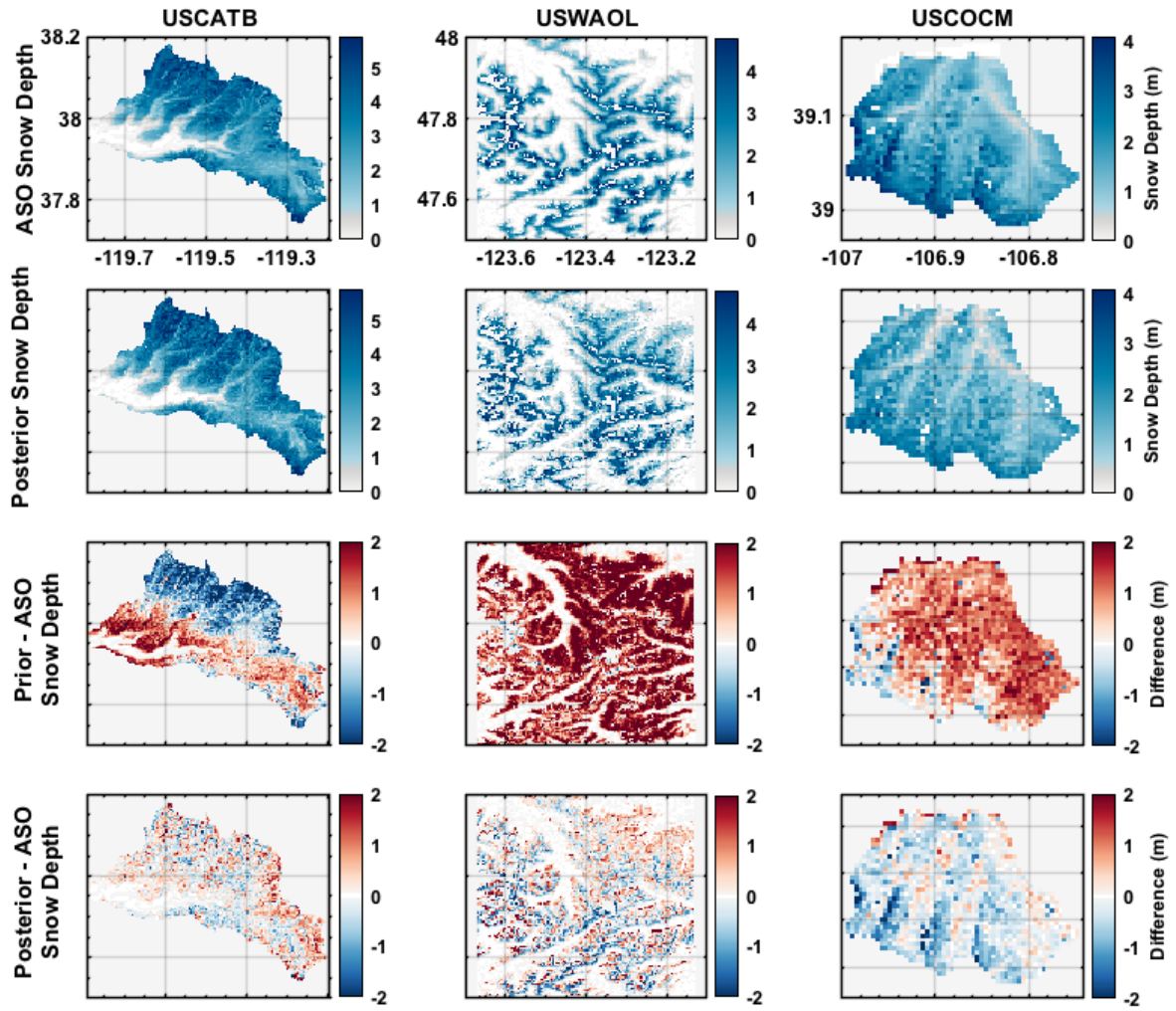

Figure 2.11 same as Fig. 2.10 (top four rows) but for snow depth.

Table 2.7 same as Table 2.6 but for snow depth.

ASO basins	Year	DOWY	*R*		*MD* (m)		*RMSD* (m)	
			Prior	Post.	Prior	Post.	Prior	Post.
USCATB	2015	185	0.54	0.82	-0.10	-0.01	0.21	0.14
	2016	184	0.73	0.90	-0.38	-0.18	0.69	0.41
	2017	183	0.61	0.92	-0.13	0.09	1.16	0.62
	2018	205	0.71	0.83	-0.32	-0.18	0.60	0.46
	2019	175	0.72	0.90	-0.01	-0.20	0.78	0.56
	2020	196	0.75	0.90	0.02	0.05	0.43	0.30
	2021	211	0.50	0.82	-0.33	0.04	0.47	0.29
USWAOL	2016	181	0.81	0.85	1.34	0.02	1.64	0.76
USCOCM	2019	189	0.54	0.76	0.75	-0.30	1.03	0.62

2.5 Usage Notes

The snow reanalysis framework described herein is designed to capture seasonal snow in mountainous areas and does not model glacier processes. However, some non-seasonal snow and glaciers may exist in some regions of the WUS (e.g., the Olympics). Such grid cells can be diagnosed and excluded as described above using the non-seasonal snow mask (as diagnosed via the snow reanalysis framework). It is recommended to mask out these pixels before comparing with other datasets for seasonal snow.

The WUS–SR dataset is developed from a LSM-SDC model integrated with fSCA data assimilation. The strength of the product is in its space-time continuity where highly uncertain model-based prior estimates are constrained by snow measurements. While uncertainty and bias correction are embedded in the framework, errors and uncertainty in MERRA2 forcings, model parameters, and Landsat fSCA retrievals undoubtedly affect the accuracy of SWE estimates. Developing the uncertainty models using sparse in situ data and application of uncertainty model parameters uniformly over space, likely both oversimplify the true uncertainty and how it varies across different physiographic and climatological gradients.

Compared with the previous framework and inputs used in the published 90-m reanalysis dataset over the Sierra Nevada (Margulis, Cortés, Girotto, & Durand, 2016), some key updates/changes in the current snow reanalysis framework include: 1) use of MERRA2 forcings instead of NLDAS2 forcings, which are globally available and were found to yield marginally better SWE estimates relative to ASO estimates in Tuolumne (Margulis, Liu, et al., 2019); 2) use of the SRTM DEM (with the ASTER DEM used for void filling) and 3) use of the globally available AVHRR landcover map instead of the National Land Cover Database limited in the

U.S. These changes are primarily made to use globally available data for extension and application to broad spatial domains.

Future versions of this dataset could include: 1) use of multi-source fSCA measurements from Landsat, MODIS, Sentinel, and/or other sources (e.g., VIIRS) to increase the number of cloud-free fSCA images (especially in the Pacific Northwest); 2) examination of the impact of different forcings (e.g., NLDAS2, MERRA2, ERA5) and their uncertainties; 3) use of time-varying forest cover to better reflect transient changes; 4) use of dust-on-snow measurements (Skiles et al., 2015) to better constrain albedo; and 5) use of multi-resolution approaches (Baldo & Margulis, 2018, 2017) to better capture snow estimates in complex terrain with higher resolution where necessary; 6) use of fSCA from Landsat 9 in the future versions.

2.6 Bibliography

Andreadis, K. M., & Lettenmaier, D. P. (2006). Assimilating remotely sensed snow observations into a macroscale hydrology model. *Advances in Water Resources*, *29*(6), 872–886. https://doi.org/10.1016/j.advwatres.2005.08.004

Baldo, E., & Margulis, S. A. (2017). Implementation of a physiographic complexity-based multiresolution snow modeling scheme: MULTIRESOLUTION SNOW MODELING. *Water Resources Research*, *53*(5), 3680–3694. https://doi.org/10.1002/2016WR020021

Baldo, E., & Margulis, S. A. (2018). Assessment of a multiresolution snow reanalysis framework: A multidecadal reanalysis case over the upper Yampa River basin, Colorado. *Hydrology and Earth System Sciences*, *22*(7), 3575–3587. https://doi.org/10.5194/hess-22-3575-2018

Cortés, G., Girotto, M., & Margulis, S. A. (2014). Analysis of sub-pixel snow and ice extent over the extratropical Andes using spectral unmixing of historical Landsat imagery. *Remote Sensing of Environment*, *141*, 64–78. https://doi.org/10.1016/j.rse.2013.10.023

Cortés, G., & Margulis, S. (2017). Impacts of El Niño and La Niña on interannual snow accumulation in the Andes: Results from a high-resolution 31 year reanalysis. *Geophysical Research Letters*, *44*(13), 6859–6867. https://doi.org/10.1002/2017GL073826

Deems, J. S., Painter, T. H., Barsugli, J. J., Belnap, J., & Udall, B. (2013). Combined impacts of current and future dust deposition and regional warming on Colorado River Basin snow dynamics and hydrology. *Hydrology and Earth System Sciences*, *17*(11), 4401–4413. https://doi.org/10.5194/hess-17-4401-2013

Dickinson, R. E., Henderson-Sellers, A., & Kennedy, P. J. (1993). *Biosphere-Atmosphere Transfer Scheme (BATS) version 1e as coupled to the NCAR community climate model. Technical note. [NCAR (National Center for Atmospheric Research)]* (PB-94-106150/XAB; NCAR/TN-387+STR). UCAR/NCAR. http://dx.doi.org/10.5065/D67W6959

Fang, Y., Liu, Y., & Margulis, S. (2022). *Western United States UCLA Daily Snow Reanalysis*. National Snow and Ice Data Center Distributed Active Archive Center (NSIDC DAAC). https://doi.org/10.5067/PP7T2GBI52I2

Fang, Y., Liu, Y., & Margulis, S. A. (2022). *Western United States UCLA Daily Snow Reanalysis, Version 1*. Boulder, Colorado USA. NASA National Snow and Ice Data Center Distributed Active Archive Center. https://doi.org/10.5067/PP7T2GBI52I2

Farr, T. G., Rosen, P. A., Caro, E., Crippen, R., Duren, R., Hensley, S., Kobrick, M., Paller, M., Rodriguez, E., Roth, L., Seal, D., Shaffer, S., Shimada, J., Umland, J., Werner, M., Oskin,

M., Burbank, D., & Alsdorf, D. (2007). The Shuttle Radar Topography Mission. *Reviews of Geophysics*, *45*(2). https://doi.org/10.1029/2005RG000183

Gelaro, R., McCarty, W., Suárez, M. J., Todling, R., Molod, A., Takacs, L., Randles, C. A., Darmenov, A., Bosilovich, M. G., Reichle, R., Wargan, K., Coy, L., Cullather, R., Draper, C., Akella, S., Buchard, V., Conaty, A., Silva, A. M. da, Gu, W., … Zhao, B. (2017). The Modern-Era Retrospective Analysis for Research and Applications, Version 2 (MERRA-2). *Journal of Climate*, *30*(14), 5419–5454. https://doi.org/10.1175/JCLI-D-16-0758.1

Girotto, M., Cortés, G., Margulis, S. A., & Durand, M. (2014). Examining spatial and temporal variability in snow water equivalent using a 27 year reanalysis: Kern River watershed, Sierra Nevada. *Water Resources Research*, *50*(8), 6713–6734. https://doi.org/10.1002/2014WR015346

Girotto, M., Margulis, S. A., & Durand, M. (2014). Probabilistic SWE reanalysis as a generalization of deterministic SWE reconstruction techniques: PROBABILISTIC SWE REANALYSIS. *Hydrological Processes*, *28*(12), 3875–3895. https://doi.org/10.1002/hyp.9887

Hamilton, A. L., Characklis, G. W., & Reed, P. M. (2020). Managing Financial Risk Trade-Offs for Hydropower Generation Using Snowpack-Based Index Contracts. *Water Resources Research*, *56*(10), e2020WR027212. https://doi.org/10.1029/2020WR027212

Hansen, M. C., Defries, R. S., Townshend, J. R. G., & Sohlberg, R. (2000). Global land cover classification at 1 km spatial resolution using a classification tree approach. *International Journal of Remote Sensing*, *21*(6–7), 1331–1364. https://doi.org/10.1080/014311600210209

Hersbach, H., Bell, B., Berrisford, P., Hirahara, S., Horányi, A., Muñoz-Sabater, J., Nicolas, J., Peubey, C., Radu, R., Schepers, D., Simmons, A., Soci, C., Abdalla, S., Abellan, X., Balsamo, G., Bechtold, P., Biavati, G., Bidlot, J., Bonavita, M., … Thépaut, J.-N. (2020). The ERA5 global reanalysis. *Quarterly Journal of the Royal Meteorological Society*, *146*(730), 1999–2049. https://doi.org/10.1002/qj.3803

Huning, L. S., & AghaKouchak, A. (2020a). Global snow drought hot spots and characteristics. *Proceedings of the National Academy of Sciences*, *117*(33), 19753–19759. https://doi.org/10.1073/pnas.1915921117

Huning, L. S., & AghaKouchak, A. (2020b). Approaching 80 years of snow water equivalent information by merging different data streams. *Scientific Data*, *7*(1), 333. https://doi.org/10.1038/s41597-020-00649-1

Kim, R. S., Kumar, S., Vuyovich, C., Houser, P., Lundquist, J., Mudryk, L., Durand, M., Barros, A., Kim, E. J., Forman, B. A., Gutmann, E. D., Wrzesien, M. L., Garnaud, C., Sandells, M., Marshall, H.-P., Cristea, N., Pflug, J. M., Johnston, J., Cao, Y., … Wang, S. (2021). Snow Ensemble Uncertainty Project (SEUP): Quantification of snow water equivalent uncertainty across North America via ensemble land surface modeling. *The Cryosphere*, *15*(2), 771–791. https://doi.org/10.5194/tc-15-771-2021

Kobayashi, S., Ota, Y., Harada, Y., Ebita, A., Moriya, M., Onoda, H., Onogi, K., Kamahori, H., Kobayashi, C., Endo, H., Miyaoka, K., & Takahashi, K. (2015). The JRA-55 Reanalysis: General Specifications and Basic Characteristics. *Journal of the Meteorological Society of Japan. Ser. II*, *93*(1), 5–48. https://doi.org/10.2151/jmsj.2015-001

Larson, K. M., Gutmann, E. D., Zavorotny, V. U., Braun, J. J., Williams, M. W., & Nievinski, F. G. (2009). Can we measure snow depth with GPS receivers? *Geophysical Research Letters*, *36*(17), L17502. https://doi.org/10.1029/2009GL039430

Li, D., Lettenmaier, D. P., Margulis, S. A., & Andreadis, K. (2019). The Value of Accurate High-Resolution and Spatially Continuous Snow Information to Streamflow Forecasts. *Journal of Hydrometeorology*, *20*(4), 731–749. https://doi.org/10.1175/JHM-D-18-0210.1

Li, D., Wrzesien, M. L., Durand, M., Adam, J., & Lettenmaier, D. P. (2017). How much runoff originates as snow in the western United States, and how will that change in the future? *Geophysical Research Letters*, *44*(12), 6163–6172. https://doi.org/10.1002/2017GL073551

Lievens, H., Demuzere, M., Marshall, H.-P., Reichle, R. H., Brucker, L., Brangers, I., de Rosnay, P., Dumont, M., Girotto, M., Immerzeel, W. W., Jonas, T., Kim, E. J., Koch, I., Marty, C., Saloranta, T., Schöber, J., & De Lannoy, G. J. M. (2019). Snow depth variability in the Northern Hemisphere mountains observed from space. *Nature Communications*, *10*(1), 4629. https://doi.org/10.1038/s41467-019-12566-y

Liston, G. E. (2004). Representing Subgrid Snow Cover Heterogeneities in Regional and Global Models. *Journal of Climate*, *17*(6), 1381–1397. https://doi.org/10.1175/1520-0442(2004)017<1381:RSSCHI>2.0.CO;2

Liu, Y., Fang, Y., & Margulis, S. A. (2021). Spatiotemporal distribution of seasonal snow water equivalent in High Mountain Asia from an 18-year Landsat–MODIS era snow reanalysis dataset. *The Cryosphere*, *15*(11), 5261–5280. https://doi.org/10.5194/tc-15-5261-2021

Liu, Y., & Margulis, S. A. (2019). Deriving Bias and Uncertainty in MERRA-2 Snowfall Precipitation Over High Mountain Asia. *Frontiers in Earth Science*, *7*, 280. https://doi.org/10.3389/feart.2019.00280

Luojus, K., Pulliainen, J., Takala, M., Lemmetyinen, J., Mortimer, C., Derksen, C., Mudryk, L., Moisander, M., Hiltunen, M., Smolander, T., Ikonen, J., Cohen, J., Salminen, M., Norberg, J., Veijola, K., & Venäläinen, P. (2021). GlobSnow v3.0 Northern Hemisphere snow water equivalent dataset. *Scientific Data*, *8*(1), 163. https://doi.org/10.1038/s41597-021-00939-2

Margulis, S. A., Cortés, G., Girotto, M., & Durand, M. (2016). A Landsat-Era Sierra Nevada Snow Reanalysis (1985–2015). *Journal of Hydrometeorology*, *17*(4), 1203–1221. https://doi.org/10.1175/JHM-D-15-0177.1

Margulis, S. A., Cortés, G., Girotto, M., Huning, L. S., Li, D., & Durand, M. (2016). Characterizing the extreme 2015 snowpack deficit in the Sierra Nevada (USA) and the implications for drought recovery. *Geophysical Research Letters*, *43*(12), 6341–6349. https://doi.org/10.1002/2016GL068520

Margulis, S. A., Fang, Y., Li, D., Lettenmaier, D. P., & Andreadis, K. (2019). The Utility of Infrequent Snow Depth Images for Deriving Continuous Space-Time Estimates of Seasonal Snow Water Equivalent. *Geophysical Research Letters*, *46*(10), 5331–5340. https://doi.org/10.1029/2019GL082507

Margulis, S. A., Girotto, M., Cortés, G., & Durand, M. (2015). A Particle Batch Smoother Approach to Snow Water Equivalent Estimation. *Journal of Hydrometeorology*, *16*(4), 1752–1772. https://doi.org/10.1175/JHM-D-14-0177.1

Margulis, S. A., Liu, Y., & Baldo, E. (2019). A Joint Landsat- and MODIS-Based Reanalysis Approach for Midlatitude Montane Seasonal Snow Characterization. *Frontiers in Earth Science*, *7*, 272. https://doi.org/10.3389/feart.2019.00272

Markus, T., Neumann, T., Martino, A., Abdalati, W., Brunt, K., Csatho, B., Farrell, S., Fricker, H., Gardner, A., Harding, D., Jasinski, M., Kwok, R., Magruder, L., Lubin, D., Luthcke, S., Morison, J., Nelson, R., Neuenschwander, A., Palm, S., … Zwally, J. (2017). The Ice, Cloud, and land Elevation Satellite-2 (ICESat-2): Science requirements, concept, and implementation. *Remote Sensing of Environment*, *190*, 260–273. https://doi.org/10.1016/j.rse.2016.12.029

Molotch, N. P., & Bales, R. C. (2006). SNOTEL representativeness in the Rio Grande headwaters on the basis of physiographics and remotely sensed snow cover persistence. *Hydrological Processes*, *20*(4), 723–739. https://doi.org/10.1002/hyp.6128

Muñoz-Sabater, J., Dutra, E., Agustí-Panareda, A., Albergel, C., Arduini, G., Balsamo, G., Boussetta, S., Choulga, M., Harrigan, S., Hersbach, H., Martens, B., Miralles, D. G., Piles, M., Rodríguez-Fernández, N. J., Zsoter, E., Buontempo, C., & Thépaut, J.-N. (2021). ERA5-Land: A state-of-the-art global reanalysis dataset for land applications. *Earth System Science Data*, *13*(9), 4349–4383. https://doi.org/10.5194/essd-13-4349-2021

NASA. (2001). *Advanced Spaceborne Thermal Emission and Reflection Radiometer (ASTER)*. http://asterweb.jpl.nasa.gov/

National Operational Hydrologic Remote Sensing Center. (2004). *Snow Data Assimilation System (SNODAS) Data Products at NSIDC, Version 1*.

Nghiem, S. V. & Wu-Yang Tsai. (2001). Global snow cover monitoring with spaceborne K/sub u/-band scatterometer. *IEEE Transactions on Geoscience and Remote Sensing*, *39*(10), 2118–2134. https://doi.org/10.1109/36.957275

Nolin, A. W., Sproles, E. A., Rupp, D. E., Crumley, R. L., Webb, M. J., Palomaki, R. T., & Mar, E. (2021). New snow metrics for a warming world. *Hydrological Processes*, *35*(6). https://doi.org/10.1002/hyp.14262

Painter, T. H., Berisford, D. F., Boardman, J. W., Bormann, K. J., Deems, J. S., Gehrke, F., Hedrick, A., Joyce, M., Laidlaw, R., Marks, D., Mattmann, C., McGurk, B., Ramirez, P., Richardson, M., Skiles, S. M., Seidel, F. C., & Winstral, A. (2016). The Airborne Snow Observatory: Fusion of scanning lidar, imaging spectrometer, and physically-based modeling for mapping snow water equivalent and snow albedo. *Remote Sensing of Environment*, *184*, 139–152. https://doi.org/10.1016/j.rse.2016.06.018

Pflug, J. M., Margulis, S. A., & Lundquist, J. D. (2022). Inferring watershed-scale mean snowfall magnitude and distribution using multidecadal snow reanalysis patterns and snow pillow observations. *Hydrological Processes*, *36*(6), e14581. https://doi.org/10.1002/hyp.14581

Rodell, M., Houser, P. R., Jambor, U., Gottschalck, J., Mitchell, K., Meng, C.-J., Arsenault, K., Cosgrove, B., Radakovich, J., Bosilovich, M., Entin, J. K., Walker, J. P., Lohmann, D., & Toll, D. (2004). The Global Land Data Assimilation System. *Bulletin of the American Meteorological Society*, *85*(3), 381–394. https://doi.org/10.1175/BAMS-85-3-381

Sexton, J. O., Feng, M., Channan, S., Noojipady, P., Song, X.-P., Anand, A., Huang, C., Kim, D.-H., DiMiceli, C., & Townshend, J. R. *Global 30m Landsat Tree Canopy Version 4.* NASA's Land Processes Distributed Active Archive Center (LP DAAC). https://e4ftl01.cr.usgs.gov/MEASURES/GFCC30TC.003/

Sexton, J. O., Song, X.-P., Feng, M., Noojipady, P., Anand, A., Huang, C., Kim, D.-H., Collins, K. M., Channan, S., DiMiceli, C., & Townshend, J. R. (2013). Global, 30-m resolution continuous fields of tree cover: Landsat-based rescaling of MODIS vegetation continuous fields with lidar-based estimates of error. *International Journal of Digital Earth*, *6*(5), 427–448. https://doi.org/10.1080/17538947.2013.786146

Shi, J., & Dozier, J. (2000). Estimation of snow water equivalence using SIR-C/X-SAR. II. Inferring snow depth and particle size. *IEEE Transactions on Geoscience and Remote Sensing*, *38*(6), 2475–2488. https://doi.org/10.1109/36.885196

Skiles, S. M., Painter, T. H., Belnap, J., Holland, L., Reynolds, R. L., Goldstein, H. L., & Lin, J. (2015). Regional variability in dust-on-snow processes and impacts in the Upper Colorado River Basin. *Hydrological Processes*, *29*(26), 5397–5413. https://doi.org/10.1002/hyp.10569

Sturm, M., Goldstein, M. A., & Parr, C. (2017). Water and life from snow: A trillion dollar science question. *Water Resources Research*, *53*(5), 3534–3544. https://doi.org/10.1002/2017WR020840

Sun, S., Jin, J., & Xue, Y. (1999). A simplified layer snow model for global and regional studies. *J. Geophys. Res*, *104*(D16), 19587–19597.

Sun, S., & Xue, Y. (2001). Implementing a new snow scheme in Simplified Simple Biosphere Model. *Advances in Atmospheric Sciences*, *18*(3), 335–354. https://doi.org/10.1007/BF02919314

USGS. (2004). *SLC-off Gap-Filled Products Gap-Fill Algorithm Methodology*. https://www.usgs.gov/media/files/landsat-7-slc-gap-filled-products-phase-two-methodology

Wrzesien, M. L., Pavelsky, T. M., Durand, M. T., Dozier, J., & Lundquist, J. D. (2019). Characterizing Biases in Mountain Snow Accumulation From Global Data Sets. *Water Resources Research*, *55*(11), 9873–9891. https://doi.org/10.1029/2019WR025350

Xu, Y., Jones, A., & Rhoades, A. (2019). A quantitative method to decompose SWE differences between regional climate models and reanalysis datasets. *Scientific Reports*, *9*(1), 16520. https://doi.org/10.1038/s41598-019-52880-5

Xue, Y., Sun, S., Kahan, D. S., & Jiao, Y. (2003). Impact of parameterizations in snow physics and interface processes on the simulation of snow cover and runoff at several cold region sites. *Journal of Geophysical Research: Atmospheres*, *108*(D22). https://doi.org/10.1029/2002JD003174

Yan, H., Sun, N., Wigmosta, M., Leung, L. R., Hou, Z., Coleman, A., & Skaggs, R. (2020). Evaluating next-generation intensity–duration–frequency curves for design flood estimates in the snow-dominated western United States. *Hydrological Processes*, *34*(5), 1255–1268. https://doi.org/10.1002/hyp.13673

Yueh, S., Shah, R., Xu, X., Elder, K., Margulis, S., Liston, G., Durand, M., Derksen, C., & Elston, J. (2018). UAS-based P-band signals of opportunity for remote sensing of snow and root zone soil moisture. *Sensors, Systems, and Next-Generation Satellites XXII*, *10785*, 107850B. https://doi.org/10.1117/12.2325819

Zeng, X., Broxton, P., & Dawson, N. (2018). Snowpack Change From 1982 to 2016 Over Conterminous United States. *Geophysical Research Letters*, *45*(23), 12,940-12,947. https://doi.org/10.1029/2018GL079621

CHAPTER 3

Characterizing snow-streamflow droughts in the Western U.S. and the unpredictable case of water year 2021

Ongoing drought represented as a billion-dollar natural disaster affects 75 million of people in the Western U.S. (WUS). Based on the newly developed snow reanalysis data and in situ measurements, the severity of snowmelt and streamflow droughts are quantified over study period Water Years (WYs) 1988 to 2021. Although snowmelt is often used as the predictor of streamflow historically, the severity of snowmelt and streamflow droughts are not always coherent. Aggregated over 20 basins in the Sierra Nevada (SN) and Upper Colorado River Basin (UCRB), WY 2015 and 2018 were the driest snowmelt years, respectively, whereas 2021 and 2002 were the driest streamflow years, respectively. The aggregated-snowmelt in 2021 were at the 15th percentile in both SN and UCRB, whereas aggregated-streamflow was at the 3rd and 6th percentiles, respectively. Among snow-streamflow drought basin-years, 2021 is the only year that all basins overestimated streamflow percentiles by 50% based upon the respective snowmelt percentiles. This implies that other potential factors contribute to 2021 snow-streamflow drought. As selected as the study year due to the widespread unpredictive streamflow, 2021 had antecedent soil moisture drought over all the basins in the SN, and half of the basins in the UCRB. Additionally, basins to the north of Tuolumne had spring rainfall drought in 2021. Together, the extreme 2021 streamflow drought was a compound event modulated by contributors linking snow, soil moisture, and streamflow.

3.1 Introduction and Background

Droughts, especially in semi-arid regions like the Western U.S. (WUS), are an ongoing concern (Siirila-Woodburn et al., 2021; Williams et al., 2020) that jeopardize ecosystem services and socioeconomics including water supply, crop growth, fish and wildlife habitats, hydropower generation, and water recreation (Barnett et al., 2005; Bales et al., 2006; Viviroli et al., 2011; Huning & AghaKouchak, 2020). In 2021, up to ~75% of the WUS suffered from "extreme or exceptional" drought conditions (Williams et al., 2022), which represented a billion-dollar natural disaster that affected approximately 75 million people (NCEI, 2022; U.S. Census Bureau, 2020). In California, 2021 streamflow was the second lowest since 1905 (CADWR, 2021), and the severe drought continued in 2022. In mid-August 2021 along the Colorado River, reservoir storages in Lakes Mead and Powell, the largest and second largest reservoirs by capacity in the U.S., dropped to 30% – 40% of capacities (NASA Earth Observatory, 2021). Even worse, the storage of Lakes Mead by the end of August 2022 further dropped to historical low, 28% of capacity (NASA Earth Observatory, 2022).

In the WUS, seasonal snowmelt in key basins historically contributes to as much as 75% of total available water supply (Stewart et al., 2004; Li et al., 2017; Siirila-Woodburn et al., 2021). Hence in situ snow water equivalent (SWE; usually 1 April) is often used as a proxy for the total snow water resource availability (Aguado, 1990; Margulis et al., 2016; Nolin et al., 2021) and as a key input to statistical water supply forecasts. In 2021, California water supply forecasts on 1 April overestimated streamflow by 45-68% in key basins (CADWR, 2021). The overestimation of streamflow suggests that the historical relationship among streamflow and predictors derived from in situ observations such as SWE and precipitation (PPT), poorly characterized the streamflow generation and drought in 2021 (Lapides et al., 2022). However,

due to the lack of spatially-distributed snow data, the role of snow and other potential causes of the 2021 streamflow drought have not been examined in detail.

In this paper, we utilize a novel snow reanalysis dataset along with in situ datasets to quantify the spatial distribution of snow severity and its contribution to snow-streamflow drought. Based on the data availability, the roles of snowmelt and other contributors in streamflow is assessed over Water Years 1988 to 2021. The scientific questions addressed include: 1) What was the space-time variability of snow droughts in the WUS? 2) To what extent was snow drought responsible for the streamflow drought? and 3) What was the potential role of other contributors to the streamflow drought? The insights gained by examining the droughts over the past three decades can be used to understand and mitigate future anomalies, including the continuing effects of ongoing multi-year droughts (Williams et al., 2022).

3.2 Study domains, datasets, and methods

3.2.1 Study domains

Snow drought severity is examined across the WUS (Fig. 3.1a), but with a focus on drought-impacted basins in the Sierra Nevada (SN, Fig. 3.1b) and the Upper Colorado River Basin (UCRB, Fig. 3.1c). These sub-domains are chosen for their importance in water supply by providing water for more than half of the WUS (US Census Bureau, 2020). Basins in each sub-domain are selected for analysis based on the availability of naturalized streamflow data.

Among the basins analyzed, the Feather basin generates streamflow that drains to Lake Oroville, the second-largest reservoir in California and a key feature of the California State Water Project. Streamflow generated from the Kern basin drains to Lake Isabella, the second-largest reservoir in southern California. Lake Isabella, Folsom Lake and Oroville Lake provide

flood protection for downstream areas in addition to key water supply for irrigation, hydropower, and other uses in California's Central Valley and Sacramento Delta regions, respectively. In Colorado, snowmelt from the Colorado Headwaters (hereafter "Headwaters") and Gunnison basins contribute ~ 22% and 10% respectively of the total streamflow above Imperial Dam. Both basins are part of the Colorado River Basin, which supplies drinking water for 40 million people across the Southwestern U.S. and Mexico and is an important water resource for regional irrigation and hydropower (Xiao et al., 2018).

3.2.2 Datasets and methods

Based on data availability, WYs 1988-2021 are chosen as the study period, with 2021 highlighted as the extreme drought year of interest. The data-centric focus of this work is on understanding how OCT-JUL streamflow is impacted by snowmelt, with additional contributors examined including pre-snow precipitation (PPT) as a proxy for antecedent soil moisture and spring (APR-JUL) PPT. To acknowledge the uncertainty of data from different sources, percentiles are used throughout to quantify each metric relative to the longer historical record, with those having values less than the 30th percentile classified as "drought" conditions (Hatchett et al., 2022). More details on each dataset and the associated contributors are provided below.

3.2.2.1 Snow dataset

To better examine the role of snow on the drought, spatially continuous SWE estimates are taken from a newly developed Western U.S. – Snow Reanalysis dataset (WUS-SR; Fang, Liu and Margulis., 2022) that provides daily estimates at a spatial resolution of 16 arcseconds (~480 m) over the WUS from WYs 1985 to 2021. The dataset is generated using a retrospective snow reanalysis framework that assimilates historical Landsat fractional snow-covered area estimates over a WY to update snow water equivalent (SWE) and other variables derived from a land

surface model coupled with a snow depletion curve. SWE estimates have been validated against over 25,000 in situ station-years of data and with an overall correlation coefficient of 0.77. The new dataset allows for computing spatiotemporally continuous snow drought metrics at high resolution. Ancillary data products of the WUS-SR include meteorological drivers (derived from MERRA2 with downscaling and bias-correction, Margulis et al., 2019) such as PPT, at the same spatial and temporal scale.

As a proxy for snowmelt contributions to streamflow, the cumulative daily SWE losses (McCrary & Mearns, 2019) are computed at the pixel-scale (Fig. 3.1d) over the OCT-JUL integration window. Cumulative daily SWE loss that includes snowmelt and other losses in both the accumulation and melt seasons is defined as the snowmelt metric (Fig. 3.1d, red line). The OCT-JUL snowmelt proxy (hereafter simply referred to as "snowmelt") is computed by integrating the SWE losses (Fig. 3.1d, yellow bars) over OCT-JUL for each pixel. This metric containing actual snowmelt and other losses in both the accumulation and melt seasons is designed to capture the integrated seasonal snow contributions to streamflow as opposed to traditional single-day snapshots that are sensitive to timing, such as peak SWE and 1 April SWE (Appendix A.1, Fig. A.1a). The use of the OCT-JUL window is meant to provide a more complete picture of snowmelt instead of the commonly used APR-JUL period. APR-JUL only partially captures the snowmelt amount in years when SWE peaks before 1 April (e.g., WY 2015; Fig. A1b) and neglects the increasingly important contributions in winter (Musselman et al., 2021).

Other diagnostics, including an antecedent soil moisture proxy and spring rainfall are also derived from the WUS-SR and/or its ancillary inputs. The antecedent soil moisture proxy is discussed in detail in Section 2.2.3. APR-JUL PPT is aggregated over snowy domain (median

long-term SWE greater than 5 cm) to represent springtime PPT (mostly rainfall). All factors described herein are analyzed in terms of their percentiles (rank of data to total number of data) over the analysis period. The pixel-wise soil moisture proxy is averaged over basins while pixel-wise OCT-JUL snowmelt and APR-JUL PPT are summed over basins.

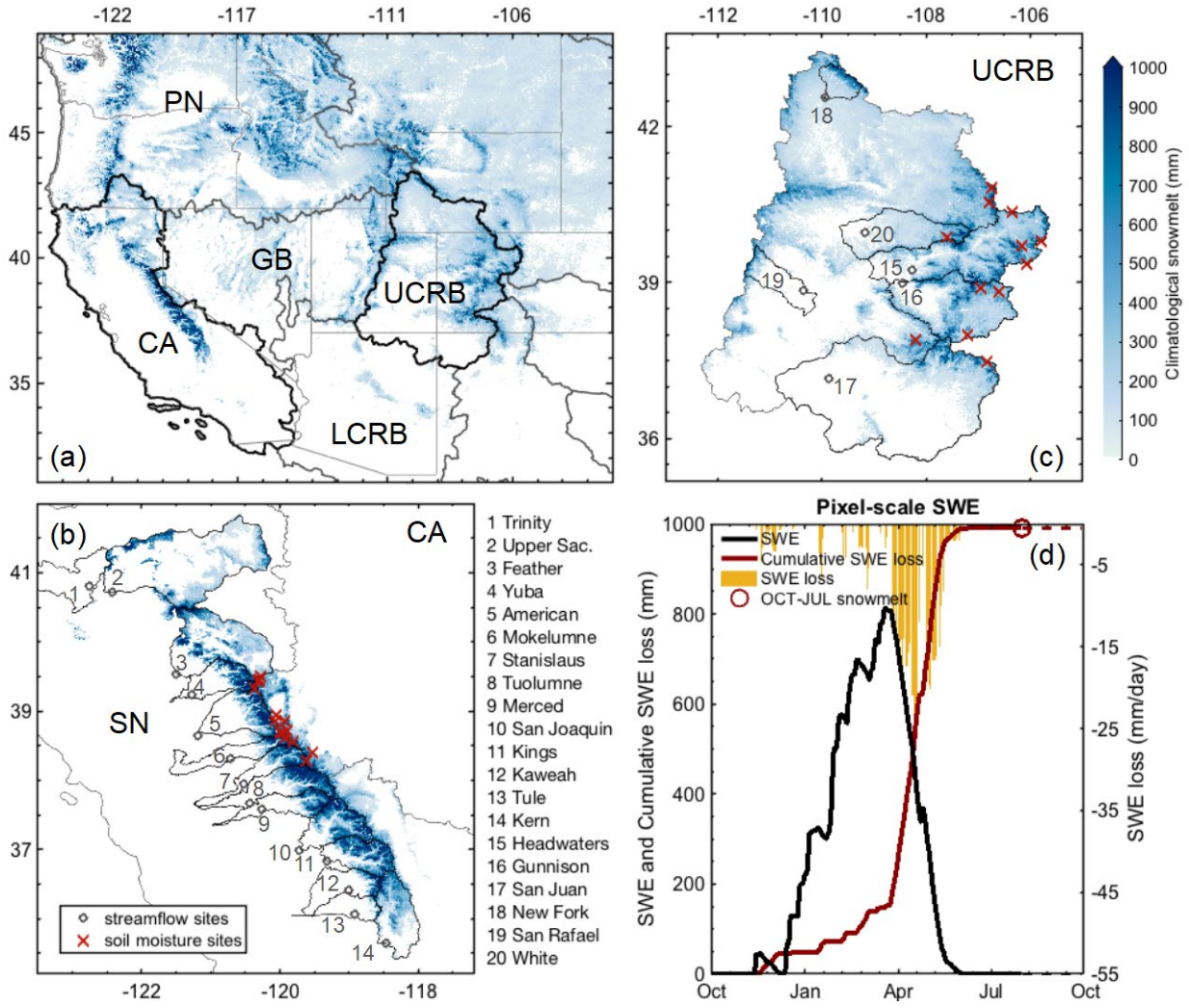

Figure 3.1 Climatological (mean over WYs 1988-2021) snowmelt distribution over (a) WUS, (b) Sierra Nevada, SN and (c) Upper Colorado River Basin, UCRB. (b) and (c) show in situ streamflow sites (gray) and soil moisture sites (red). (d) Schematic illustration of pixel-scale SWE, daily SWE losses, cumulative seasonal SWE losses, and OCT-JUL snowmelt (sample pixel: 39.98°N, 121.34°W in WY 2021). The other sub-domains in the WUS include: Pacific Northwest (PN), Great Basin (GB), and Lower Colorado River Basin (LCRB).

3.2.2.2 In situ datasets

Streamflow data is collected from the California Data Exchange Center (daily full natural flow) for sites in the SN, and from the United States Geological Survey (monthly adjusted streamflow volumes) for sites in Headwaters and Gunnison from the Snow Telemetry network (SNOTEL; Appendix A.2, Table A.1, A.2). Daily naturalized flow over the SN basins is integrated to monthly values. A year is eliminated for analysis if more than one month has missing data for 15 days or more. At each streamflow gauge, OCT-JUL integrated naturalized streamflow is computed and expressed as percentiles to analyze streamflow conditions.

Soil volumetric water content (VWC) at 5 cm, 20 cm, and 50 cm soil depth is collected from SNOTEL/Soil Climate Analysis Network (SCAN) sites with more than 15 years of soil moisture data (25 sites in the SN and 12 sites in the UCRB). It is assumed that VWC at 5, 10, 20 cm represent soil water at 0 – 10 cm, 10 – 30 cm, 30 – 70 cm (Harpold et al., 2017). Depth-weighted VWC is computed to represent the average soil moisture at each site. In situ SWE and precipitation at corresponding soil moisture sites are collected to develop a soil moisture proxy described in Section 2.2.3. Due to the limited number of in situ stations that have both soil moisture and downstream streamflow measurements, Forestdale (in the SN) and Berthoud Summit (in the UCRB) are selected as illustrative sites to demonstrate the role of antecedent soil moisture in modulating the snow contribution to streamflow (Section 3.3). Although Forestdale is stationed in an eastern-draining SN basin, it is one of the few in situ soil moisture stations with a nearby downstream streamflow gauge.

3.2.2.3 Antecedent soil moisture proxy

In situ VWC measurements are very limited in space and time in the SN and UCRB. Hence a proxy for antecedent (pre-snow) soil moisture is used to analyze the role of soil moisture

on streamflow in the basins. To estimate the antecedent soil moisture conditions more broadly over the SN and UCRB study regions, pre-snow PPT computed from gridded snow reanalysis is used as a proxy for pre-snow soil moisture. The extent to which such a proxy has useful information was examined by investigating the relationship between the observed pre-snow PPT and pre-snow soil moisture condition at in situ sites within the SN and UCRB regions. Pre-snow PPT is defined as the cumulative in situ PPT from 1 September (i.e., the last month in the previous WY) to the snow start day of the current WY, and pre-snow VWC is defined as VWC at the snow start day. The snow start day is defined as the first day when in situ SWE is greater than 2.5 mm for at least 5 continuous days.

For each year, pre-snow PPT and soil moisture are averaged across all sites to get site-averaged values over the data record for each region (i.e., SN and UCRB). Site-averaged pre-snow PPT and soil moisture are further normalized by subtracting the long-term means and dividing by the standard deviation values across all years in each region. Linear regression is used to fit the normalized site-averaged precipitation and soil moisture over the data record for each region separately. The results and application are further discussed in Section 3.3.

3.3 Results and discussion

3.3.1 Interannual snow and streamflow conditions

Based on the WUS-aggregated snowmelt computed from the snow reanalysis dataset, WYs 1988, 1990-1992, 1994, 2000, 2005, 2012, 2015, and 2021 are classified as snow drought years (Fig. 3.2a). Among the snow drought years, 2015 has the lowest WUS-wide snowmelt percentiles over the record. The WUS-wide snowmelt in 2021 was at the 24th percentile, the 8th driest year (Fig. 3.2a). Since in situ streamflow measurements are not available over the full WUS, only the WUS-wide snowmelt percentile is shown. In both SN and UCRB (Fig. 3.2b and

2c), the interannual variability in basin-averaged snowmelt and streamflow percentiles are generally in agreement. However, in a given WY, water conditions are not always consistent between SN and UCRB. In terms of snowmelt, 2015 was the driest year over the record in the SN, whereas 2018 was the driest year in the UCRB. The lowest streamflow occurred in 2021 and 2002 in the SN and UCRB, respectively. The SN-wide and UCRB-wide snowmelt in 2021 were both at the 15th percentile, whereas streamflow was at the 3rd and 6th percentiles, respectively. WY 2021 was one of the only two years (1990 and 2021) where the SN and the UCRB jointly experienced drought (less than 30th percentile) in both streamflow and snowmelt. Moreover, among these joint snow-streamflow drought years, only 2021 had streamflow that is notably less than the snowmelt percentile in both sub-domains (Fig. 3.2b and c).

While it is expected that the percentiles of streamflow and snowmelt will be correlated in the snow-dominated WUS, the annual variations in snowmelt and streamflow percentiles can be categorized into three cases that may occur in drought and non-drought years: 1) snowmelt and streamflow percentiles are comparable. 2) snowmelt is greater than streamflow percentile and 3) snowmelt is less than streamflow percentile streamflow percentile. Although these three cases can occur in any year, this work specifically focus on snow-streamflow drought years. For case 1 (e.g., WYs 2014, 2020 in the SN, and 2002, 2012 in the UCRB), streamflow droughts are likely primarily driven by snow drought. For case 2 (e.g., 1988 and 2021 in the SN, 1989 and 2021 in the UCRB), in addition to snowmelt, other factors linked to water losses/deficits such as low antecedent soil moisture, a lack of spring rainfall or higher evapotranspiration are likely contributing to streamflow drought. Streamflow in this case may be overestimated from the historical snow-streamflow relationship. In contrast, for case 3 (e.g., 2012 and 2018 in the SN, 1991 and 2015 in the UCRB), additional water inputs like high spring rainfall might off-set the

reduction of streamflow from low snowpacks resulting in a higher streamflow than snowmelt percentile. In this case, streamflow may be underestimated based on the historical snow-streamflow relationship. Under a drought condition, an overestimation of streamflow can have significant consequences with respect to water supply and its downstream allocation. Therefore, case 2 is of primary interest in this study, where WY 2021 falls into this category.

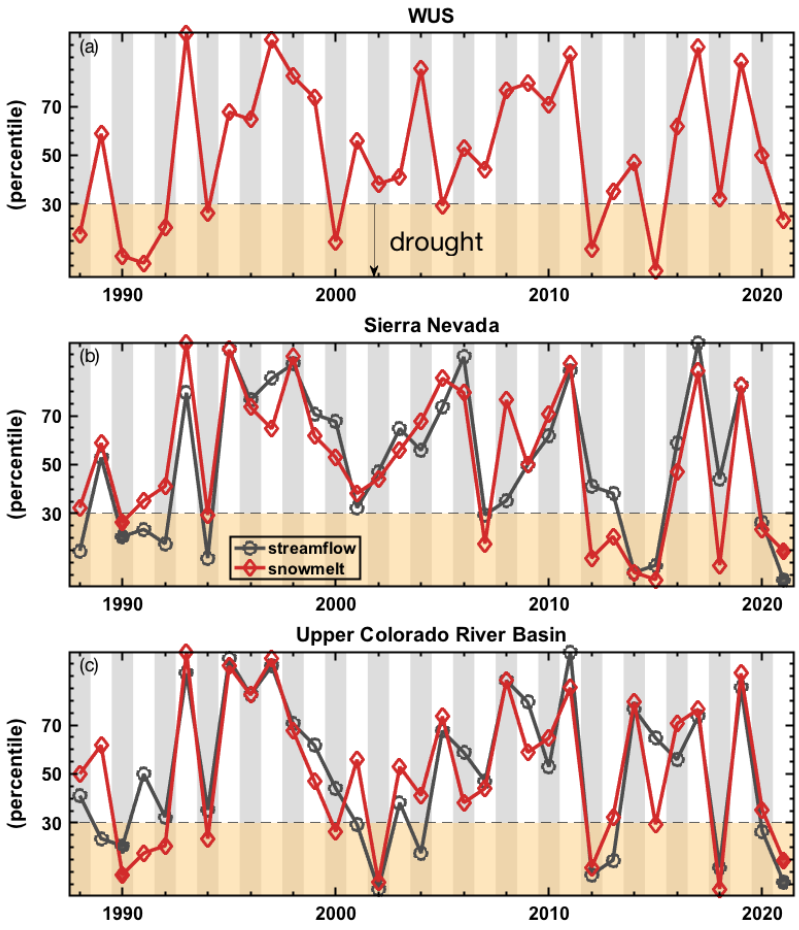

Figure 3.2 (a) Snowmelt percentile time series for the WUS domain shown in Fig. 3.1 over WYs 1998 to 2021. (b) and (c) Streamflow (circles) and snowmelt (diamonds) percentile time series aggregated from basins in the Sierra Nevada (SN) and Upper Colorado River Basin (UCRB) sub-domains shown in Fig. 3.1. The aggregated streamflow percentiles are computed from available streamflow data in the SN and UCRB. The aggregated snowmelt percentiles are computed from snow reanalysis data. Years with filled markers in SN and UCRB represent conditions of joint snow-streamflow drought occurring in both SN and UCRB.

For SN and UCRB basins with streamflow observations, linear regression was used to fit OCT-JUL snowmelt and streamflow percentiles over WYs 1988 to 2021 (Fig. 3.3). The simple linear regression model is used to quantify the relationship between snowmelt and streamflow by leaving out the impact of other known factors, and to identify years where the predictability of streamflow from snowmelt is low based on the historical relationship. Based on the derived relationships, snowmelt explains the majority of variance in streamflow with R^2 ranging from 0.5 at San Rafael in UCRB to 0.86 at Kings in SN. Overall, the power of snow explaining variations in streamflow (R^2) is higher for basins in SN where snow is more dominant – such as the southern basins of Kern or Kings – than those in UCRB (Fig. 3.1b, c). In UCRB, snowmelt has a stronger relationship with streamflow for Headwaters and Gunnison basins with R^2 of 0.8 and 0.78, respectively. The relative predictive error:

$$\text{Relative Predictive Error} = \frac{Flow_{predicted} - Flow_{observed}}{Flow_{observed}} \quad (6)$$

is used to quantify the degree to which streamflow is poorly predicted in any given year. *Flow* represents OCT-JUL streamflow in percentile. A positive relative predictive error represents that the predicted value overestimates observed streamflow. A higher relative predictive error in absolute value means the predicted value is further away from the observation. For example, in the Feather basin (Fig. 3.3), the relative predictive error in WY 2021 is computed as the difference of the predicted streamflow percentile (17^{th}, black square) and the observed streamflow percentile (3^{rd}, red circle), divided by the observed percentile (3^{rd}, red circle). This yields a predictive relative error of 467%.

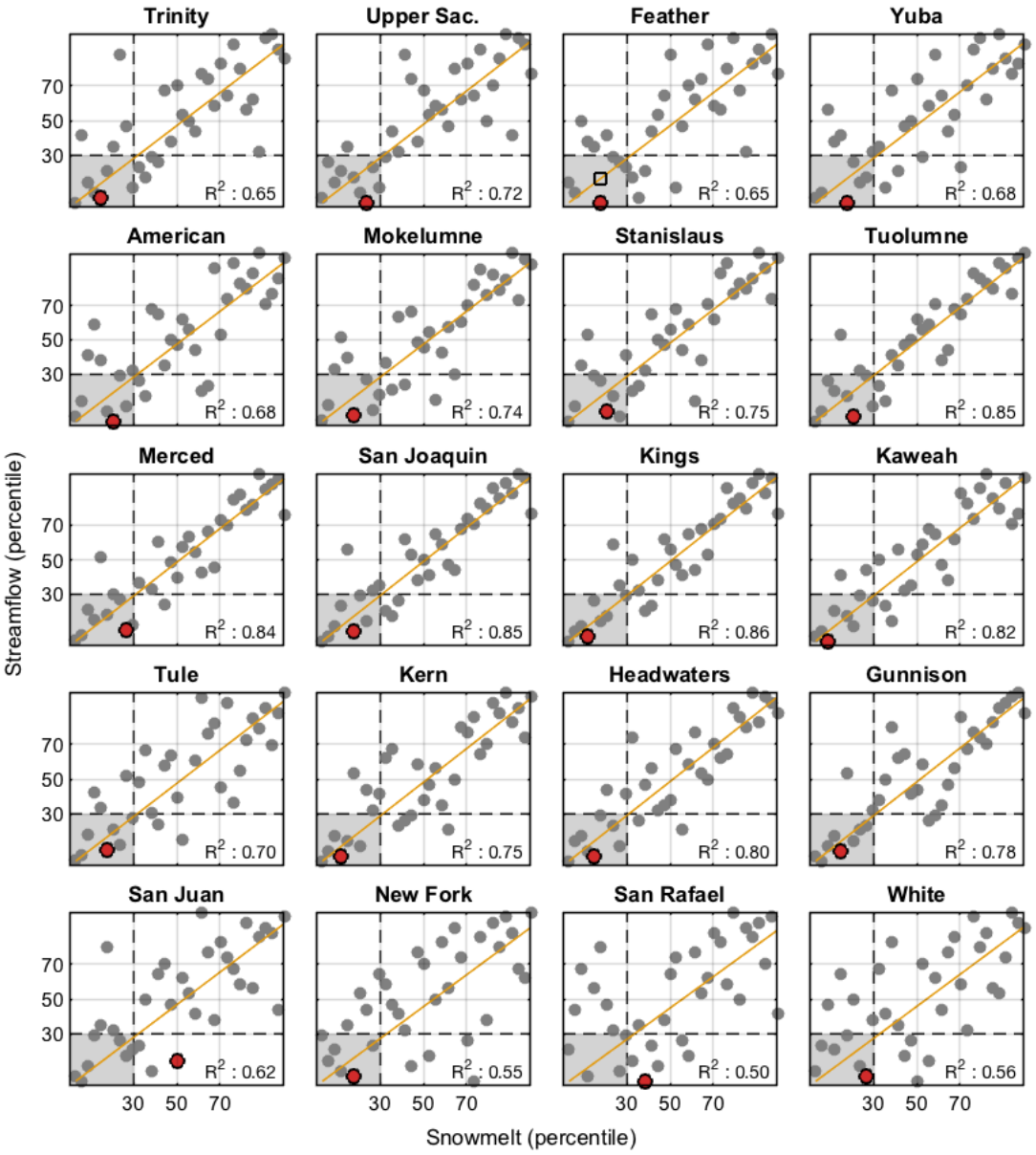

Figure 3.3 Scatter plot of OCT-JUL snowmelt and streamflow (percentiles over WYs 1988-2021). The grey shaded areas represent snow-streamflow drought years with both snowmelt and streamflow below the 30th percentile. Solid lines are regression lines (with zero intercepts), where R^2 is the coefficient of determination. Red circles are the observed values in WY 2021. The square symbol in the Feather basin represents the predicted streamflow in WY 2021.

For each basin, the 10 driest (less than 30th percentile) streamflow and snowmelt WYs are highlighted separately in Fig. 3.4a and b. In the SN (14 basins), 18 years had at least one basin in snowmelt drought, with 9 of those years having drought across 12-14 basins, 6 years having only

one basin in (mild) snow drought and the other 3 years having between 3-7 basins in snow drought. For streamflow drought, 18 years had at least one basin in streamflow drought, with 8 of those years having drought across 12-14 basins, 3 years having only 1 basin in (mild) snow drought, and the remaining years having 2-7 basins in snow drought. In the UCRB (6 basins), 22 years and 20 years had at least one basin in snowmelt drought and streamflow drought, respectively. Among the snowmelt drought years in the UCRB, 8 out of 22 years had drought over 4 basins, 3 years had drought across 3 basins, and the rest years had drought at 1-2 basins. In both SN and UCRB (20 basins), 24 years had at least one basin in snowmelt drought with 2 (2012 and 2021) of those years had snowmelt drought across 18 basins. Similarly, 24 years had at least one basin in streamflow drought, with 2 (1990, 1994) out of these years having streamflow drought across 17 basins, 1 year (2021) having streamflow across all 20 basins.

In WY 2021, 18 out of the 20 basins across the SN and UCRB had snowmelt drought, with only the San Juan and San Rafael not exhibiting conditions (Fig. 3.4a). Streamflow drought was widespread over all sub basins in WY 2021 (Fig. 3.4b). Based on the snow-streamflow regression relationships, predicted streamflow percentiles were overestimated by 50% over half of the basins across the SN and UCRB in 1992 and 2021(Fig. 3.4c). On the contrary, in 2012 and 2018, predicted streamflow percentiles were underestimated by 50% over half of the basins. For snow-streamflow drought years where snowmelt and streamflow were both less than 30th percentile, ~ 19% of the basin-years had negative predictive error lower than -50% and ~ 28% of the basin-years had positive predictive error greater than 50%. WY 2021 is the only year where all the basins overestimate streamflow percentiles by more than 50% based upon the respective snowmelt percentiles.

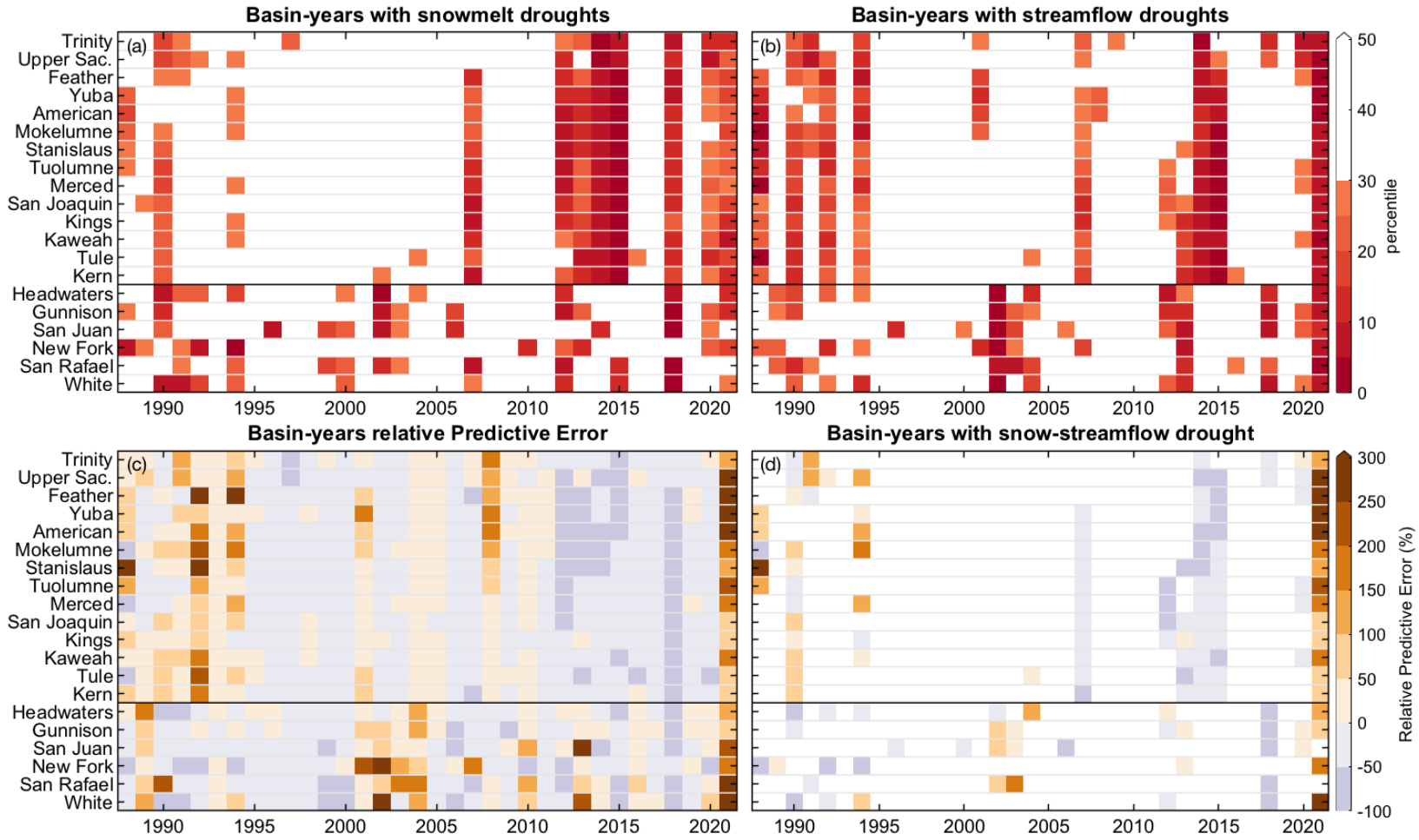

Figure 3.4 (a) and (b) Basin-years with snowmelt drought and streamflow drought in basins with available streamflow data over the study period. (c) Relative predictive errors over the full record. (d) Relative predictive errors for just snow-streamflow drought years. A positive relative predictive error represents an overestimation of streamflow, whereas a negative value represents an underestimation of streamflow.

3.3.2 Severity of WY 2021 snow and streamflow drought

WY 2021 represented a widespread low-snow year: ~ 40% of the snow-dominated WUS had snowmelt below the 30th percentile (Fig. 3.5a). The snow drought was especially pronounced over the SN (Fig. 3.5b) and the UCRB (Fig. 3.5c) with region-aggregated snowmelt corresponding to the 15th and 24th percentiles, respectively. Over the other basins, snowmelt was higher, but still below the long-term median. These results agree with other assessments that report 2021 as a low-snow year but not exceptionally low relative to the historical record (CADWR, 2021; Western Water Assessment, 2021). However, the severity of snow drought is spatially heterogeneous. For example, the southern part of the SN had lower snowmelt (compared to its long-term median) than the northern SN. In the UCRB, the Headwaters and Gunnison basins had more severe snow droughts than the rest of the basin.

Streamflow scarcity in WY 2021 was more extreme than snowmelt. In the western SN, naturalized streamflow was below the 10th percentile in all basins, however snowmelt percentiles were much higher than streamflow percentiles (Fig. 3.5d). For basins to the north of San Joaquin, the differences between snowmelt and streamflow percentiles were more than 10% except for the Trinity. For example, for both the Feather and American basins in the northern SN, streamflow was extremely low (3rd percentile, i.e., driest over the record), in contrast to a much less extreme snowmelt condition (18th and 21st percentile, respectively). For those to the south of San Joaquin, streamflow drought was still more severe than snowmelt drought with snowmelt and streamflow differences ranging between 5% to 10%. Streamflow at the Kern basin (southern SN) was at the 6th percentile (second lowest) while snowmelt was at the 12th percentile. In the UCRB (Fig. 3.5e), snowmelt percentiles are more than 5% greater than streamflow percentiles. The Gunnison basin had the lowest difference in that the streamflow was at the 9th percentile, while snowmelt

was at the 15th percentile. In contrast, streamflow was at the 6th percentile given the same rank of snowmelt (15th) at the Headwaters as the Gunnison. The snowmelt percentiles at San Juan and San Rafael were all above the 30th percentile which are not classified as a drought condition.

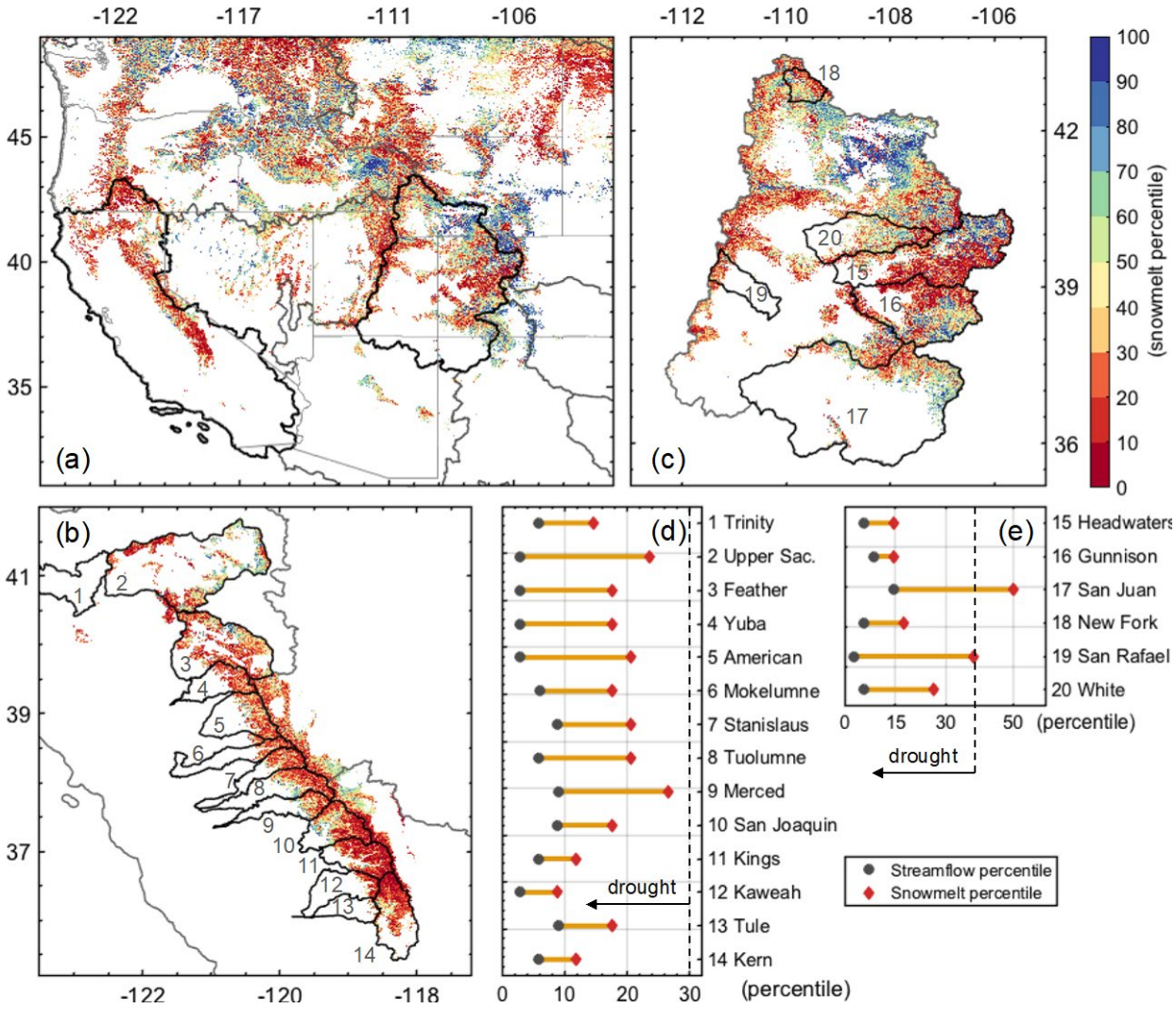

Figure 3.5 WY 2021 OCT–JUL snowmelt percentile (shown for snow-dominated pixels with long-term median peak SWE > 5 cm) in (a) WUS, (b) SN, and (c) UCRB. (d) and (e) show paired streamflow (black circles) and snowmelt (red diamonds) percentiles at basins in the SN and UCRB, respectively.

While the snowmelt was low in WY 2021, it is higher than would be expected if it were the main driver of the observed low streamflow. This is evident in the high relative predictive

error based on the historical snow-streamflow relationship (Fig. 3.4). This suggests that other factors such as antecedent soil moisture and spring rainfall were at a play in leading to the low observed OCT-JUL streamflow. The following sections discuss the potential additional contributors to streamflow drought in WY 2021.

3.3.3 Impact of antecedent soil moisture on snow contributions to streamflow

Antecedent (pre-snow) soil moisture is an indicator for how much of the soil reservoir must be filled by snowmelt and/or rainfall before generating streamflow and is therefore a potential contributor to variations in snowmelt-driven streamflow. Streamflow is generally insensitive to snowmelt before soil moisture exceeds soil water storage capacity (Seyfried et al., 2009). Therefore, the relationship between snowmelt and streamflow can be weakened by low antecedent soil moisture conditions that require a greater amount of snowmelt to fill up the soil reservoir before triggering streamflow.

To illustrate the evolution of VWC and its impact on streamflow generation from snowmelt, in situ streamflow, VWC, and SWE are illustrated at two of the few sites with collocated data in the WUS: Forestdale (SN, Fig. 3.6) and Berthoud Summit (UCRB, Fig. 3.7). At Forestdale, VWC in WY 2021 began with above-median conditions but remained low during snow accumulation (Fig. 3.6b, 16th percentile at peak SWE day). At Berthoud Summit in the UCRB, VWC remained below 5% (Fig. 3.7b, 6th percentile at peak SWE day) during the entire snow accumulation season. Both sites show that with low antecedent VWC in 2021, it took longer for soil moisture to reach saturation after the peak SWE day than in the highest streamflow years when antecedent soil moisture was high (30 days and 11 days later at Forestdale and Berthoud Summit, respectively).

While in situ soil moisture data is limited, Fig. 3.6f and 3.7d show that the majority of in situ sites in both the SN (19 out of 25) and the UCRB (9 out of 12) exhibited low WY 2021 antecedent soil moisture (less than the 30th percentile). While 2021 SWE was not extremely low, high antecedent soil moisture deficits may have taken up a larger fraction of snowmelt into soil water storage, leaving less snowmelt to generate streamflow. The low antecedent soil moisture indicates an outsized role of soil moisture in 2021 with respect to streamflow. This is consistent with other studies (e.g., Lapides et al., 2022) that show the importance of low antecedent soil moisture in explaining the overestimated streamflow forecast in 2021 in California.

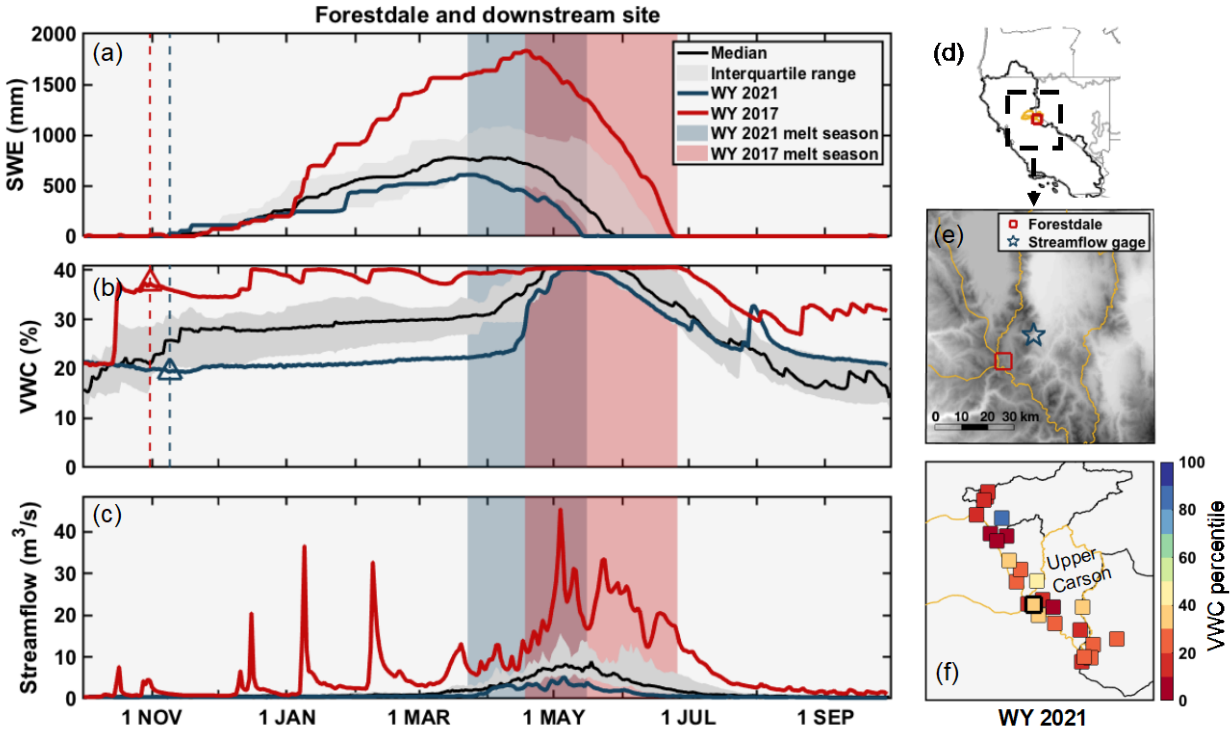

Figure 3.6 (a) in situ daily SWE, (b) depth-averaged VWC and (c) streamflow at Forestdale, for a WY 2021 and for the highest streamflow year on record (WY 2017). The median and interquartile range of VWC across all years are shown for reference. Dashed lines are dates of snow onset, and the '△' symbols indicate antecedent soil moisture. (d) and (e) locations of Forestdale in situ site and downstream streamflow gauge. (f) soil moisture percentiles for 2021 (from record of WYs 2003-2021) at available sites in the SN.

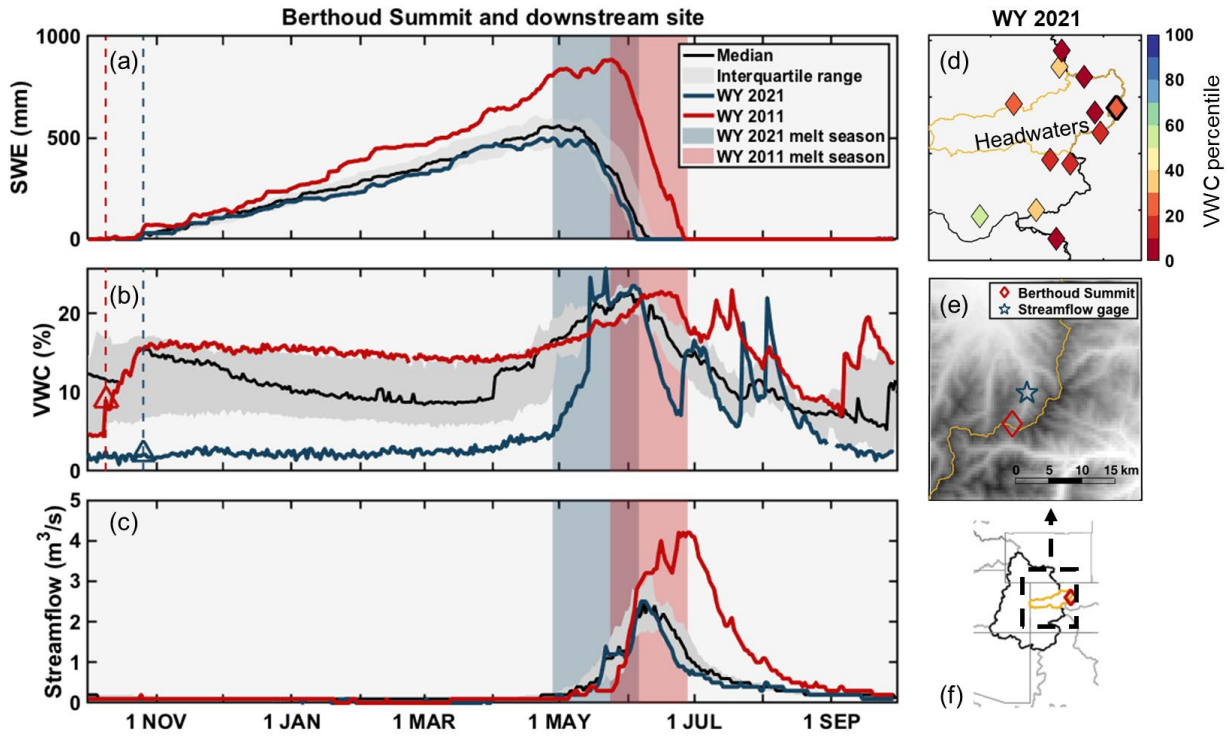

Figure 3.7 Same as Fig. 3.6 but for Berthoud Summit site in the UCRB.

To investigate the role of antecedent soil moisture beyond in situ sites, an antecedent soil moisture proxy is developed based on in situ data and snow reanalysis auxiliary data. Regression results (Fig. 3.8a and b) indicate that the observed site-averaged pre-snow PPT explains more than 68% of the observed pre-snow soil moisture variability over SN and UCRB. Based on the significant relationship, we used gridded pre-snow PPT computed from the WUS-SR aggregated over snowy domain as a proxy for antecedent soil moisture. It should be note that while pre-snow PPT seems to reasonably represent the antecedent soil moisture condition over the SN and UCRB where in situ soil moisture data exists (Fig. 3.6f and 3.7d), it may not be as representative across the entire domain (Fig. 3.8d) because of soil heterogeneity and other factors. Here it is used as an indicator of relative antecedent soil moisture instead of as a quantitative metric.

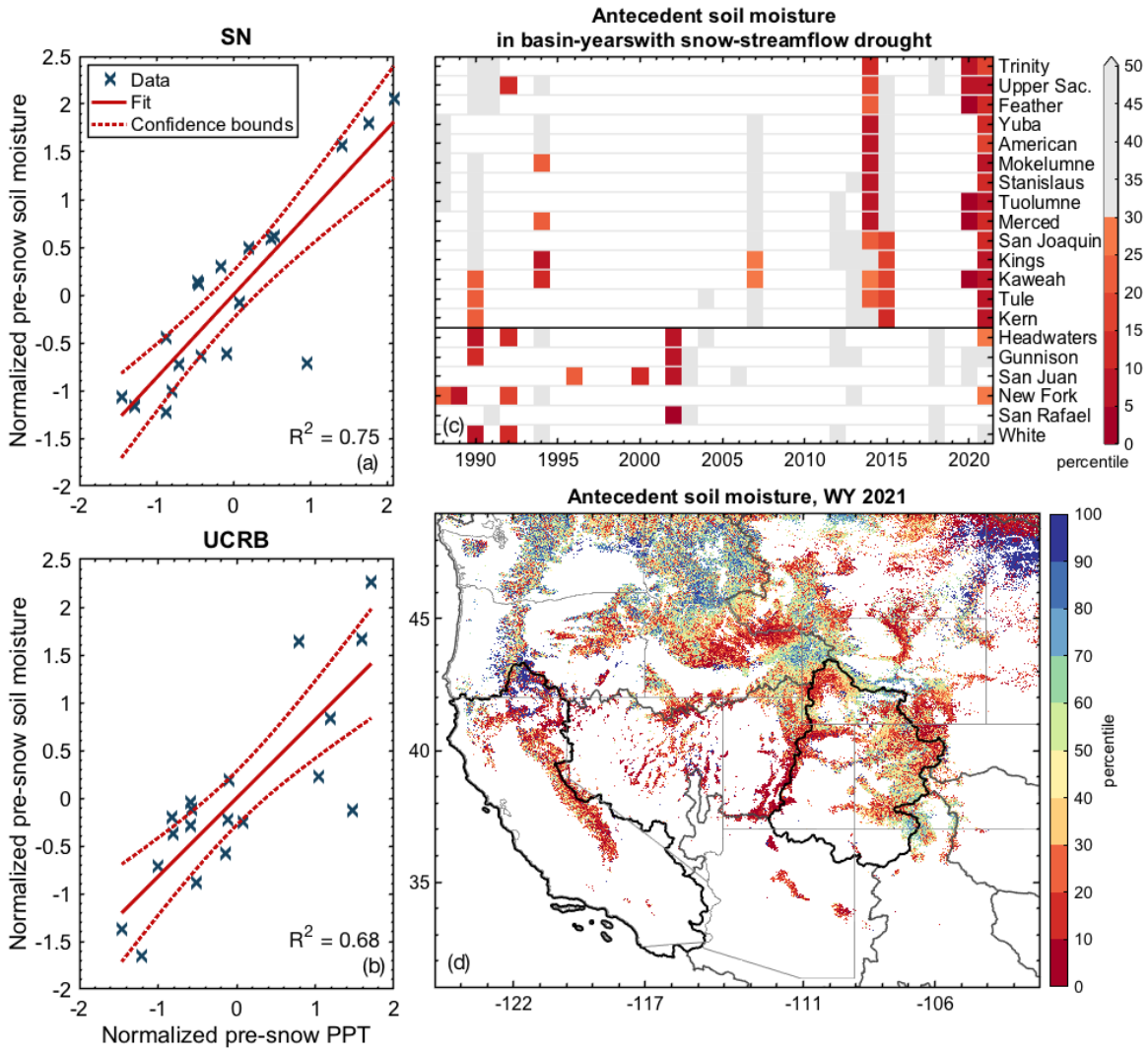

Figure 3.8 (a) and (b) regression plot of normalized site-averaged pre-snow PPT vs. pre-snow soil moisture at in situ sites in the SN and the UCRB (as shown in Fig. 3.1). (c) antecedent soil moisture percentiles for basins and years with snow-streamflow drought conditions. Basin-years without snow-streamflow drought years are masked out in white background. Those with antecedent soil moisture greater than the 30th percentile are further masked out in gray. (d) Map of WY 2021 antecedent soil moisture in the WUS. Pre-snow PPT computed from snow reanalysis data is used as the proxy of antecedent soil moisture shown in (c) and (d).

In the SN, snow-streamflow droughts in WY 2014 and 2021 were accompanied with antecedent soil moisture droughts at over 12-14 basins (Fig. 3.8c). In the UCRB, drought conditions in antecedent soil moisture coincided with snow-streamflow over 3 basins in 1990,

1992 and 2002. In 2021, antecedent soil moisture was widely and significantly low over the SN, whereas only 2 basins in UCRB had mild antecedent soil moisture drought (Fig. 3.8d). Low 2021 antecedent soil moisture was observed in the Great Basin and Lower Colorado River basin (LCRB). The western and northeastern Pacific Northwest (PN) did not have low antecedent soil moisture, whereas the southeastern part had antecedent soil moisture drought in 2021.

3.3.4 Impact of spring rainfall on snow contribution to streamflow

Spring rainfall in snowy areas is another potential contributor to streamflow that can offset or enhance anomalies in snowmelt (Zheng et al., 2018). APR-JUL precipitation from the snow reanalysis dataset is used as the proxy of spring rainfall. Among snow-streamflow droughts in the SN (Fig. 3.9a), spring rainfall drought occurred at over 7 basins to the south of Feather in WY 2007, and to the north of Tuolumne in WY 2021. In the UCRB, 4 out of 6 basins had spring rainfall drought in snowy areas with the exception of New Fork and White in 2002. None of the basins in UCRB experienced 2021 spring rainfall drought. Fig. 3.9b confirms that 2021 spring rainfall is widely lower than normal in the northern SN, but higher than normal in the southern SN and UCRB. PN snowy areas received a very low amount of spring rainfall whereas the LCRB received higher than normal 2021 spring rainfall.

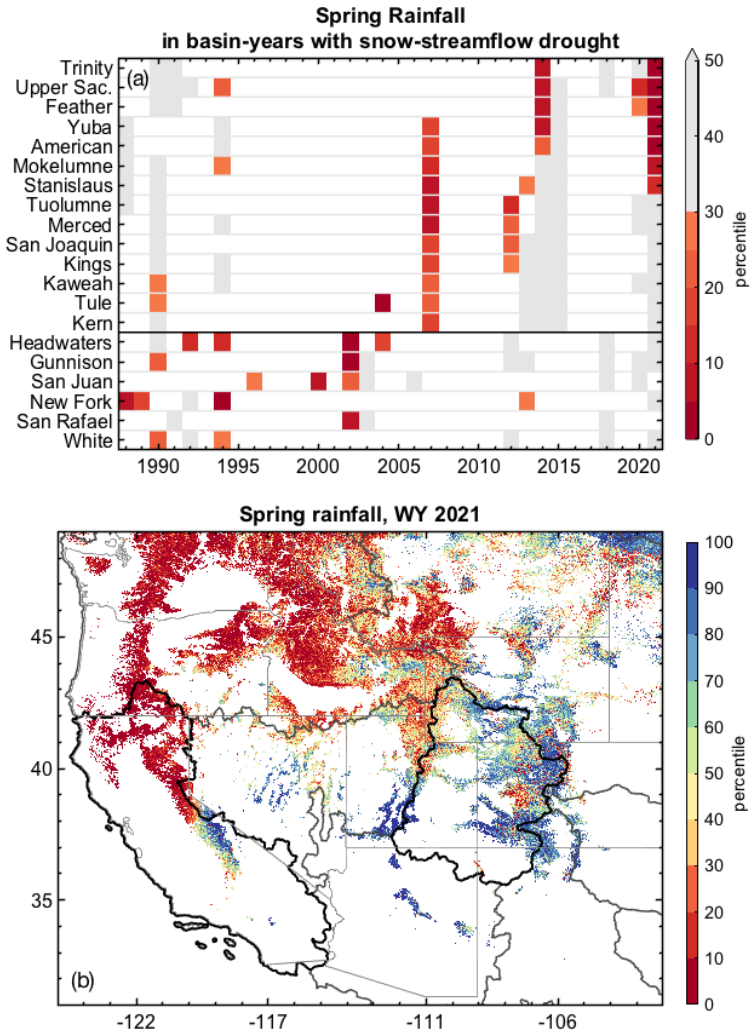

Figure 3.9 (a) spring rainfall (in snow-covered areas) percentiles for basins and years with snow-streamflow drought conditions. Basins and years without snow-streamflow drought years are masked out in white background. Those with spring rainfall greater than the 30th percentile are further masked out in gray. (b) Map of WY 2021 spring rainfall percentile in the WUS.

3.3.5 Characteristics of snow-streamflow droughts

3.3.5.1 Classification of WY 2021 snow-streamflow drought

Based on snowmelt, antecedent soil moisture proxy, and spring precipitation, WY 2021 streamflow droughts in basins in the SN and UCRB are classified into five types. Among all the basins with available data, only San Juan and San Rafael did not have snowmelt drought in WY 2021 (Fig. 3.5). Antecedent soil moisture at San Rafael was at the 6th percentile, suggesting a

large portion of snowmelt may have gone into soil storage. It is hypothesized (but cannot be confirmed due to lack of data) that high evapotranspiration also contributed to the low streamflow given the lack of snowmelt drought in these two basins. For the basins with snow-streamflow drought in WY 2021, antecedent soil moisture was itself below the drought threshold (30th percentile), with the exception of Gunnison and White. As illustrated in Fig. 3.5, the percentile difference between snowmelt and streamflow was only 6% for Gunnison. The difference between snowmelt and streamflow, and the relative predictive error in Gunnison are the lowest in the UCRB. Although antecedent soil moisture is not classified as drought by definition in the White, it was at the 35th percentile. Only basins to the north of Tuolumne in the SN had spring rainfall drought. For those basins, the combination of low snowmelt, low antecedent soil moisture and low spring rainfall together contributed to the low 2021 streamflow.

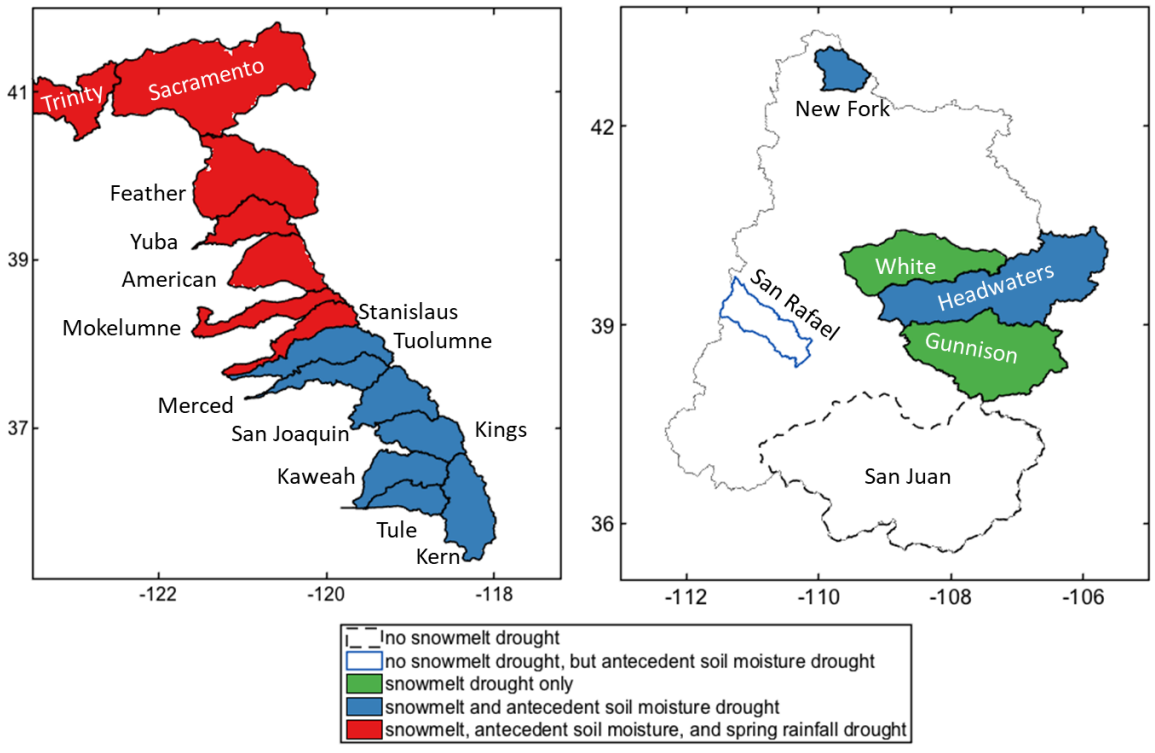

Figure 3.10 Classification of WY 2021 streamflow drought conditions based on snowmelt, antecedent soil moisture, and spring rainfall (over snowy regions) for basins in SN and UCRB.

3.3.5.2 Contributors of snow-streamflow drought years in example basins

To further illustrate the roles of snowmelt, antecedent soil moisture and spring precipitation in streamflow droughts, the Feather, Kern, Headwaters and Gunnison are selected as example basins. These basins are chosen considering their importance for water resource supply (Section 3.2.1) and representation of different types of WY 2021 drought for each domain. For example, in the SN, the Feather watershed is selected to study the scenario that the combination of snowmelt, antecedent soil moisture and spring rainfall drought all contribute to WY 2021 snow-streamflow drought. The Kern and Headwaters are selected to study the scenario that snowmelt and antecedent soil moisture contribute to WY 2021 snow-streamflow drought in SN and UCRB, respectively. The Gunnison is selected to study the scenario that snowmelt was in drought conditions and antecedent soil moisture is close-to drought condition. To examine the relative role of these hydrologic contributors, percentiles of OCT-JUL streamflow, antecedent soil moisture proxy (pre-snow PPT), OCT-JUL snowmelt, and spring rainfall (APR-JUL PPT over snowy regions) are illustrated in Fig. 3.11 for each example basin. For context, to qualitatively assess characteristics of different drought years, the underlying contributors in WY 2021 are compared to another extreme drought year (Fig. 3.11 a-b, e-f; i.e., WY 2015 for the Feather and Kern, and 2002 for the Headwaters and Gunnison).

In the Feather basin, WY 2015 was an extreme snow drought year (Margulis et al., 2016; 3rd percentile), yet it had a higher OCT-JUL streamflow percentile compared to 2021 (Fig. 3.11c). This highlights that other (non-snow) contributors were at work in driving streamflow differences between the two drought years. Antecedent soil moisture and spring rainfall in 2015 were much higher than 2021. Among all example basin-years shown in Fig. 3.11, 2021 in the Feather was the most unpredictable year. It stood out in having less antecedent soil moisture and

spring rainfall inputs, both of which would be consistent with lower streamflow. In the Kern basin, snowmelt and streamflow were lowest in 2015 and exhibited antecedent soil moisture drought conditions. Although spring rainfall in the snowy region was higher than normal, it did not offset the low snowmelt and low antecedent soil moisture. Compared to 2015, snowmelt drought in 2021 is less severe, however antecedent soil moisture drought is more severe and the spring rainfall is closer to normal (Fig. 3.11d). The significantly lower antecedent soil moisture in WY 2021 seems to have offset the slightly higher-than-normal spring rainfall, yielding streamflow close to that in 2015.

Across the UCRB case study watersheds, the 2021 streamflow drought is extreme, but was even more severe in 2002. In both the Headwaters and Gunnison watersheds, 2002 had low antecedent soil moisture and snow (3rd to 9th percentile) and the lowest spring PPT (3rd percentile). Together, these contributors would be expected to contribute to low streamflow conditions, which is consistent with the lowest observed values. The 2021 drought was not as extreme as 2002: streamflow was the second and third lowest in the Headwaters and Gunnison, respectively, despite higher snowmelt percentiles (15th percentile). This can be explained by a similar pattern to 2002 in terms of low antecedent soil moisture and snowmelt. The largest difference between the two years was a much larger spring rainfall in 2021, which likely aided in preventing a much more significant streamflow drought.

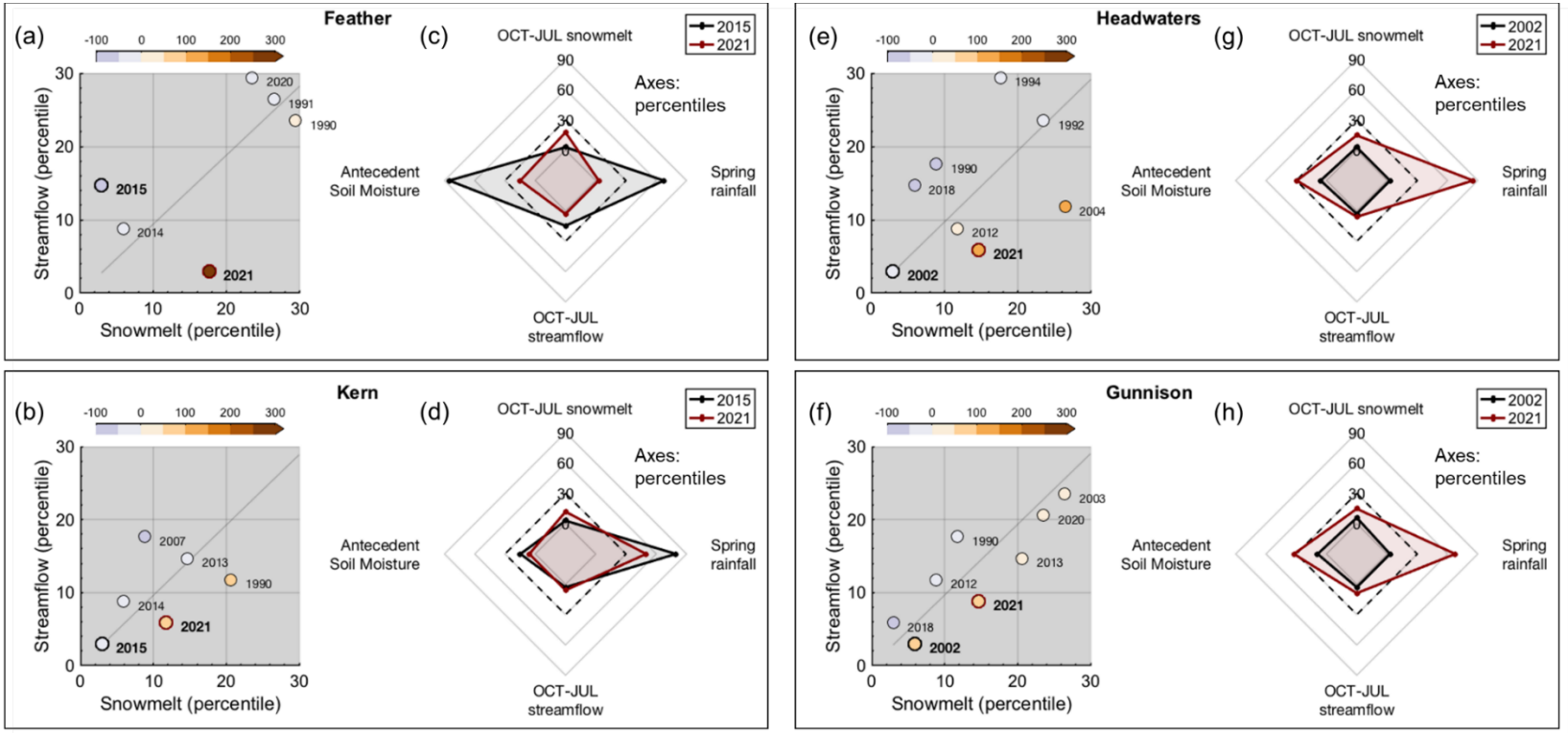

Figure 3.11 (a)-(b), (e)-(f) Scatter plot of OCT-JUL snowmelt and streamflow (zoomed in version of Fig. 3.2) for example basins during snow-streamflow drought years. Each dot is colored by the relative predictive error in percentage. Solid lines are regression lines (with zero intercepts). Years in bold with solid circles are presented as example drought years (WYs 2015 and 2021 in the SN; WYs 2002 and 2021 in the UCRB) for additional analysis. (c)-(d), (g)-(h) Percentiles of OCT-JUL streamflow and other contributors for example basins and years.

3.4 Conclusions and Needed Future Work

Snowmelt and streamflow drought were quantified over the study period (WYs 1988-2021) in the WUS based on snow reanalysis estimates and in situ measurement. Based on the snow reanalysis dataset, WY 2015 had the lowest WUS-wide snowmelt percentiles over the record. Aggregated over the basins examined, 2015 and 2018 were the driest snowmelt years over the record in the SN and UCRB, respectively. Inconsistent with snowmelt drought years, 2021 and 2002 were the driest streamflow years in the SN and UCRB, respectively. 2021 was a widespread snow drought year in the WUS, and especially pronounced in the SN and UCRB that 18 out of 20 had snowmelt drought. However, the corresponding streamflow percentiles were much lower. Among snow-streamflow drought basin-years, 2021 is the only year that all 18 basins overestimated streamflow percentiles by 50% based upon the respective snowmelt percentiles. Hence, while snow drought played an important role in driving the observed low streamflow in 2021, other contributors were also at play (i.e., antecedent soil moisture, springtime rainfall).

Site-averaged pre-snow PPT explains more than 68% of the observed antecedent soil moisture variability over SN and UCRB. Based on the significant relationship, pre-snow PPT from gridded snow reanalysis dataset is used as the proxy of antecedent soil moisture. In the SN, 2014 and 2021 had antecedent soil moisture drought across more than 13 out of 14 of basins. In the UCRB, 2002 had antecedent soil moisture across 4 out of 6 basins. In 2021, over 75% of SN and UCRB in situ sites had low antecedent soil moisture conditions. The results from antecedent soil moisture proxy show that all basins examined had drought in SN, and half of basins had drought in UCRB.

Beyond snow and antecedent soil moisture conditions, basins to the north of Tuolumne in the SN had spring precipitation drought in 2021, which reinforced low streamflow conditions. In contrast, in the southern SN and UCRB, above-normal spring rainfall likely offset what would have otherwise been an even more significant streamflow drought.

Together, these contributors suggest that the extreme WY 2021 streamflow drought was a compound event modulated by 1) antecedent soil moisture (which set the stage for available soil water storage), 2) snowmelt and spring precipitation (as the key sources of spring runoff).

The data-centric study conducted herein cannot fully account for the relative importance of these processes due to the limited extent of soil moisture observations but highlights the likely complexities in how drought manifests itself even in basins where snow is the dominant historical driver. A mechanistic modeling approach (e.g. Lapides et al., 2022) to include other factors such as actual evapotranspiration, which was beyond the scope of this study, could further quantify the various contributors.

To examine and improve future streamflow predictive skill in snow-dominated regions, more widespread and collocated observations of SWE and soil moisture are needed (Seyfried et al., 2009; Harpold et al., 2017; Livneh & Badger, 2020). SWE and soil moisture are the two longest-memory states in the terrestrial water cycle and play a linked role in streamflow generation. Yet no direct and representative measurements are available over larger domains at desired resolutions (Kim et al., 2021). The need for better snow and soil moisture measurements are becoming more urgent as historical relationships are likely to become less robust.

Future warming projections show declining seasonal snowpacks and shifts in streamflow patterns (Barnett et al., 2005; Musselman et al., 2018; Siirila-Woodburn et al., 2021) as well as rising frequency of consecutive snow drought years (Marshall et al., 2019). Under a warmer

climate with potentially more frequent rain-on-snow events (Cooper et al., 2016; Musselman et al., 2018), earlier snowmelt, and drier soil moisture (Cook et al., 2021; Harpold & Molotch, 2015), the anomalous streamflow conditions caused by snowmelt-soil moisture links like those seen in WY 2021 may become more common.

3.5 Bibliography

Aguado, E. (1990). Elevational and latitudinal patterns of snow accumulation departures from normal in the Sierra Nevada. *Theoretical and Applied Climatology*, *42*(3), 177–185. https://doi.org/10.1007/BF00866873

Bales, R. C., Molotch, N. P., Painter, T. H., Dettinger, M. D., Rice, R., & Dozier, J. (2006). Mountain hydrology of the western United States. *Water Resources Research*, *42*(8). https://doi.org/10.1029/2005WR004387

Barnett, T. P., Adam, J. C., & Lettenmaier, D. P. (2005). Potential impacts of a warming climate on water availability in snow-dominated regions. *Nature*, *438*(7066), Article 7066. https://doi.org/10.1038/nature04141

CADWR. (2021). *Water Year 2021: An Extreme Year*. https://water.ca.gov/-/media/DWR-Website/Web-Pages/Water-Basics/Drought/Files/Publications-And-Reports/091521-Water-Year-2021-broch_v2.pdf

Cook, B. I., Mankin, J. S., Williams, A. P., Marvel, K. D., Smerdon, J. E., & Liu, H. (2021). Uncertainties, Limits, and Benefits of Climate Change Mitigation for Soil Moisture Drought in Southwestern North America. *Earth's Future*, *9*(9), e2021EF002014. https://doi.org/10.1029/2021EF002014

Cooper, M. G., Nolin, A. W., & Safeeq, M. (2016). Testing the recent snow drought as an analog for climate warming sensitivity of Cascades snowpacks. *Environmental Research Letters*, *11*(8), 084009. https://doi.org/10.1088/1748-9326/11/8/084009

Fang, Y., Liu, Y., & Margulis, S. A. (2022). *Western United States UCLA Daily Snow Reanalysis, Version 1*. Boulder, Colorado USA. NASA National Snow and Ice Data Center Distributed Active Archive Center. https://doi.org/10.5067/PP7T2GBI52I2

Harpold, A. A., & Molotch, N. P. (2015). Sensitivity of soil water availability to changing snowmelt timing in the western U.S. *Geophysical Research Letters*, *42*(19), 8011–8020. https://doi.org/10.1002/2015GL065855

Harpold, A. A., Sutcliffe, K., Clayton, J., Goodbody, A., & Vazquez, S. (2017). Does Including Soil Moisture Observations Improve Operational Streamflow Forecasts in Snow-Dominated Watersheds? *JAWRA Journal of the American Water Resources Association*, *53*(1), 179–196. https://doi.org/10.1111/1752-1688.12490

Hatchett, B. J., Rhoades, A. M., & McEvoy, D. J. (2022). Monitoring the daily evolution and extent of snow drought. *Natural Hazards and Earth System Sciences*, *22*(3), 869–890. https://doi.org/10.5194/nhess-22-869-2022

Huning, L. S., & AghaKouchak, A. (2020). Global snow drought hot spots and characteristics. *Proceedings of the National Academy of Sciences*, *117*(33), 19753–19759. https://doi.org/10.1073/pnas.1915921117

Kim, R. S., Kumar, S., Vuyovich, C., Houser, P., Lundquist, J., Mudryk, L., Durand, M., Barros, A., Kim, E. J., Forman, B. A., Gutmann, E. D., Wrzesien, M. L., Garnaud, C., Sandells, M., Marshall, H.-P., Cristea, N., Pflug, J. M., Johnston, J., Cao, Y., … Wang, S. (2021). Snow Ensemble Uncertainty Project (SEUP): Quantification of snow water equivalent

uncertainty across North America via ensemble land surface modeling. *The Cryosphere*, *15*(2), 771–791. https://doi.org/10.5194/tc-15-771-2021

Lapides, D. A., Hahm, W. J., Rempe, D. M., & Dralle, D. N. (2022). *Missing snowmelt runoff following drought explained by root-zone storage deficits*. https://eartharxiv.org/repository/view/3142/

Li, D., Wrzesien, M. L., Durand, M., Adam, J., & Lettenmaier, D. P. (2017). How much runoff originates as snow in the western United States, and how will that change in the future? *Geophysical Research Letters*, *44*(12), 6163–6172. https://doi.org/10.1002/2017GL073551

Livneh, B., & Badger, A. M. (2020). Drought less predictable under declining future snowpack. *Nature Climate Change*, *10*(5), Article 5. https://doi.org/10.1038/s41558-020-0754-8

Margulis, S. A., Cortés, G., Girotto, M., Huning, L. S., Li, D., & Durand, M. (2016). Characterizing the extreme 2015 snowpack deficit in the Sierra Nevada (USA) and the implications for drought recovery. *Geophysical Research Letters*, *43*(12), 6341–6349. https://doi.org/10.1002/2016GL068520

Margulis, S. A., Liu, Y., & Baldo, E. (2019). A Joint Landsat- and MODIS-Based Reanalysis Approach for Midlatitude Montane Seasonal Snow Characterization. *Frontiers in Earth Science*, *7*, 272. https://doi.org/10.3389/feart.2019.00272

Marshall, A. M., Abatzoglou, J. T., Link, T. E., & Tennant, C. J. (2019). Projected Changes in Interannual Variability of Peak Snowpack Amount and Timing in the Western United States. *Geophysical Research Letters*, *46*(15), 8882–8892. https://doi.org/10.1029/2019GL083770

McCrary, R. R., & Mearns, L. O. (2019). Quantifying and Diagnosing Sources of Uncertainty in Midcentury Changes in North American Snowpack from NARCCAP. *Journal of Hydrometeorology*, *20*(11), 2229–2252. https://doi.org/10.1175/JHM-D-18-0248.1

Musselman, K. N., Lehner, F., Ikeda, K., Clark, M. P., Prein, A. F., Liu, C., Barlage, M., & Rasmussen, R. (2018). Projected increases and shifts in rain-on-snow flood risk over western North America. *Nature Climate Change*, *8*(9), Article 9. https://doi.org/10.1038/s41558-018-0236-4

NOAA National Centers for Environmental Information (NCEI). (2022). *NOAA National Centers for Environmental Information (NCEI) U.S. Billion-Dollar Weather and Climate Disasters (2022)* [Data set]. NOAA National Centers for Environmental Information. https://doi.org/10.25921/STKW-7W73

Nolin, A. W., Sproles, E. A., Rupp, D. E., Crumley, R. L., Webb, M. J., Palomaki, R. T., & Mar, E. (2021). New snow metrics for a warming world. *Hydrological Processes*, *35*(6). https://doi.org/10.1002/hyp.14262

Seyfried, M. S., Grant, L. E., Marks, D., Winstral, A., & McNamara, J. (2009). Simulated soil water storage effects on streamflow generation in a mountainous snowmelt environment, Idaho, USA. *Hydrological Processes*, *23*(6), 858–873. https://doi.org/10.1002/hyp.7211

Siirila-Woodburn, E. R., Rhoades, A. M., Hatchett, B. J., Huning, L. S., Szinai, J., Tague, C., Nico, P. S., Feldman, D. R., Jones, A. D., Collins, W. D., & Kaatz, L. (2021). A low-to-no snow future and its impacts on water resources in the western United States. *Nature Reviews Earth & Environment*, *2*(11), Article 11. https://doi.org/10.1038/s43017-021-00219-y

Stewart, I. T., Cayan, D. R., & Dettinger, M. D. (2004). Changes in Snowmelt Runoff Timing in Western North America under a `Business as Usual' Climate Change Scenario. *Climatic Change*, *62*(1), 217–232. https://doi.org/10.1023/B:CLIM.0000013702.22656.e8

Viviroli, D., Archer, D. R., Buytaert, W., Fowler, H. J., Greenwood, G. B., Hamlet, A. F., Huang, Y., Koboltschnig, G., Litaor, M. I., López-Moreno, J. I., Lorentz, S., Schädler, B., Schreier, H., Schwaiger, K., Vuille, M., & Woods, R. (2011). Climate change and mountain water resources: Overview and recommendations for research, management and policy. *Hydrology and Earth System Sciences*, *15*(2), 471–504. https://doi.org/10.5194/hess-15-471-2011

Western Water Assessment. (2021). *Water Year 2021 Summary*. https://wwa.colorado.edu/resources/intermountain-west-climate-dashboard/briefing/water-year-2021-summary

Williams, A. P., Cook, B. I., & Smerdon, J. E. (2022). Rapid intensification of the emerging southwestern North American megadrought in 2020–2021. *Nature Climate Change*, *12*(3), Article 3. https://doi.org/10.1038/s41558-022-01290-z

Williams, A. P., Cook, E. R., Smerdon, J. E., Cook, B. I., Abatzoglou, J. T., Bolles, K., Baek, S. H., Badger, A. M., & Livneh, B. (2020). Large contribution from anthropogenic warming to an emerging North American megadrought. *Science*, *368*(6488), 314–318. https://doi.org/10.1126/science.aaz9600

Zheng, X., Wang, Q., Zhou, L., Sun, Q., & Li, Q. (2018). Predictive Contributions of Snowmelt and Rainfall to Streamflow Variations in the Western United States. *Advances in Meteorology*, *2018*, e3765098. https://doi.org/10.1155/2018/3765098

CHAPTER 4

Spatiotemporal snow water storage uncertainty in the midlatitude American Cordillera

Despite the critical role of snow in terrestrial water resources, spatiotemporal snow water storage uncertainty remains unclear over the midlatitude American Cordillera. This work quantifies the uncertainty of accumulation-season peak snow storage amongst commonly used global and regional products over the Western U.S. (WUS) and Andes, which have similar hydrometeorology but are disparate with respect to amount of available in situ information. The recently developed WUS Snow Reanalysis (WUS-SR) and Andes Snow Reanalysis (Andes-SR) datasets, that have been significantly verified against in situ measurements over 30 years, are used as reference datasets. Intercomparison results over WUS show that climatological peak SWE storage averaged from high- and moderate-resolution products (284 ± 14 km^3; overestimated by 6%) is in better agreement with WUS-SR (269 km^3) than the low-resolution products (127 ± 54 km^3; underestimated by 53%). Compared to the Andes-wide peak snow storage estimate from Andes-SR (29 km^3), the averaged estimates from other products (19 km^3 ± 16 km^3; underestimated by 35%) are less clustered by spatial resolution, have large uncertainty, and are mostly biased low. Only the high- to moderate-resolution SNODAS and UA products show comparable estimates of windward-leeward gradients with the reference dataset over a subdomain (Sierra Nevada) of the WUS. The other products distribute too much snow on the leeward side in both the Sierra Nevada and Andes, missing the orographic-rainshadow patterns that have important hydrological implications. The uncertainty of peak seasonal snow storage is

primarily explained by precipitation uncertainty in both the WUS (R^2 = 0.55) and Andes (R^2 = 0.84). Given similar forcing inputs, snow storage can be significantly divergent in the ERA5 and GLDAS subsets due to resolution-induced elevation differences or distinct land surface model mechanisms including rain–snow partitioning and accumulation-season snowmelt generation. The availability and use of in situ precipitation and snow measurements (i.e., in WUS) in some products adds value by reducing snow storage uncertainty, however they are not applicable for regions with limited in situ data like the Andes.

4.1 Background and Motivation

Seasonal snow storage in mountains provide vital freshwater to downstream users estimated to be over 16.7% of the global population (Immerzeel et al., 2020; Rhoades et al., 2022). Melt of accumulated winter snow in the spring and summer impacts agriculture, hydropower generation, and water supply and recreation, making it a key component of the food-energy-water nexus in many regions of the world (Huss et al., 2017; Qin et al., 2020; Siirila-Woodburn et al., 2021). Despite its importance, a complete understanding of regional terrestrial water cycles is hampered by a limited characterization of seasonal mountain snow storage uncertainty.

The lack of in situ and remotely sensed measurements of mountain snow water equivalent (SWE), a key metric related to water availability, are primarily responsible for the limited characterization of seasonal snow storage in these regions. For example, in the midlatitude American Cordillera, where snowmelt is estimated to contribute to as much as 70% of total runoff in some basins (Li et al., 2017), existing in situ networks are both sparse and unrepresentative of the conditions spanning the larger domains in the Western United States (WUS) and South American Andes (Dozier et al., 2016; Molotch & Bales, 2006; Nolin et al.,

2021; Saavedra et al., 2018). Current remotely sensed SWE estimates from passive microwave measurements are useful over much of the globe, but are too coarse to capture the spatial heterogeneity and deep snowpacks in these regions with complex terrain (Luojus et al., 2021).

In lieu of measurements, globally available snow products, typically generated from land surface models (LSMs), provide the majority of large-scale estimates of the spatiotemporal patterns of mountain snow water storage. However, seasonal snow storage estimates from global snow products remain highly uncertain, which results from discrepancies in meteorological forcings, variations in snow process representation, and coarse spatial resolution (Broxton et al., 2016; Cho et al., 2022; Liu et al., 2022; Wrzesien et al., 2019). The uncertainty (including bias) of seasonal snow storage further propagates to streamflow forecasts (Kim et al., 2021) and impacts water resources management. Coarse spatial resolutions smooth topography and impact the ability to resolve orographic features (including rainshadows) over complex terrain (Daly, 2006). Current estimates of mountain snow water storage uncertainties in both space and time need to be characterized to ensure the reliability of impact studies that rely on SWE estimates (Mankin et al., 2015; Immerzeel et al., 2020; Huning and AghaKouchak, 2020).

The analysis herein is applied to the snow-dominated midlatitude portions of the American Cordillera, which are representative of regional mountains of significant importance to humans. To quantify the spatiotemporal uncertainties of snow storage from commonly used snow products, recently-developed high-resolution snow reanalysis datasets covering the WUS (Fang et al., 2022) and Andes (Cortés & Margulis, 2017) are used in this work as reference datasets. The WUS and Andes domains have comparable atmospheric circulation patterns and hydrologic cycles (Rhoades et al., 2022), but are disparate with respect to the amount of available in situ information. The WUS has among the highest density of in situ snow

information, which either directly or indirectly inform SWE estimates, while the Andes has little to no ground measurements, making SWE estimates almost entirely model-based. This paper aims to assess: 1) the spatiotemporal uncertainty of SWE in the WUS and Andes over the accumulation season, and 2) the drivers of the SWE uncertainty. Knowledge of the uncertainty and its drivers will put current snow-impact studies in better context and provide a pathway for improving future estimates aimed at reducing snow uncertainty.

4.2 Study Domain and Datasets

4.2.1 Study Domain

This study focuses on the snow-dominated midlatitude mountain ranges of the America Cordillera (Figure 1), where snowmelt-driven runoff serves large populations. Specifically, the WUS and Andes are selected as the study domains based on recently developed snow-specific reanalysis products (Cortés & Margulis, 2017; Fang et al., 2022). These SWE estimates have been significantly verified against independent in situ and airborne measurements, making them well-suited to being used as references for other products. The average elevation across the WUS is ~ 1383 m with a maximum > 4300 m, in contrast to a higher average elevation of ~ 2999 m with a maximum > 6800 m in the Andes. The beginning of the seasonal snow cycle starts from October 1st and April 1st in the WUS and Andes, respectively. Hence, a water year (WY) spans from October 1st to September 30th in the WUS, and April 1st to March 31st in the Andes.

The WUS contains three major mountain ranges including the Sierra Nevada, Rocky Mountains and Cascades (Fig. 4.1). Amongst these, the Sierra Nevada subdomain is the closest analog to the Andes, sharing similar hydroclimatology and topography. Winter westerlies dominate precipitation timing and patterns in these two mountain ranges, leading to orographic gradients on the windward side of the mountains and rainshadow effects resulting in significant

snow differences across relatively short windward-leeward gradients.

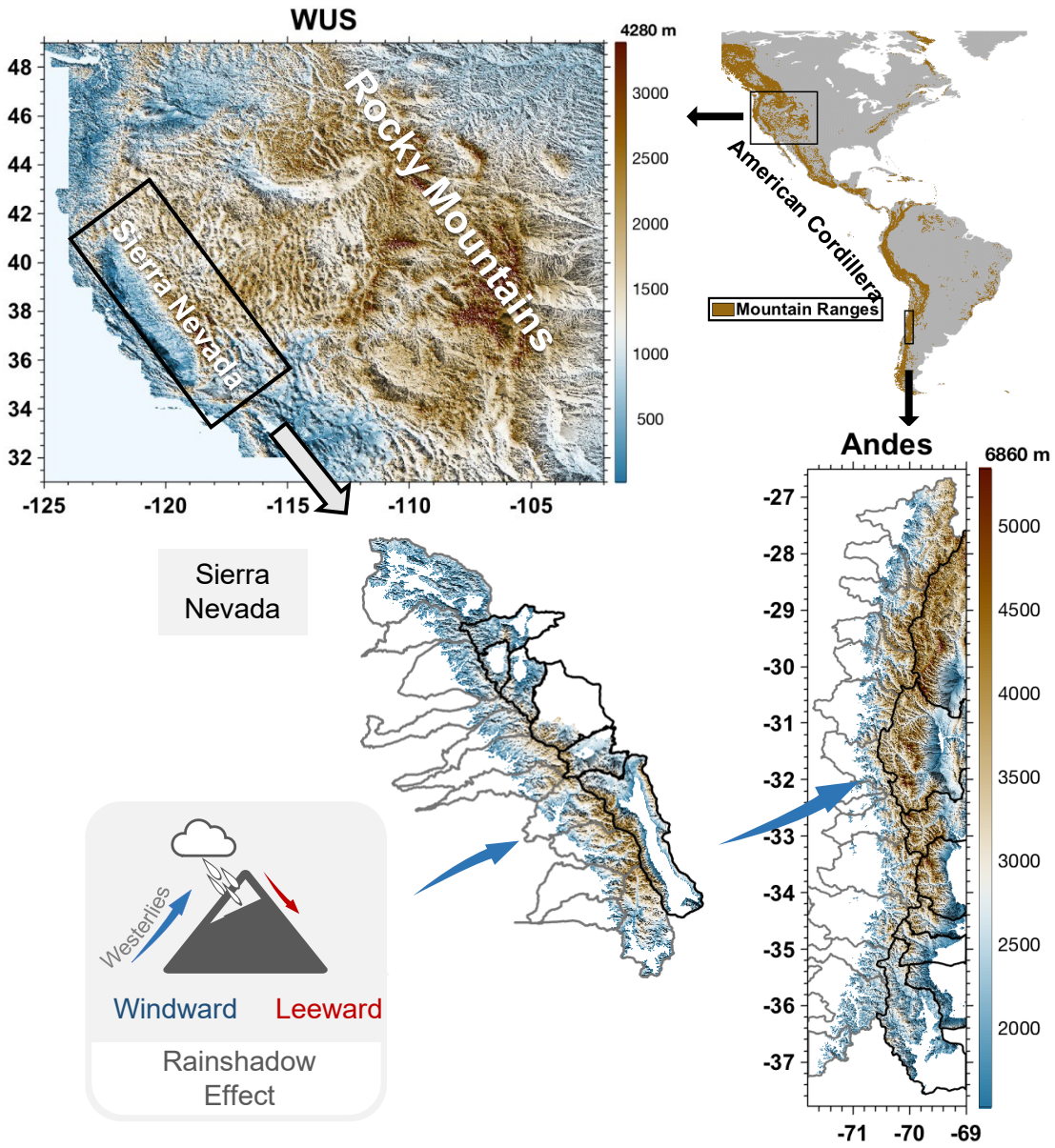

Figure 4.1 DEM and location of midlatitude American Cordillera: WUS and Andes. Bottom left cartoon shows that moist air rises on the windward side of the mountain, and drier air flows down the leeward side of the mountain creating a rainshadow effect. Arrows represent the generalized directions of westerlies. The Sierra Nevada (SN, sub-basin of WUS) and Andes are chosen to study the rainshadow effect. Windward watersheds are shown in gray boundaries and leeward watersheds are shown in black boundaries. Mountain ranges are based on Snethlage et al. (2022).

4.2.2 Datasets

This paper intercompares data from the Andes Snow Reanalysis (Andes-SR) and WUS Snow Reanalysis (WUS-SR) datasets (as reference datasets), to seven global snow datasets (available over both domains), and two regional datasets (available only over the WUS domain) shown in Table 4.1. The Andes-SR (WYs 1985 to 2015; Cortés and Margulis, 2017) SWE estimates are at ~ 180 m resolution and the WUS-SR (WYs 1985 to 2021; Fang et al., 2022) SWE estimates are at ~ 480 m resolution. The Andes-SR and WUS-SR datasets were both generated from the Bayesian framework developed by Margulis et al. (2016, 2019) with assimilation of fractional snow-covered area images derived from Landsat 5, 7 and 8 using the Particle Batch Smoother (PBS; Margulis et al., 2015). Independent verification shows that both datasets are consistent with in situ peak SWE with a correlation coefficient of 0.73 over the Andes (Cortés & Margulis, 2017) and 0.77 over the WUS (using > 25,000 station-years of in situ data; Fang et al., 2022). Further verification of the WUS-SR SWE against Airborne Snow Observatory (ASO) SWE estimates shows consistent performance between these two spatial products with correlation coefficients ranging from 0.75 to 0.91. With high consistency against point-scale in situ and spatially-distributed airborne SWE estimates, as well as the high spatial resolutions specifically targeting mountainous domains, these two snow reanalysis datasets are used as reference SWE datasets to evaluate the snow storage of other products over the WUS and Andes.

The seven global snow products include ERA5-Land, ERA5, MERRA2 and four GLDAS-2.1 products (Noah LSM at 0.25°: GLDAS – NOAH025; Noah LSM at 1.0°: GLDAS – NOAH10; VIC LSM at 1.0°: GLDAS –VIC10; Catchment LSM at 1.0°: GLDAS – CLSM10). The SNODAS and UA products only cover the US and therefore are not included in Andes

intercomparison. Following Liu et al. (2022), SWE, precipitation and snowfall were collected from each of the seven global products, SNODAS, and UA (including PRISM precipitation (Daly et al., 1994) used in the UA product). Since the reference snow reanalysis products do not output precipitation and snowfall, only SWE is used for reference. For the purposes of analysis and discussion in this work, the products described above are classified by their spatial resolution. Specifically, reference datasets and those products with spatial resolution less than ~1 km are deemed "high-resolution" (*HR*: WUS-SR, Andes-SR, and SNODAS), those with spatial resolutions between ~1 km and ~10 km are deemed "moderate-resolution" (*MR*: UA, ERA5-Land), and those with spatial resolutions greater than ~10 km are deemed "low-resolution" ("*LR*": ERA5, GLDAS set). Globally and regionally availably datasets are referred to as "products", and WUS-SR and Andes-SR are referred to as reference "datasets".

The snow reanalysis reference products are, by design, constrained by observations using a data assimilation approach. However, not all the other products are solely model-based. SNODAS uses in situ snow, airborne SWE from gamma radiation snow surveys and satellite snow cover, and UA uses in situ SWE as inputs to constrain estimates. Although ERA5 assimilates snow depth, limited examples of these in situ measurements are used in the WUS and Andes. However, in the WUS, with its relatively high density of in situ meteorological sites, almost all products are based on models with meteorological forcings that include some in situ measurements. In contrast, due to limited in situ meteorological sites in the Andes, the quality of input forcings remains unclear, but is likely more uncertain than over the WUS. More details on the snow products used herein are given in Table 4.1 and Appendix B.1.

Table 4.1 Details of snow datasets and products used in this work. Note that SNODAS data in WY 2004 is not used due to quality issues cited in NOHRSC (2004). *Snow reanalysis products are used as reference datasets.

Datasets/Products	Land surface model	Spatial Resolution	Temporal Coverage	Forcings	Assimilated snow data (Method)	Domain availability
WUS-SR*	SSiB - SDC	16” (~500 m)	1985-2021	MERRA2	Landsat fSCA (PBS)	WUS
ANDES-SR*	SSiB - SDC	6” (~180 m)	1985-2015	MERRA	Landsat fSCA (PBS)	Andes
SNODAS	NOHRSC Snow Model (NSM)	1 km (~ 0.01°)	2004-present	Downscaled NWP forcing	Ground based snow/ airborne SWE/ satellite snow cover (Newtonian Nudging)	WUS
UA	-	4 km (~ 0.04°)	1981-present	PRISM	In situ SWE/ snow depth from SNOTEL and snow depth from COOP (Ordinary Kriging Interpolation)	WUS
ERA5-Land	H-TESSEL (IFS Cy45r1)	0.1° (~ 10 km)	1950-present	ERA5 with “lapse rate correction”	-	WUS, Andes
ERA5	H-TESSEL (IFS Cy41r2)	0.25° (~ 25 km)		IFS Cy41r2 with 4D-Var	In situ snow depth (Optimal Interpolation); IMS snow cover	WUS, Andes
MERRA2	Catchment	0.5° × 0.625° (~ 50 - 63 km)	1980-present	MERRA2	-	WUS, Andes
GLDAS-2.1	Noah	0.25° (~ 25 km)	2001-present	NOAA/GDAS, GPCP 1.3, bias corrected AGRMET	-	WUS, Andes
	Noah	1° (~ 100 km)			-	WUS, Andes
	VIC	1° (~ 100 km)			-	WUS, Andes
	Catchment (CLSM)	1° (~ 100 km)			-	WUS, Andes

4.3 Intercomparison Methodology

4.3.1 Intercomparison study period

Where possible, the intercomparison study periods in the two domains are chosen as WYs 1985-2021 (01 October 1984 to 30 September 2021) for the WUS, and WYs 1985-2015 (01 April 1984 to 31 March 2015) for the Andes, based on the availability of the respective snow reanalysis datasets. Of the products listed in Table 4.1, only GLDAS (starting in WY 2001) and SNODAS (starting in WY 2005) are not available over the full snow reanalysis period. For those products, long-term climatologies are necessarily derived over the shorter periods. Hence in the WUS, climatologies for the GLDAS and SNODAS products are over their available 21- and 17-year records, while all other products span the 37-year record. In the Andes, the GLDAS products are over their 15-year record, while all other products span the 31-year record. Analysis of climatological results from the products with longer periods do not show significant differences when applied to the shorter study periods (not shown).

4.3.2 Focusing on intercomparison during the snow accumulation season

The intercomparison herein focuses on the snow accumulation season. To motivate this focus, the climatological (long-term average) daily time series of domain-aggregated SWE volume across all products are illustrated in Fig. 4.2 Two key points are evident: (i) there are significant discrepancies between products (that are analyzed in more detail below) and (ii) much of the uncertainty occurs during the accumulation season (and then propagates to the ablation season). An accurate characterization of peak SWE (at the end of the accumulation season) is a key metric of the final condition of snow accumulation processes and the initial condition leading into the main snowmelt season. Intercomparison of modeled snowmelt season processes are made more difficult when the initial conditions (i.e., peak SWE prior to the primary ablation

season) across models are different. Given the large uncertainties observed in domain-wide peak SWE climatology (Fig. 4.2), this paper focuses on the uncertainties in the accumulation season (as done in Liu et al., 2022) in order to better understand how and why accumulation season estimates diverge across products. All the analyses focus on the accumulation season using metrics described below.

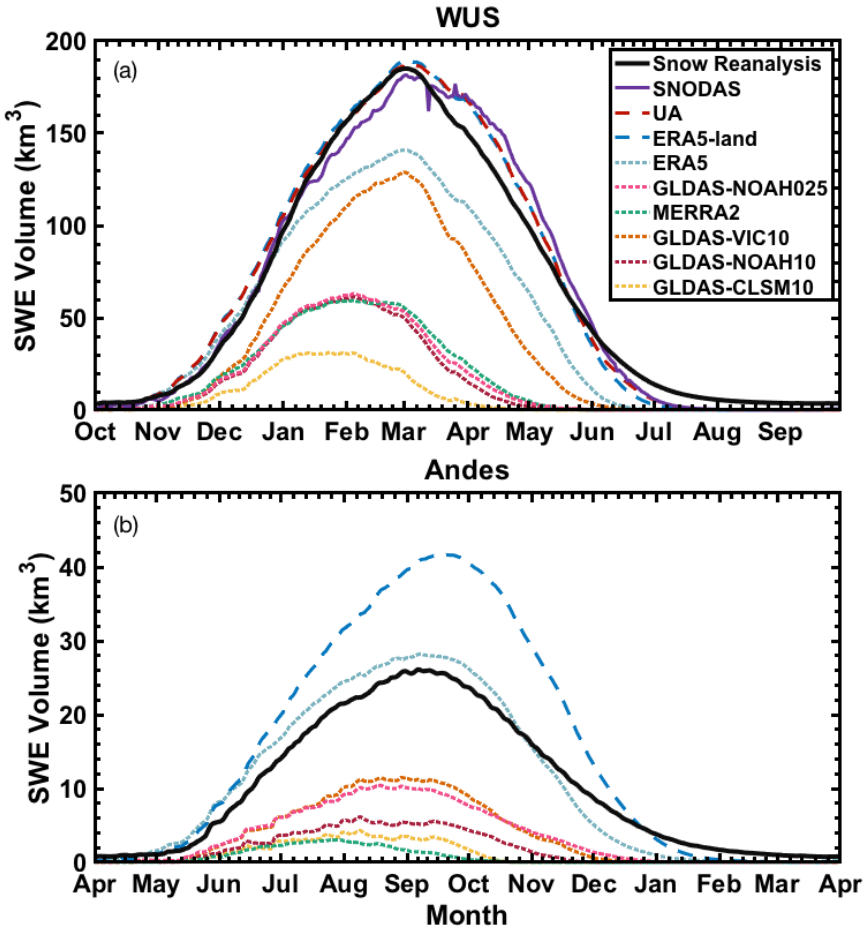

Figure 4.2 Climatology of seasonal cycle of SWE volume in the WUS and Andes domains. Solid lines represent high-resolution (HR) datasets and products, dashed lines represent moderate-resolution (MR) products, and dotted lines represent low-resolution (LR) products.

4.3.3 Snow metrics used in the intercomparison

The processes leading to the domain-aggregated peak SWE shown in Fig. 4.2 depend on pixel-scale snow mass balance processes. Hereafter, for each product, the pixel-wise processes

are analyzed prior to aggregating to the larger domain. The day corresponding to pixel-wise peak SWE (defined as t_{peak}) is computed for each product at their raw spatial resolution. The pixel-wise peak SWE depth (swe_{peak}) is aggregated to get pixel-wise peak SWE volume (SWE_{peak}). Hence in results to follow, swe_{peak} is used to describe and analyze maps of SWE, while SWE_{peak} is used to describe spatially aggregated volumes of SWE.

At each pixel, accumulation-season precipitation and snowfall are accumulated from the beginning of the WY up to t_{peak}, where the accumulated maps of depth can then be aggregated over the domain of interest. The mass balance equations relating domain-aggregated cumulative snowfall (S_{acc}), SWE (SWE_{peak}), cumulative ablation (A_{acc}), cumulative precipitation (P_{acc}), cumulative snowfall (S_{acc}), and cumulative rainfall (R_{acc}) are shown below:

$$SWE_{peak} = S_{acc} - A_{acc} \tag{7}$$

$$S_{acc} = P_{acc} - R_{acc} \tag{8}$$

where in Eq. (1) and (2), P_{acc}, S_{acc}, SWE_{peak} are directly computed from the snow products. R_{acc} and A_{acc} are the residuals based on these two mass balance equations. Climatological values are computed as the long-term (interannual) mean of P_{acc}, S_{acc}, SWE_{peak} over the intercomparison periods.

Persistent snow and ice areas are excluded before spatially integrating the SWE volumes, since most products analyzed in this work do not explicitly estimate glaciers and persistent snow. Such persistent snow and ice masks are first obtained from the Andes-SR and WUS-SR products and then aggregated to the spatial resolution of each product (as done in Liu et al., 2022). Domain masks in each product are also applied here, which are derived based on the reference

datasets using the same approach. Details of persistent snow and ice masks and domain masks are described in Appendix B.2 and shown in Fig. B.1 and B.2.

Beyond domain-wide results, we choose to intercompare products and their ability to capture rainshadow effects, that often occur over short geographic scales, but have significant influence on the water availability between windward and leeward sides of mountain ranges. For simplicity we focus on the windward-leeward contrasts over the Sierra Nevada in the WUS and those over the Andes. Figure 4.1 shows the boundaries of windward basins (in gray) and leeward basins (in black) for both domains. The Sierra Nevada and Andes are analogs of each other due to the mostly north-south orientation of the mountain ranges that are relatively perpendicular to the mostly westerly prevailing winds. In both cases, the windward and leeward basins serve distinct downstream populations and so resolving those spatial variations have important hydrological implications. To assess the ability of products in capturing rainshadow effects, pixel-wise SWE_{peak} is aggregated over the windward (SWE_{peak}^{wind}) and leeward (SWE_{peak}^{lee}) watersheds. Since MR and CR pixels may cover both windward and leeward watersheds, fractional swe_{peak} is aggregated to get SWE_{peak} over the two types of watersheds separately (Fig. B.3 and B.4). The fractional swe_{peak} is computed by multiplying pixel-wise swe_{peak} and the fraction of pixel within the windward or leeward watershed. The detailed steps used to derive the windward and leeward watershed snow storage are described in Appendix B.2.

4.4 Results and Discussion

4.4.1 Climatological SWE uncertainty

4.4.1.1 Spatial distribution of pixel-wise peak SWE

Climatological pixel-wise swe_{peak} maps for the WUS-SR (Fig. 4.3a) clearly show the highest snow storage occurring in the Sierra Nevada, Cascades, and Rocky Mountains. When

integrated over the whole domain, the climatological WUS SWE_{peak} is 269.2 km^3 (Fig. 4.3k). Similar spatial distributions of swe_{peak} are observed for the HR (SNODAS; Fig. 4.3b) and MR products (UA and ERA5-Land; Fig. 4.3c and d). However, the remaining products (ERA5, MERRA5 and GLDAS set; Fig. 4.3e to j) significantly underestimate swe_{peak} and smooth out the spatial patterns captured by the HR and MR products. The combined HR and MR inter-product average of climatological WUS SWE_{peak} is 283.8 ± 14.4 km^3, in contrast to an average of 126.7 ± 53.7 km^3 for LR products (Fig. 4.3k). This suggests large uncertainty (both bias and spread) in SWE_{peak} among LR products. Compared to WUS-SR, SNODAS overestimates SWE_{peak} by ~12% (Fig. 4.3k) and exhibits higher swe_{peak} in the Sierra Nevada, Cascades, and Rocky Mountains. UA and ERA5-Land both exhibit a similar magnitude of SWE_{peak} (differences < 5%) compared to WUS-SR, both of which have higher swe_{peak} in the Cascades. Despite similar spatial distribution of swe_{peak}, ERA5-Land and ERA5 underestimate WUS SWE_{peak} by 21% (Fig. 4.3k) compared to WUS-SR. All GLDAS products severely underestimate SWE_{peak} compared to WUS-SR, where GLDAS-VIC10 shows the highest WUS SWE_{peak} (with a 35% underestimation compared to WUS-SR).

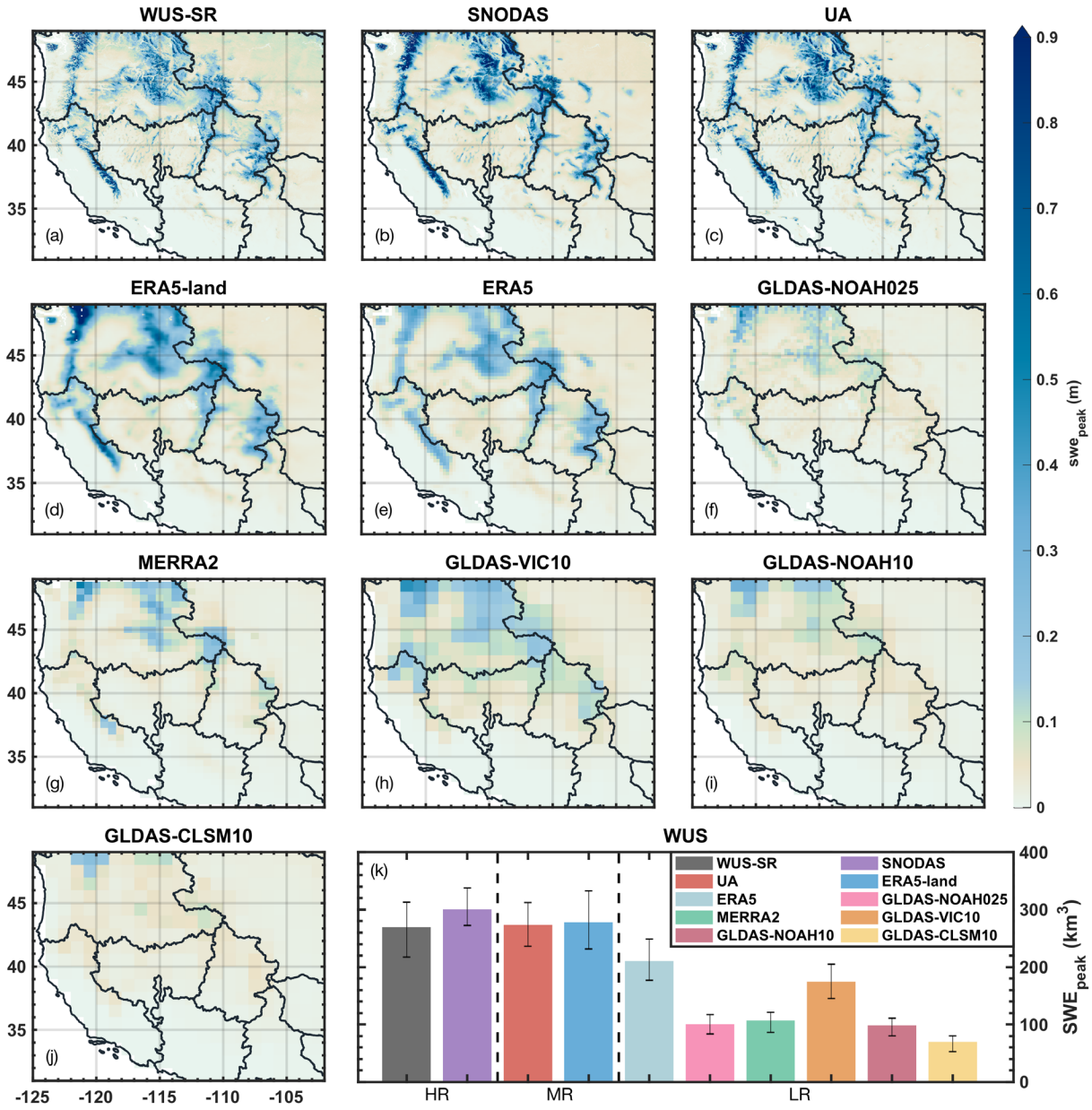

Figure 4.3 (a – j) Spatial distribution of climatological swe_{peak} in the WUS. (k) shows the climatological WUS SWE_{peak} (colored bars) and the interannual inter-quartile range (IQR; black error bars). The bar plots are ordered by spatial resolution, with highest resolution on the left and lowest resolution on the right. The vertical dashed lines separate the three spatial resolution categories (i.e., HR < ~ 1 km, ~ 1 km < MR < ~ 10 km, LR > ~ 10 km). Glacier and permanent snow areas are masked out in the maps and domain aggregated volumes.

Based on the Andes-SR, the climatological SWE_{peak} is 28.9 km^3 (Fig. 4.4i). The southern Andes has higher swe_{peak} compared to the northern region (Fig. 4.4a). The spatial distribution of swe_{peak} and integrated SWE_{peak} volumes vary much more broadly across different products (Fig. 4.4b to k) than they do in the WUS. The MR and LR inter-product average of climatological SWE_{peak} is 19.2 ± 15.6 km^3 (Fig. 4.4i). ERA5-Land and ERA5 overestimate SWE_{peak} by 65.6% and 17.6%, respectively (Fig. 4.4i). ERA5-Land significantly overestimates swe_{peak} in the southern part of the Andes. Most of the LR products, including MERRA2 and the GLDAS set, significantly underestimate SWE_{peak} by as much as 79%, compared to Andes-SR (Fig. 4.4i). These findings for the Andes domain are qualitatively similar to Liu et al. (2022), where ERA5 and ERA5-Land overestimate SWE_{peak} and MERRA2 and GLDAS underestimate SWE_{peak} in High Mountain Asia (HMA), another snow-dominated region with limited in situ measurements.

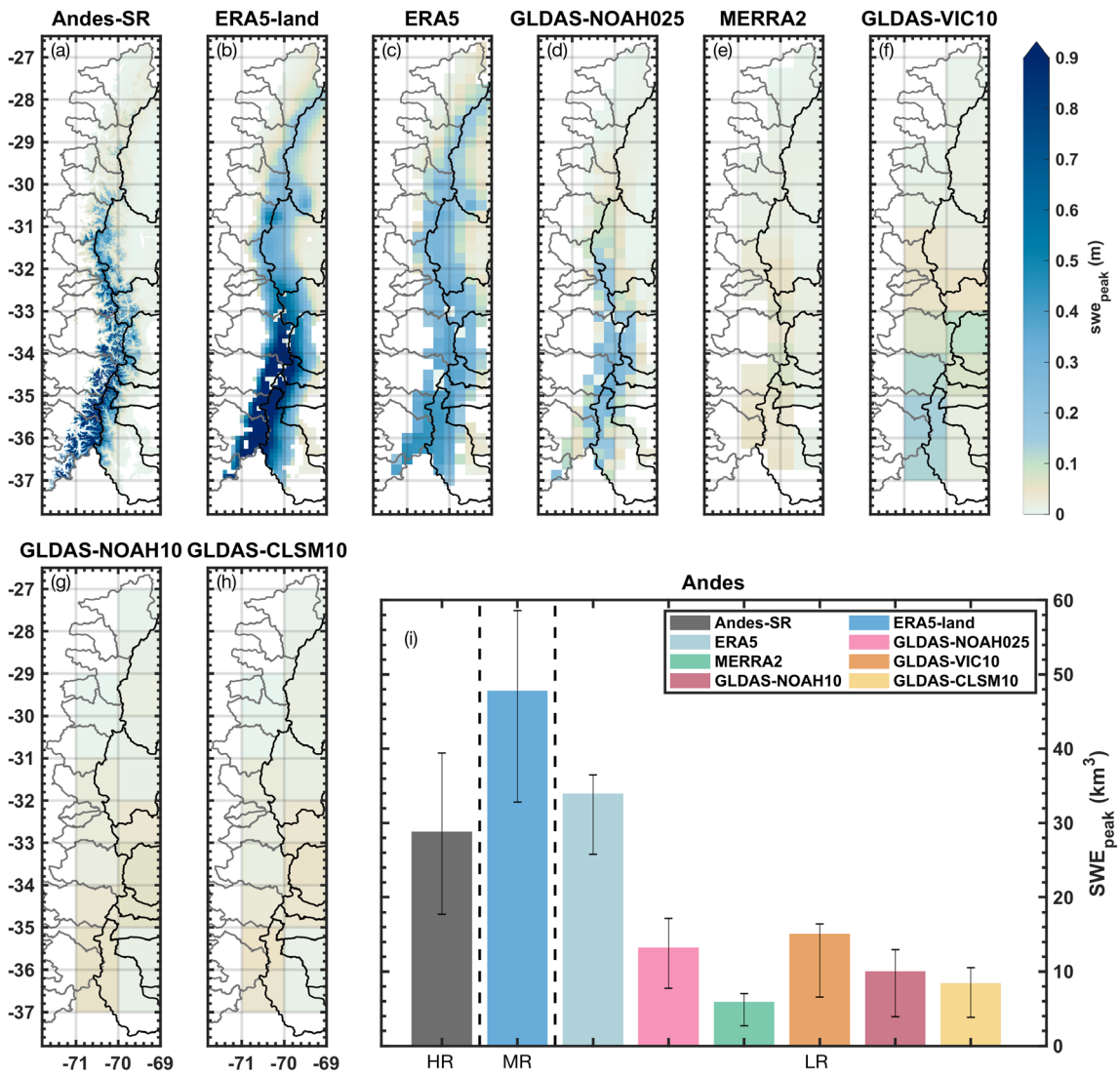

Figure 4.4 (a – h) Spatial distribution of climatological swe_{peak} in the Andes. (i) shows the climatological Andes SWE_{peak} (colored bars) and the interannual inter-quartile range (IQR; black error bars). The bar plots are ordered by spatial resolution, with highest resolution on the left and lowest resolution on the right. The vertical dashed lines separate the three spatial resolution categories (i.e., HR < ~ 1 km, ~ 1 km < MR < ~ 10 km, LR > ~ 10 km). Glacier and permanent snow areas are masked out in the maps and domain aggregated volumes.

4.4.1.2 Resolving key spatial gradients: Rainshadow effects

In addition to the overall spatial distribution in SWE, the orographically-driven rainshadow (windward vs. leeward) distribution represents an example of an important spatial

feature in many mountain contexts. Beyond climatological biases described in Section 4.4.1.1, this section focuses on the relative patterns of windward vs. leeward storage. The differences in rainshadow storage gradients are examined in the Sierra Nevada subdomain of the WUS and across the Andes. While resolving rainshadow effects is challenging for narrow topographic regions like the Sierra Nevada and Andes, it has important hydrological implications.

Based on the WUS-SR in the Sierra Nevada (Fig. 4.5), the latitudinal distribution of SWE_{peak}^{wind} is largest in the 37°–38° N latitudinal band, while the latitudinal distribution of SWE_{peak}^{lee} is largest in the 38°–39° N latitudinal band. The latitudinal windward and leeward basin storage of SWE decreases monotonically north and south of these maximum values. The total stored windward volume SWE_{peak}^{wind} is 3.74 times more than the leeward volume SWE_{peak}^{lee}. This ratio is the combined effect of variations in area and SWE depth between the windward and leeward basins and identifies that (on average) the windward basins store between 3 and 4 times more SWE volume than the leeward basins. Given that the windward and leeward areas across which SWE is integrated are effectively the same across products, any differences in ratio is driven by differences in SWE depth. SWE depth variations are primarily driven by resolving orographic enhancement of snowfall between windward and leeward slopes. In the Sierra Nevada, only SNODAS and UA products (spatial resolutions < ~ 4 km) exhibit comparable SWE_{peak}^{wind} to SWE_{peak}^{lee} ratios. The ratios of SWE_{peak}^{wind} to SWE_{peak}^{lee} are 4.20 (12% greater than the WUS-SR) for SNODAS and 3.14 (16% less than WUS-SR) for UA, suggesting a fairly good agreement between windward-leeward snow volume distributions in these products. However, resolving the pattern of windward-leeward snow distribution is significantly impaired in the other MR and LR products. The ratios computed from ERA5-Land, ERA5, GLDAS-NOAH025, MERRA2, GLDAS-VIC10, GLDAS-NOAH10, and GLDAS-CLSM10 range from 1.08-2.40

and are 36%, 46%, 43%, 55%, 68%, 66%, and 71% less than that in the WUS-SR, respectively. Hence, the MR and LR products generally have too little snow on the windward side compared to the leeward side. The location of the windward maximum SWE_{peak} is consistent in most snow products with the exception of the LR products (i.e., ERA5, GLDAS), which have a secondary maximum between 39°–40° N. The location of the leeward maximum SWE_{peak} is consistent in most of the snow products with the exception of MERRA2, which is maximum at a lower latitude.

Based on the Andes-SR, the largest SWE_{peak}^{wind} is distributed between the 35°–36° S latitudinal band, while the distribution of SWE_{peak}^{lee} has two peaks between the 31°–32° S and 35°– 36° S latitudinal bands (Fig. 4.6). The ratio of SWE_{peak}^{wind} to SWE_{peak}^{lee} is 1.58 from the Andes-SR, which is again the combined effect of windward-leeward variations in both area and SWE depth. Like the Sierra Nevada, ERA5-Land and all of the CR products improperly partition SWE_{peak} over the windward vs. leeward basins in the Andes. These products have SWE_{peak}^{wind} to SWE_{peak}^{lee} ratios less than 1 indicating deficient snow in the windward watersheds compared to the leeward watersheds. The lowest SWE_{peak}^{wind} to SWE_{peak}^{lee} ratio of 0.72 is observed from MERRA2 (54% less than Andes-SR). GLDAS-VIC10 has the largest SWE_{peak}^{wind} to SWE_{peak}^{lee} ratio of 0.92 among Andes global products, which is still 42% less than the Andes-SR. For the windward watersheds, SWE_{peak}^{wind} from ERA5-Land and GLDAS-CLSM10 are the highest in the same latitudinal band as the Andes-SR, however, the other products have an erroneous SWE_{peak}^{wind} distribution. None of the products resolve the SWE_{peak}^{lee} distribution on the leeward side.

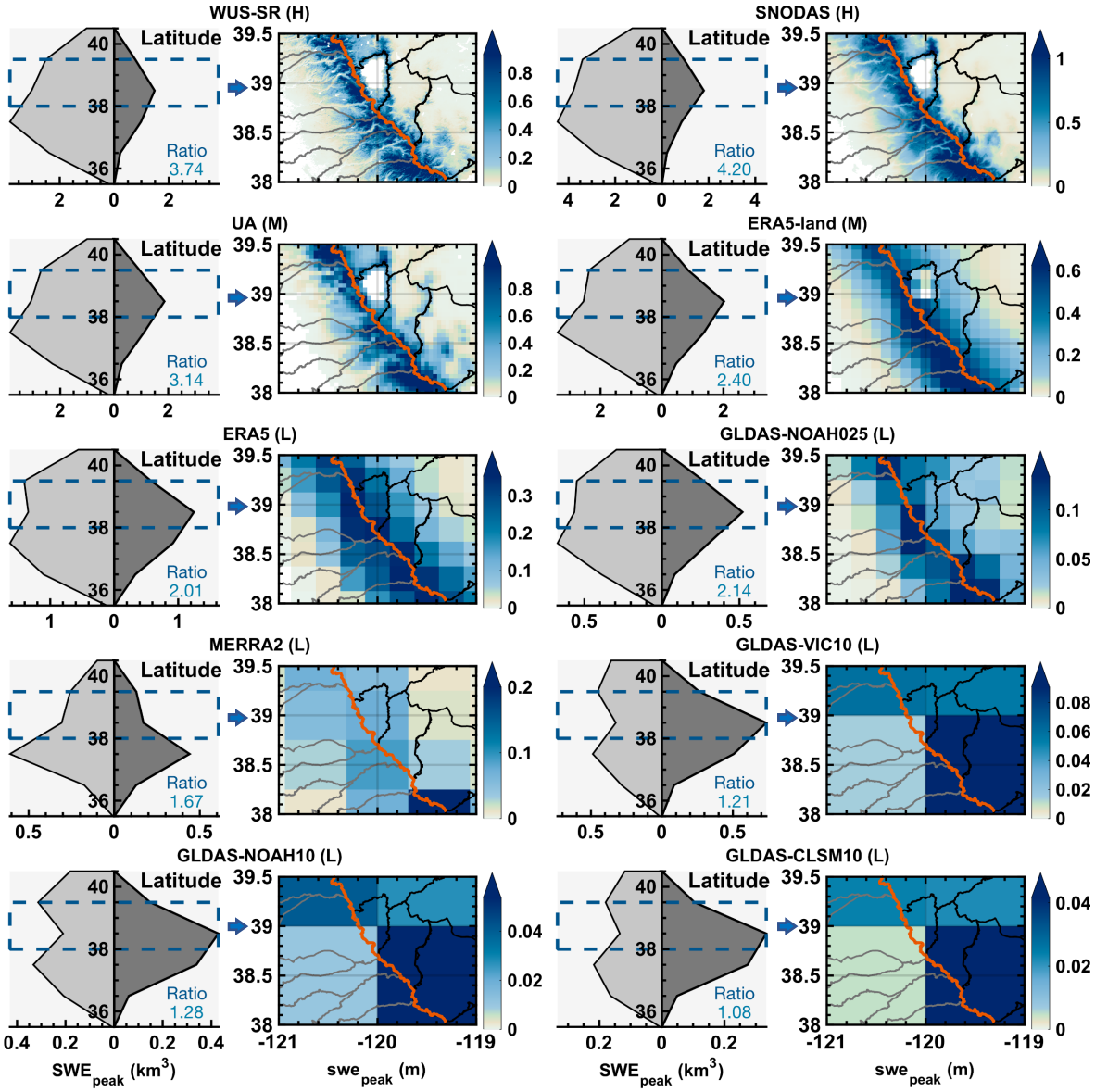

Figure 4.5 Latitudinal distribution of integrated SWE_{peak} (km^3) over windward (SWE_{peak}^{wind}; light gray area) and leeward basins (SWE_{peak}^{lee}; dark gray areas) in the Sierra Nevada in first and third columms. Text labels indicate the ratio of latitudinally-integrated SWE_{peak}^{wind} to SWE_{peak}^{lee}. The climatological swe_{peak} (m) spatial patterns corresponding to the latitude band indicated by dashed lines are illustrated in the second and fourth columns. The red line represents the Sierra Nevada ridgeline separating windward (western) from leeward (eastern) basins. Note: Different swe_{peak} ranges are used for each product to highlight latitudinal/spatial patterns more than absolute values (due to significant biases in some products).

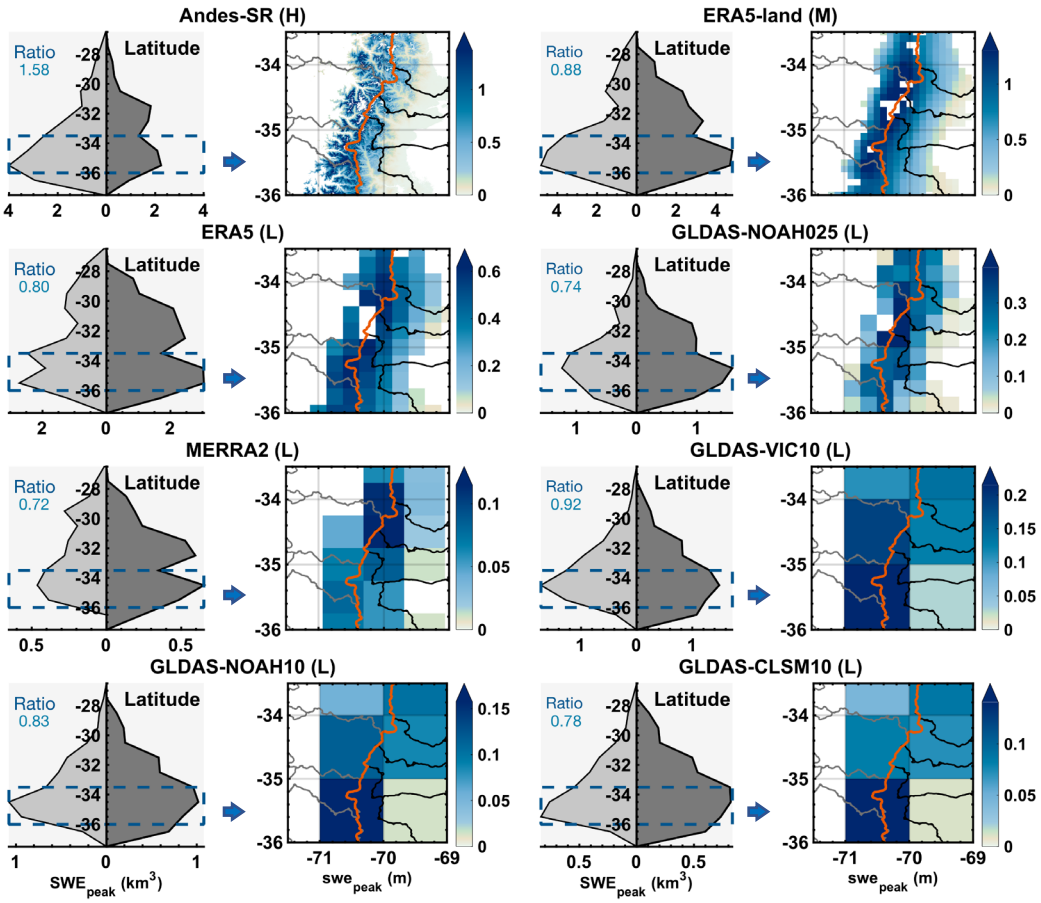

Figure 4.6 Latitudinal distribution of SWE_{peak} (km^3) over windward (SWE_{peak}^{wind}; light gray area) and leeward basins (SWE_{peak}^{lee}; dark gray areas) in the Andes in first and third columms. Text labels indicate the ratios of latitudinally-integrated SWE_{peak}^{wind} to SWE_{peak}^{lee}. The climatological swe_{peak} (m) spatial patterns corresponding to the latitude band indicated by dashed lines are illustrated in the second and fourth columns. The red line represents the Andes ridgeline separating windward (western) from leeward (eastern) basins. Note: Different swe_{peak} ranges are used for each product to highlight latitudinal/spatial patterns.

4.4.2 Interannual SWE uncertainty

The interannual variability of SWE_{peak} is in general agreement (with correlation coefficients $R > 0.86$) between the WUS-SR snow reanalysis and other products shown in Fig. 4.7. SWE_{peak} from UA and ERA5-Land agrees well with WUS-SR in both magnitude and correlation (Fig. 4.7a to 4.7c), with relative mean differences (*RMD*) of less than 3% in absolute

value and $R > 0.9$. While SNODAS overestimates SWE volume with a *RMD* of 14% (Figure 4.7a), it shows consistent interannual variations with a high *R* value of 0.92. The LR products are generally well correlated with WUS-SR with $R > 0.85$, although SWE_{peak} from these products is underestimated by as much as 190 km^3 (GLDAS-CLSM10), equivalent to a *RMD* of 71% compared to WUS-SR. Figure 4.7j shows that SWE percentiles computed from different products in the WUS are in better agreement in extreme years and in less agreement for near-average years. For example, WY 2017 was the wettest year among all products and WY 2015 was the driest year for all products except for SNODAS (in which WY 2005 is suspiciously low). WY 2014 was a normal-to-wet year with SWE_{peak} between the sixtieth and seventieth percentiles from GLDAS-NOAH025, MERRA2, GLDAS-NOAH10, and GLDAS-CLSM10, but a normal-to-dry year with SWE_{peak} less than the fiftieth percentile in the other products.

The interannual variability of SWE_{peak} is in much less agreement in the Andes (Fig. 4.8; with *R* as low as 0.56) than the WUS. Fig. 4.8 shows that ERA5-Land and MERRA2 are most consistent with Andes-SR in terms interannual variability ($R > 0.85$). However, ERA5-Land overestimates SWE_{peak} by 18 km^3 (*RMD* = 65%) and MERRA2 underestimates SWE_{peak} by 23 km^3 (*RMD* = -80%). Although ERA5 has the smallest *RMD* of 17%, the correlation coefficient *R* is 0.74, suggesting that SWE_{peak} from ERA5 is less representative of interannual variation in the Andes. For the GLDAS products, GLDAS-NOAH025 has $R = 0.79$, whereas *R* values for other GLDAS products at 1° are less than 0.65, indicating that SWE from these LR products are less consistent with the interannual variation from Andes-SR. Figure 8a illustrates that the SWE_{peak} percentiles computed from the common 12-year record are much less consistent in the Andes than in the WUS (shown in Fig. 4.7j) for both normal and extreme years. Despite good temporal correlation of SWE_{peak} (between 0.86 and 0.90) in WUS, the relatively poorer temporal

correlation (between 0.56 and 0.87) identified from the LR products in the Andes, indicates that they may be less suitable for trend or other analyses that require snow estimates with representative interannual variability.

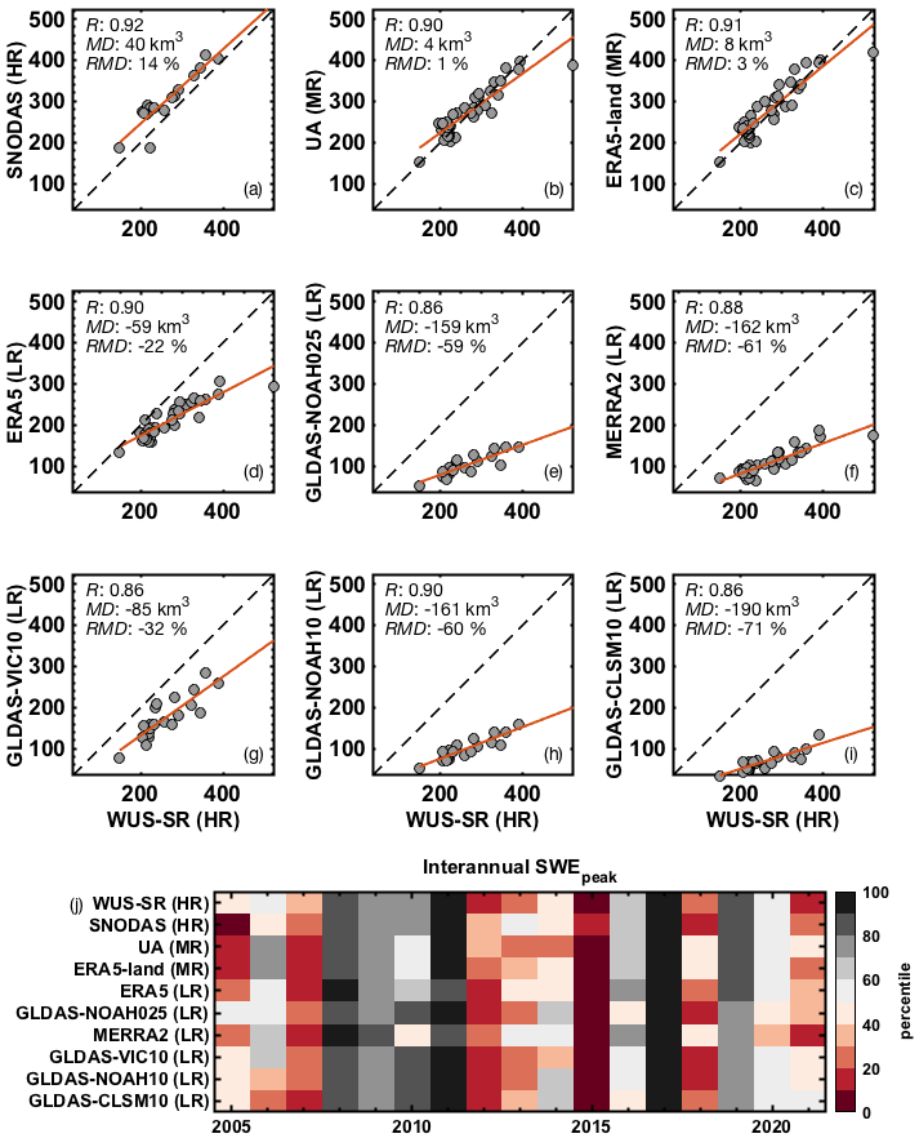

Figure 4.7 Scatter plots (a – i) of SWE_{peak} volumes between WUS-SR and other products. Each dot represents SWE_{peak} volume (km^3) for each year over the study period (WYs 1985 to 2021) where data is available. For the SNODAS and GLDAS products, the comparison is over WYs 2005 to 2021, and 2001 to 2021, respectively. (j) shows the SWE_{peak} percentiles in each WY over the overlapping period including all products (WYs 2005 to 2021).

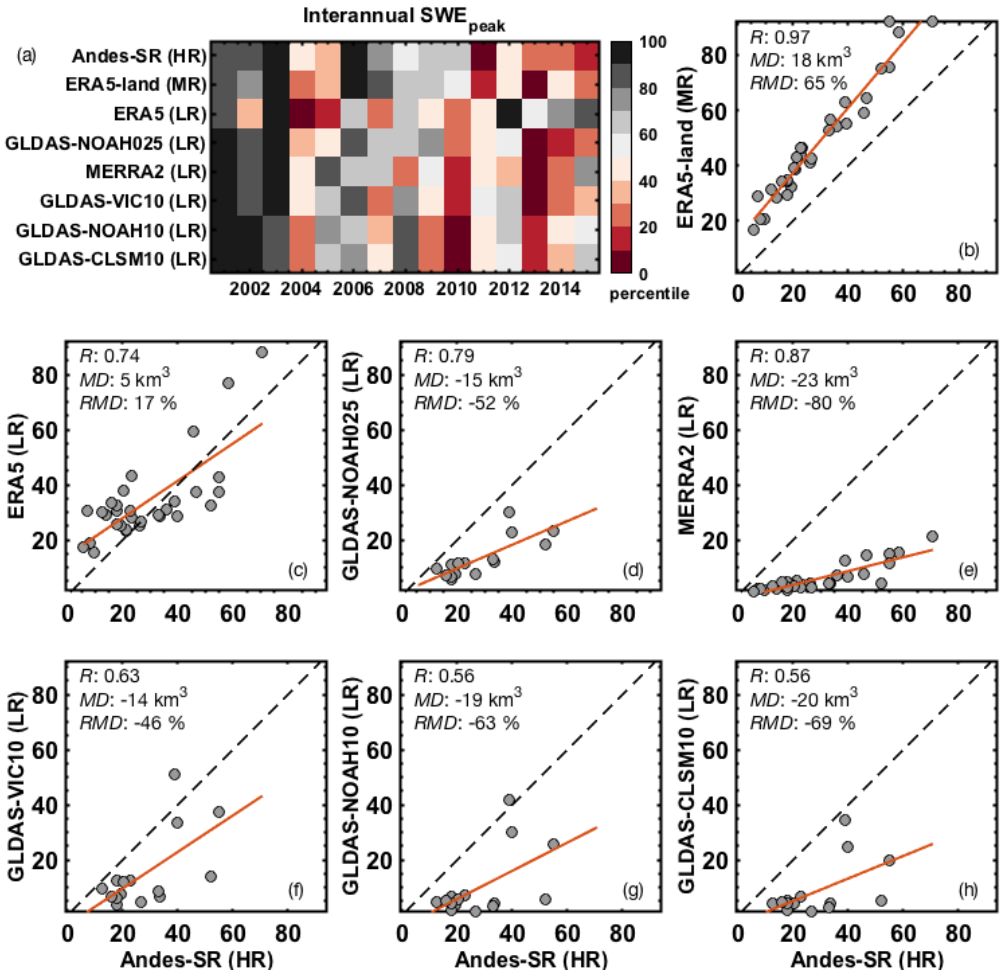

Figure 4.8 Scatter plots (b – h) of SWE_{peak} volumes between Andes-SR and other products. Each dot represents SWE_{peak} volume (km^3) for each year over the study period (WYs 1985 to 2015) where data is available. For the GLDAS products, the comparison is over WYs 2001 to 2015. (a) shows the SWE_{peak} percentiles in each WY over the overlapping period including all products (WYs 2001 to 2015).

4.4.3 Drivers of SWE uncertainty

4.4.3.1 Uncertainty in annual SWE_{peak} from accumulation-season precipitation and snowfall

To better understand the accumulation-season SWE_{peak} uncertainty driven by model inputs, the relationship among P_{acc}, S_{acc}, and SWE_{peak} is quantified for all products. The data

points are more clustered in the WUS (Fig. 4.9a, b) than those in the Andes (Fig. 4.9c, d). GLDAS-CLSM10 and MERRA2 tend to have lower P_{acc}, S_{acc} and therefore SWE_{peak} in both the WUS and Andes. ERA5-Land and ERA5, on the other hand, have higher P_{acc}, S_{acc} and SWE_{peak} in both domains. For rain-snow partitioning, UA (Fig. 4.9a) tends to have more S_{acc} over the WUS compared to the other products. Given similar S_{acc}, SNODAS (Fig. 4.9b) is inclined to generate higher SWE_{peak}. In the Andes, GLDAS-NOAH10 and GLDAS-CLSM10 partition less P_{acc} into S_{acc} with circles lower than the regression line, in contrast to ERA5-Land and ERA5 that tend to partition more (Fig. 4.9c). SWE_{peak} from ERA5-Land diverges from ERA5 (Fig. 4.9d) given similar amount of P_{acc} and S_{acc}, presumably caused by different melt amounts between the two products driven by resolution-induced elevation differences.

Annual values of P_{acc} and S_{acc} estimates from all products show that the variance in P_{acc} explains the majority of the variance in snowfall in the accumulation season with a coefficient of determination $R^2 = 0.55$ in the WUS (Fig. 4.9a) and $R^2 = 0.84$ in the Andes (Fig. 4.9c). This is consistent with previous findings (Broxton et al., 2016; Cho et al., 2022; Liu et al., 2022) and the expectation that precipitation is the major contributor to uncertainy in SWE. The lower R^2 in the WUS compared to the Andes suggests that other factors such as air temperature plays a more important role in rain–snow partitioning in the WUS. Approximately 49% of P_{acc} falls as snow in the WUS, whereas, around 75% of P_{acc} falls as snow in the Andes (Fig. 4.9a, c). This is because the Andes is at higher elevation (~2999 m) with cooler temperature than the WUS (~1383 m), leading to more precipitation falling as snow. The variance in SWE_{peak} is mostly explained by the variance in S_{acc}, i.e., $R^2 = 0.77$ in WUS (Fig. 4.9b) and $R^2 = 0.87$ in the Andes (Fig. 4.9d). As a fraction of cumulative snowfall, 65% and 75% remains as SWE_{peak} in the WUS and Andes, respectively, while the rest is lost to accumulation-season ablation.

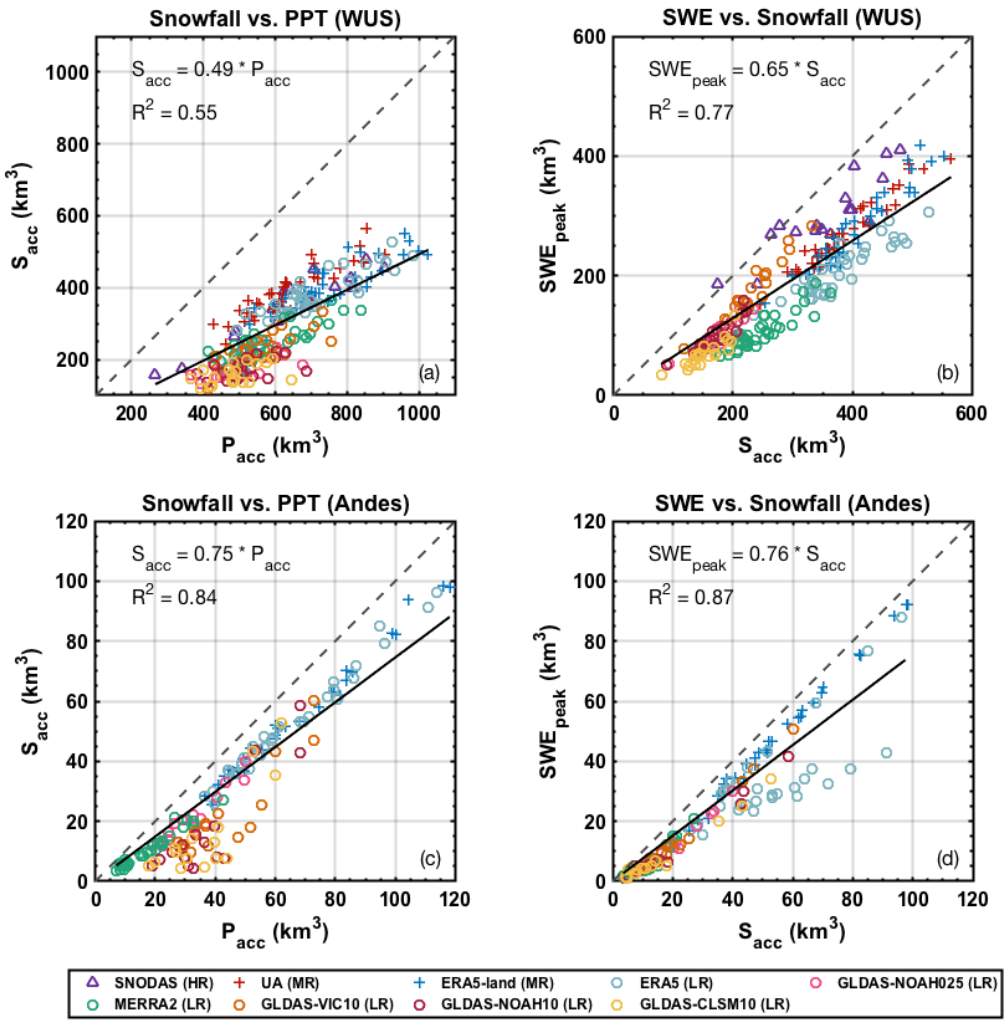

Figure 4.9 Left panels show scatter plots of accumulation-season S_{acc} (km^3) vs. P_{acc} (km^3) volumes over the WUS and Andes, respectively, indicating the partitioning of precipitation into snowfall. Right panels show scatter plots of accumulation-season SWE_{peak} (km^3) vs. S_{acc} (km^3) over WUS and Andes, respectively, indicating how much snowfall remains as SWE vs. being lost to ablation. Solid lines are linear regression and dashed lines are 1:1 lines.

4.4.3.2 Uncertainty in climatological SWE_{peak} from differences in LSMs and spatial resolution

To understand the impact of varying LSM mechanisms (i.e., rain–snow partitioning and snowmelt generation) and spatial resolution on the uncertainties in SWE, climatological

precipitation, snowfall, and SWE_{peak} for all products over the WUS and Andes are shown in Fig. 4.10. The rainfall to precipitation ratio (R_{acc}/P_{acc}, gray text) represents the impact of rain–snow partitioning mechanisms, and the ablation to snowfall ratio (A_{acc}/S_{acc}, black text) represents the impact of accumulation-season snowmelt mechanisms. It should be noted that different peak SWE days may impact R_{acc}/P_{acc} via the accumulation window, i.e., the shorter accumulation season in the GLDAS subset (associated with earlier peak SWE days, t_{peak}, Fig. 4.10 red symbol) has cooler average temperature, and thus lower R_{acc}/P_{acc}. However, no significant relationship was found between t_{peak} and R_{acc}/P_{acc}, suggesting that R_{acc}/P_{acc} is not sensitive to t_{peak}. The WUS, with relatively lower elevation, has higher precipitation in the form of rainfall and higher snowfall loss to ablation than the Andes at higher elevation. In the WUS, R_{acc}/P_{acc} ranges from 0.39 (UA) to 0.69 (GLDAS-CLSM10), and A_{acc}/S_{acc} ranges from 0.15 (SNODAS) to 0.56 (MERRA2). In the Andes, R_{acc}/P_{acc} ranges from 0.19 (ERA5-Land) to 0.57 (GLDAS-CLSM10), and A_{acc}/S_{acc} ranges from 0.13 (ERA5-Land) to 0.48 (GLDAS-CLSM10). Precipitation tends to fall more as snow in the HR, MR, and ERA5 products, whereas a higher fraction of precipitation falls as rainfall in the other products (GLDAS, MERRA2), even though lower P_{acc} are observed in both domains. The differences in melt mechanisms across product models further differentiate the A_{acc}/S_{acc}, and therefore SWE_{peak}.

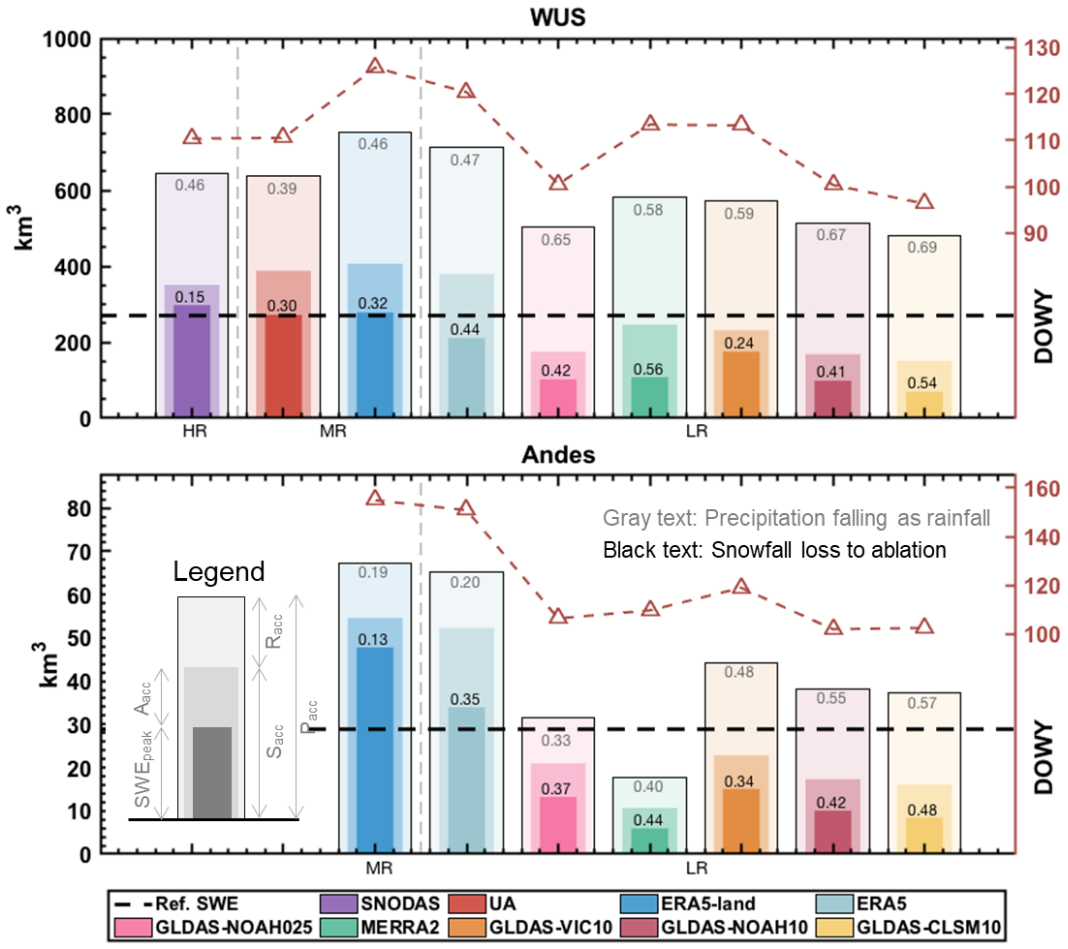

Figure 4.10 Climatological SWE_{peak}, S_{acc}, and P_{acc} volumes aggregated over WUS (top panel) and Andes (bottom panel) in km^3. Red triangles (corresponding to right y-axis) shows the t_{peak} averaged over all pixels and WYs. The horizontal dashed lines are the reference snow reanalysis SWE volumes from WUS-SR and Andes-SR. The vertical dashed lines group the products by spatial resolution (i.e., HR, MR, LR). The black text lists the A_{acc}/S_{acc} and gray text lists the R_{acc}/P_{acc}.

Accumulation-season snowfall and SWE_{peak} are sensitive to different rain–snow partitioning and snowmelt generation mechanisms across products. The same precipitation inputs (with only minor differences caused by downscaling) are used to derive GLDAS estimates at 1.0° from three different LSMs, making the GLDAS models a useful subset to understand the impact of LSM process representation on SWE estimates. Among the GLDAS subset at 1.0°,

R_{acc}/P_{acc} and A_{acc}/S_{acc} range from 0.59-0.69 and 0.24-0.54, respectively, in the WUS (Fig. 4.11a), and range from 0.48-0.57 and 0.34-0.48, respectively, in the Andes (Fig. 4.11b). Compared to R_{acc}/P_{acc}, a wider range of A_{acc}/S_{acc} values are observed in both the WUS and Andes, suggesting that snowmelt generation mechanism differences contribute more to the climatological SWE_{peak} uncertainties than the rain-snow partitioning differences. Given a similar amount of P_{acc}, GLDAS-VIC10 partitions the most into snowfall even with later peak days, whereas GLDAS-CLSM10 partitions the least in both domains. The differences in R_{acc}/P_{acc} are ≤ 0.1 between GLDAS-VIC10 and GLDAS-CLSM10, implying that the differences in snowfall caused by rain–snow partitioning is less than 10% of precipitation inputs among GLDAS subset at 1.0°. For A_{acc}/S_{acc}, GLDAS-VIC10 has the lowest ratio compared to others, suggesting that VIC snowfall loss to ablation is the least in this domain. GLDAS-VIC10 tends to have higher P_{acc}, S_{acc}, and SWE_{peak} which are closer to those from the HR or MR snow products. In the VIC model, elevation bands are used to better represent sub-grid snowfall and SWE estimates. In addition to GLDAS-CLSM10, which has the highest A_{acc}/S_{acc} among the GLDAS subset at 1.0°, MERRA2 has a comparably high A_{acc}/S_{acc}. Both products use the same LSM, suggesting that a larger portion of snowfall is lost as accumulation-season ablation in the Catchment model (Xiao et al., 2021).

Domains with larger variance in elevation are likely to be more sensitive to model spatial resolution, and therefore impact elevation-dependent mechanisms in the LSMs. ERA5-Land (0.1°) and ERA5 (0.25°) SWE are derived from the same LSM driven by similar forcings but modeled at different spatial resolutions. Similarly, GLDAS-NOAH025 (0.25°) and GLDAS-NOAH10 (1°) SWE are derived from the same Noah model driven by similar forcings but at two spatial resolutions. These two groups of products (Fig. 4.11c to f) are useful to isolate the impact

of spatial resolution on SWE estimates via differences in elevation representation. The raw DEMs from each product are used to compute the mean and standard deviation of elevation over WUS and Andes. The Andes located at higher elevation also has a larger variance in elevation (standard deviation > 1100 m) compared to the WUS (standard deviation < 800 m) across all resolutions. The standard deviation varies more significantly with resolution than the mean in both WUS and Andes (Fig. 4.11g, h). With coarser spatial resolution, the variance in elevation decreases, indicating that coarse-resolution products tend to underestimate the true variance in elevation. The differences in elevation variance between products are larger in the Andes than the WUS. For example, when increasing resolution of GLDAS from 1.0° to 0.25°, the standard deviation of elevation increases by 14% in the Andes compared to 8% in the WUS.

The R_{acc}/P_{acc} is similar in the ERA5-Land and ERA5 for the same domains (i.e., 0.47 from ERA5-Land and 0.46 from ERA5 in the WUS; 0.19 from ERA5-Land and 0.20 from ERA5 in the Andes), suggesting that the rain–snow partitioning in the ERA5 models is relatively insensitive to the elevation differences introduced by different spatial resolutions. The Andes is located at a higher elevation than the WUS, resulting in lower R_{acc}/P_{acc}. However, the A_{acc}/S_{acc} varies significantly between ERA5-Land and ERA5 in both WUS (0.32 vs. 0.44, respectively) and Andes (0.13 vs. 0.35, respectively). Hence, even though similar amounts of snowfall are generated for ERA5 and ERA5-Land, SWE_{peak} can be significantly different due to differences in ablation resulting from spatial resolution-based elevation differences. For GLDAS-NOAH025 and GLDAS-NOAH10, R_{acc}/P_{acc} and A_{acc}/S_{acc} are similar in the WUS. Large differences of both R_{acc}/P_{acc} and A_{acc}/S_{acc} are observed between GLDAS-NOAH025 and GLDAS-NOAH10. This suggests that increasing spatial resolution from 0.25° to 0.1° (ERA5) significantly impact snowmelt generation in both Andes and WUS, whereas increasing spatial resolution from to 1°

to 0.25° (GLDAS) impacts rain-snow partition and snowmelt generation only in Andes with its larger differences in elevation standard deviation between products at two spatial resolutions.

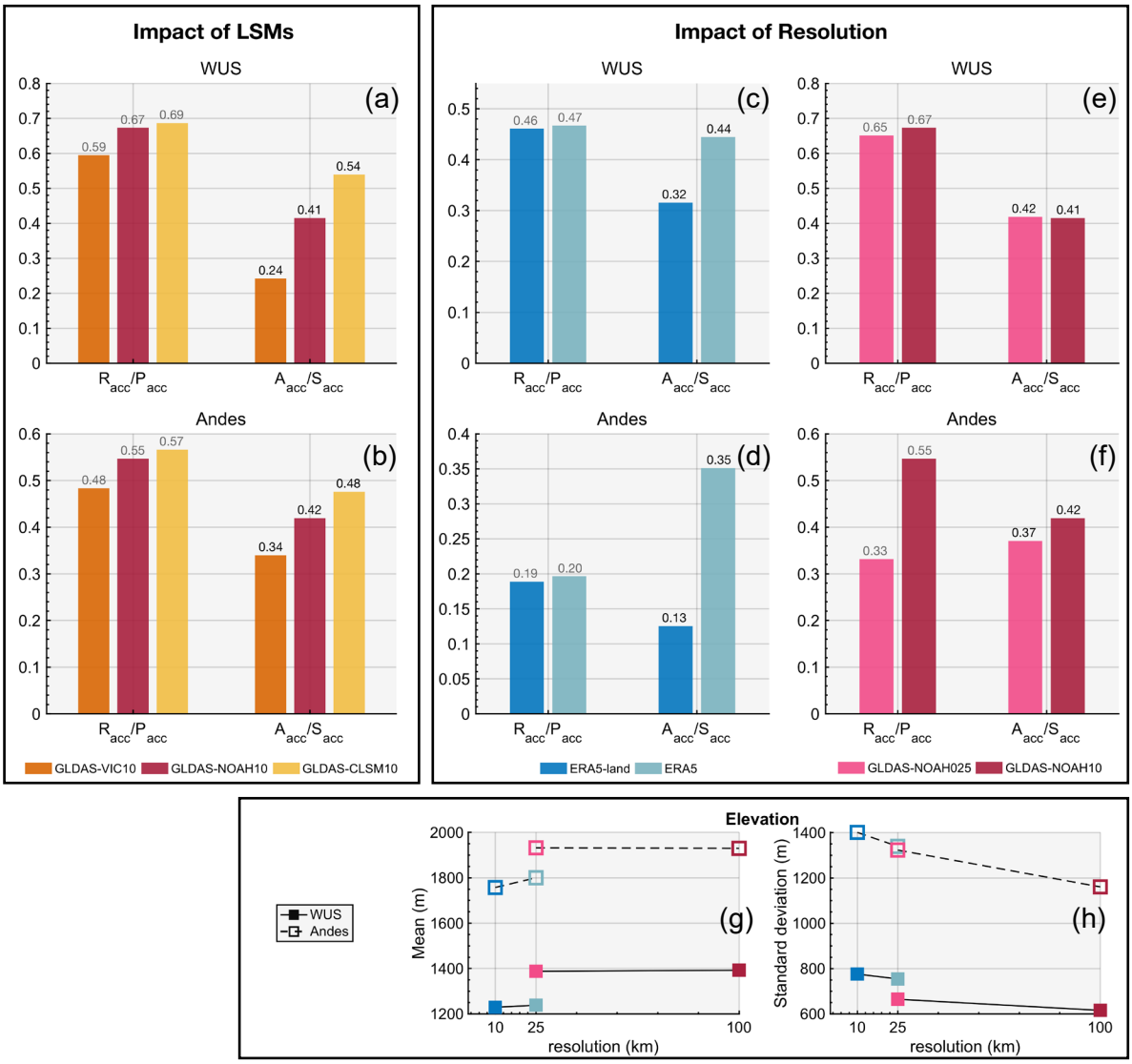

Figure 4.11 (a) and (b) R_{acc}/P_{acc} and A_{acc}/S_{acc} for three GLDAS LSMs (VIC, Noah, and Catchment) at the same spatial resolution (~ 100 km). (c) and (d) R_{acc}/P_{acc} and A_{acc}/S_{acc} for ERA5-Land (~ 10 km) and ERA5 (~ 25 km) using the same LSM and similar forcings, but different spatial resolutions. (e) and (f) Same as (c) and (d) but for GLDAS-NOAH025 (~ 25 km) and GLDAS-NOAH10 (~ 100 km). (g) and (h) mean and standard deviation of elevation over WUS and Andes from the ERA5-Land and ERA5 group, and the GLDAS-NOAH025 and GLDAS-NOAH10 group.

4.5 Conclusion

This paper quantifies the spatiotemporal snow storage uncertainty over the midlatitude American Cordillera (i.e., the WUS and Andes). These two domains are both snow-dominated areas sharing similar hydrometeorology, however, much less in situ measurements are available in the Andes compared with the WUS. The uncertainties of snow water storage, spatial patterns (including rainshadow effect), and interannual variability are analyzed among the HR (less than ~ 1 km), MR (between ~1 km to ~10 km) and LR (greater than ~10 km) snow products. The impact of forcings, LSM differences and spatial resolution on snow storage uncertainty is assessed to provide insights for generating future snow products especially for snow-dominated regions including areas with scarse in situ measurements.

With respect to characterizing climatological and interannual storage uncertainty, the key conclusions are:

1) In the WUS, HR and MR snow products are in better agreement with WUS-SR peak snow storage (269 km^3) than the LR snow products, among which snow storage is biased low with large uncertainty. The climatological snow storage was found to be 284 $km^3 \pm 14$ km^3 among HR and MR products and 127 $km^3 \pm 54$ km^3 among LR products. In the Andes, MR and LR products exhibit much larger relative uncertainty in snow storage. The Andes-wide peak snow storages are less clustered by spatial resolution with climatological estimates of 19 $km^3 \pm 16$ km^3 compared with peak snow storage of 29 km^3 from Andes-SR.
2) Beyond significant biases in overall storage, most of the global products poorly characterize snow storage variations related to orographically-induced rainshadow effects. Compared to the WUS-SR, only SNODAS and UA reasonably distribute snow storage over windward and leeward watersheds in the Sierra Nevada. MR and LR products partition less snow storage on

the windward side in both Sierra Nevada and Andes. In the Andes, global products show more snow water is stored on the leeward side of the mountain than the windward side, completely missing the orographic-rainshadow patterns. Based on these results, to accurately resolve topographically-driven features in snow storage likely requires spatial resolutions less than ~ 5 km.

3) Consistent interannual variability is observed among all products assessed in the WUS, whereas there is less agreement in the Andes. This suggests that snow trend studies based on these globally availably snow products applied in the Andes might not be as reliable as those applied in the WUS.

With respect to drivers of uncertainty in snow storage estimates, the key conclusions are:

1) Precipitation primarily explains the variance of snowfall as expected, which propagates to the variance of snow storage. Precipitation uncertainty accounts for a larger portion of snowfall uncertainty in the Andes compared with the WUS.
2) Aside from precipitation, LSM differences result in varying rain–snow partitioning and snowmelt generation, that play important roles in snow storage variance. Accumulation-season snowmelt generation mechanisms tend to contribute more to the climatological SWE_{peak} uncertainties than the rain–snow partitioning. When increasing spatial resolution, larger spatial variance in elevation between products in the Andes propagates to larger differences in precipitation falling as rainfall, snowfall loss to ablation, and thus SWE_{peak} than those in the WUS.

Data assimilation techniques are used to constrain the SWE uncertainties in SNODAS, UA, WUS-SR and Andes-SR. Moreover, many products are implicitly constrained by their use of in situ precipitation data in some form over the WUS. With more accurate precipitation

estimates in the WUS, products at HR to MR show reasonable estimates of SWE_{peak}. However, ERA5-Land (MR) and CR products miss the rainshadow effect (Section 4.4.1.2). SNODAS and UA generate high quality SWE estimates in the WUS via inclusion of in situ SWE measurements that are generally unavailable for regions like the Andes. Additionally, regions like Andes do not have sufficient in situ forcing measurements, resulting in a large uncertainty in forcings that propagates to SWE.

Although HR and MR products reasonably estimate snow storage in the WUS, uncertainty in snow storage from products at coarse spatial resolution in the WUS and at moderate and coarse spatial resolution in the Andes (where there are limited in situ measurements) need to be reduced to increase their utility for understanding the role of snow in regional water and energy cycling. For regional application, it is suggested to properly downscale global product to reduce the bias. Resolving orographic-rainshadow patterns is still a challenging task among existing products. Future work is needed to reduce the accumulation-season snow storage uncertainty for mountainous regions with limited in situ measurements. Beyond the accumulation-season processes focused on herein, the snowmelt uncertainty and its drivers in the melt-season should be investigated to further characterize additional uncertainty in warm-season snowmelt rates and timing. Aiming for resolving orographic-rainshadow patterns and generating reliable SWE estimates globally will likely require assimilation of space-borne snow observations. Specifically, future spaceborne missions that can directly provide SWE measurements at high to moderate spatial resolution over mountainous domains would be extremely valuable for constraining modeled estimates and generating continuous space–time SWE products at high accuracy over the globe.

4.6 Bibliography

Broxton, P. D., Zeng, X., & Dawson, N. (2016). Why Do Global Reanalyses and Land Data Assimilation Products Underestimate Snow Water Equivalent? *Journal of Hydrometeorology*, *17*(11), 2743–2761. https://doi.org/10.1175/JHM-D-16-0056.1

Cho, E., Vuyovich, C. M., Kumar, S. V., Wrzesien, M. L., Kim, R. S., & Jacobs, J. M. (2022). Precipitation biases and snow physics limitations drive the uncertainties in macroscale modeled snow water equivalent. *Hydrology and Earth System Sciences*, *26*(22), 5721–5735. https://doi.org/10.5194/hess-26-5721-2022

Cortés, G., & Margulis, S. (2017). Impacts of El Niño and La Niña on interannual snow accumulation in the Andes: Results from a high-resolution 31 year reanalysis. *Geophysical Research Letters*, *44*(13), 6859–6867. https://doi.org/10.1002/2017GL073826

Daly, C. (2006). Guidelines for assessing the suitability of spatial climate data sets. *International Journal of Climatology*, *26*(6), 707–721. https://doi.org/10.1002/joc.1322

Daly, C., Neilson, R. P., & Phillips, D. L. (1994). A Statistical-Topographic Model for Mapping Climatological Precipitation over Mountainous Terrain. *Journal of Applied Meteorology and Climatology*, *33*(2), 140–158. https://doi.org/10.1175/1520-0450(1994)033<0140:ASTMFM>2.0.CO;2

Dozier, J., Bair, E. H., & Davis, R. E. (2016). Estimating the spatial distribution of snow water equivalent in the world's mountains. *WIREs Water*, *3*(3), 461–474. https://doi.org/10.1002/wat2.1140

Fang, Y., Liu, Y., & Margulis, S. A. (2022). A western United States snow reanalysis dataset over the Landsat era from water years 1985 to 2021. *Scientific Data*, *9*(1), Article 1. https://doi.org/10.1038/s41597-022-01768-7

Huning, L. S., & AghaKouchak, A. (2020). Global snow drought hot spots and characteristics. *Proceedings of the National Academy of Sciences*, *117*(33), 19753–19759. https://doi.org/10.1073/pnas.1915921117

Huss, M., Bookhagen, B., Huggel, C., Jacobsen, D., Bradley, R. s., Clague, J. j., Vuille, M., Buytaert, W., Cayan, D. r., Greenwood, G., Mark, B. g., Milner, A. m., Weingartner, R., & Winder, M. (2017). Toward mountains without permanent snow and ice. *Earth's Future*, *5*(5), 418–435. https://doi.org/10.1002/2016EF000514

Immerzeel, W. W., Lutz, A. F., Andrade, M., Bahl, A., Biemans, H., Bolch, T., Hyde, S., Brumby, S., Davies, B. J., Elmore, A. C., Emmer, A., Feng, M., Fernández, A., Haritashya, U., Kargel, J. S., Koppes, M., Kraaijenbrink, P. D. A., Kulkarni, A. V., Mayewski, P. A., … Baillie, J. E. M. (2020). Importance and vulnerability of the world's water towers. *Nature*, *577*(7790), Article 7790. https://doi.org/10.1038/s41586-019-1822-y

Kim, R. S., Kumar, S., Vuyovich, C., Houser, P., Lundquist, J., Mudryk, L., Durand, M., Barros, A., Kim, E. J., Forman, B. A., Gutmann, E. D., Wrzesien, M. L., Garnaud, C., Sandells, M., Marshall, H.-P., Cristea, N., Pflug, J. M., Johnston, J., Cao, Y., … Wang, S. (2021). Snow Ensemble Uncertainty Project (SEUP): Quantification of snow water equivalent uncertainty across North America via ensemble land surface modeling. *The Cryosphere*, *15*(2), 771–791. https://doi.org/10.5194/tc-15-771-2021

Li, D., Wrzesien, M. L., Durand, M., Adam, J., & Lettenmaier, D. P. (2017). How much runoff originates as snow in the western United States, and how will that change in the future? *Geophysical Research Letters*, *44*(12), 6163–6172. https://doi.org/10.1002/2017GL073551

Liu, Y., Fang, Y., Li, D., & Margulis, S. A. (2022). How Well do Global Snow Products Characterize Snow Storage in High Mountain Asia? *Geophysical Research Letters*, *49*(16), e2022GL100082. https://doi.org/10.1029/2022GL100082

Liu, Y., Fang, Y., & Margulis, S. A. (2021). Spatiotemporal distribution of seasonal snow water equivalent in High Mountain Asia from an 18-year Landsat–MODIS era snow reanalysis dataset. *The Cryosphere*, *15*(11), 5261–5280. https://doi.org/10.5194/tc-15-5261-2021

Luojus, K., Pulliainen, J., Takala, M., Lemmetyinen, J., Mortimer, C., Derksen, C., Mudryk, L., Moisander, M., Hiltunen, M., Smolander, T., Ikonen, J., Cohen, J., Salminen, M., Norberg, J., Veijola, K., & Venäläinen, P. (2021). GlobSnow v3.0 Northern Hemisphere snow water equivalent dataset. *Scientific Data*, *8*(1), 163. https://doi.org/10.1038/s41597-021-00939-2

Mankin, J. S., Viviroli, D., Singh, D., Hoekstra, A. Y., & Diffenbaugh, N. S. (2015). The potential for snow to supply human water demand in the present and future. *Environmental Research Letters*, *10*(11), 114016. https://doi.org/10.1088/1748-9326/10/11/114016

Margulis, S. A., Cortés, G., Girotto, M., & Durand, M. (2016). A Landsat-Era Sierra Nevada Snow Reanalysis (1985–2015). *Journal of Hydrometeorology*, *17*(4), 1203–1221. https://doi.org/10.1175/JHM-D-15-0177.1

Margulis, S. A., Girotto, M., Cortés, G., & Durand, M. (2015). A Particle Batch Smoother Approach to Snow Water Equivalent Estimation. *Journal of Hydrometeorology*, *16*(4), 1752–1772. https://doi.org/10.1175/JHM-D-14-0177.1

Margulis, S. A., Liu, Y., & Baldo, E. (2019). A Joint Landsat- and MODIS-Based Reanalysis Approach for Midlatitude Montane Seasonal Snow Characterization. *Frontiers in Earth Science*, *7*, 272. https://doi.org/10.3389/feart.2019.00272

Molotch, N. P., & Bales, R. C. (2006). SNOTEL representativeness in the Rio Grande headwaters on the basis of physiographics and remotely sensed snow cover persistence. *Hydrological Processes*, *20*(4), 723–739. https://doi.org/10.1002/hyp.6128

NOHRSC. (2004). *Snow Data Assimilation System (SNODAS) Data Products at NSIDC, Version 1*. https://nsidc.org/data/g02158/versions/1

Nolin, A. W., Sproles, E. A., Rupp, D. E., Crumley, R. L., Webb, M. J., Palomaki, R. T., & Mar, E. (2021). New snow metrics for a warming world. *Hydrological Processes*, *35*(6). https://doi.org/10.1002/hyp.14262

Qin, Y., Abatzoglou, J. T., Siebert, S., Huning, L. S., AghaKouchak, A., Mankin, J. S., Hong, C., Tong, D., Davis, S. J., & Mueller, N. D. (2020). Agricultural risks from changing snowmelt. *Nature Climate Change*, *10*(5), Article 5. https://doi.org/10.1038/s41558-020-0746-8

Rhoades, A. M., Hatchett, B. J., Risser, M. D., Collins, W. D., Bambach, N. E., Huning, L. S., McCrary, R., Siirila-Woodburn, E. R., Ullrich, P. A., Wehner, M. F., Zarzycki, C. M., & Jones, A. D. (2022). Asymmetric emergence of low-to-no snow in the midlatitudes of the American Cordillera. *Nature Climate Change*, *12*(12), Article 12. https://doi.org/10.1038/s41558-022-01518-y

Saavedra, F. A., Kampf, S. K., Fassnacht, S. R., & Sibold, J. S. (2018). Changes in Andes snow cover from MODIS data, 2000–2016. *The Cryosphere*, *12*(3), 1027–1046. https://doi.org/10.5194/tc-12-1027-2018

Siirila-Woodburn, E. R., Rhoades, A. M., Hatchett, B. J., Huning, L. S., Szinai, J., Tague, C., Nico, P. S., Feldman, D. R., Jones, A. D., Collins, W. D., & Kaatz, L. (2021). A low-to-no snow

future and its impacts on water resources in the western United States. *Nature Reviews Earth & Environment*, *2*(11), Article 11. https://doi.org/10.1038/s43017-021-00219-y

Snethlage, M. A., Geschke, J., Ranipeta, A., Jetz, W., Yoccoz, N. G., Körner, C., Spehn, E. M., Fischer, M., & Urbach, D. (2022). A hierarchical inventory of the world's mountains for global comparative mountain science. *Scientific Data*, *9*(1), Article 1. https://doi.org/10.1038/s41597-022-01256-y

Wrzesien, M. L., Pavelsky, T. M., Durand, M. T., Dozier, J., & Lundquist, J. D. (2019). Characterizing Biases in Mountain Snow Accumulation From Global Data Sets. *Water Resources Research*, *55*(11), 9873–9891. https://doi.org/10.1029/2019WR025350

Xiao, M., Mahanama, S. P., Xue, Y., Chen, F., & Lettenmaier, D. P. (2021). Modeling Snow Ablation over the Mountains of the Western United States: Patterns and Controlling Factors. *Journal of Hydrometeorology*, *22*(2), 297–311. https://doi.org/10.1175/JHM-D-19-0198.1

CHAPTER 5

Conclusion and Future Work

5.1 Conclusion and key findings

The key contributions and findings for each Chapter are summarized as follows.

In Chapter 2 it was shown that:

1) An accurate high-resolution snow reanalysis dataset over the Landsat remote sensing record can be derived over the WUS using a Bayesian framework in which snow is estimated from land surface model coupled with snow depletion curve and updated by assimilation of cloud-free Landsat fractional snow-covered area observations.
2) The peak snow water equivalent (SWE) is well verified with independent in situ measurements with a WUS-wide correlation coefficient of 0.77, mean difference of –0.15 m, and root mean square difference of 0.28 m. It is well correlated with Airborne Snow Observatory (ASO) measurements with correlation coefficient ranging from 0.71 to 0.91. It is noteworthy that comparing point-scale measurements with grid-scale estimates is less fair than the comparison between spatially distributed estimates.
3) Considering the high-resolution (~ 480 m), temporal continuity (daily over 1985 to 2021), and coverage of the full WUS, the dataset can be used to characterize the variability and uncertainty of snow water storage.

In Chapter 3 it was shown that:

1) WY 2021 was a widespread low-snow year where over 40% of the snow-dominated WUS had snowmelt below the 30th percentile. However, WY 2021 stood out as an

unexpected year with extremely low streamflow compared to less extreme snow conditions in the Sierra Nevada (SN) and Upper Colorado River Basin (UCRB).

2) Over 75% of the in situ sites in the SN and UCRB had antecedent soil moisture drought, and a majority of the watersheds assessed had antecedent soil moisture drought in addition to snowmelt drought. The extreme 2021 streamflow drought was a compound event modulated by contributors linking snow, soil moisture, and streamflow.

In Chapter 4 it was shown that:

1) In the WUS, based on the climatological peak snow storage of 269 km^3 from WUS-SR, averaged snow storage from high- and moderate-resolution products are only overestimated by 6%, whereas averaged snow storage from low-resolution products is underestimated by 53%. In the Andes, the peak climatological snow storage of 29 km^3 from Andes-SR is underestimated by more than 35% from global products.
2) Mostly of the global datasets cannot resolve the orographically-induced rainshadow pattern in both WUS and Andes by partitioning too much snow storage on the leeward side of the mountain. A spatial resolution less than ~ 5 km is suggested to accurately resolve topographically-driven features in snow storage.
3) Although precipitation is the primary driver of snow uncertainty in the accumulation season, LSM mechanisms and coarse spatial resolution contribute to the uncertainty in snow water storage. Specifically, snow water storage is more sensitive to accumulation-season snowmelt-mechanisms than rain-snow partitioning. Domains with large spatial variance in topography (Andes) tend to be more sensitive to resolution than those with less spatial variance in topography (WUS).

5.2 Potential for Future Work

The high-resolution WUS-SR dataset provides a valuable tool to study snow-related research in the WUS. To extend the dataset derived in Chapter 2 to global mountains, potential research directions could include:

1) Forcing uncertainties from different sources such as MERRA2 and ERA5 on SWE estimates and the value of multi-forcings can be quantified to better represent a priori SWE uncertainty.
2) For domains highly impacted by clouds, the limited number of cloud-free nadir fSCA measurements increase the uncertainty of snow estimates. To constrain the snow uncertainty, multi-source fSCA measurements from Landsat, MODIS, Sentinel and VIIRS can be used to increase the number of cloud free fSCA images.
3) A multi-resolution scheme can be applied to resolve spatial distribution of SWE at topography with high variance at high resolution and vice versa.
4) The current snow reanalysis framework uses multi-year averaged forest cover. Instead, time-varying forest cover can be inputted to better reflect transient changes for snow-related studies sensitive to vegetation changes.
5) In addition to forest coverage and number of fSCA images, the impact of summer fire on snow uncertainty by changing the initial conditions can be investigated.

Based on the work in Chapter 3, future efforts to better quantify the contribution of snow to snow-streamflow droughts could include:

1) The data-centric study performed in Chapter 3 cannot fully quantify the contribution of all possible factors. Estimates from mechanistic modeling and downscaled climate simulations can be used to examine factors such as evapotranspiration for historical and

future drought types like WY 2021. Downscaled soil moisture data can be used to further examine the temporal evolution of soil moisture and its relationship with snowmelt.

2) Since the snow reanalysis dataset was only available up to 2021 by the time of this work, snow drought conditions in WY 2022 were not included. Extending the analysis to WY 2022 would be beneficial to understand the roles of snow and other factors on low streamflow in a consecutive dry year.
3) Under a warming climate, it is needed to quantify the frequency of drought types like WY 2021, which may significantly impact water resources management plans.

Based on quantifying the uncertainty of snow water storage and its drivers in Chapter 4, the following steps could be taken to improve the future snow estimates:

1) Large snow water storage uncertainty observed at coarse-resolution datasets in the WUS and all global datasets in the Andes need to be reduced, although snow water storage from high- and moderate-resolution datasets (< 10 km) agree with the WUS-SR.
2) The orographic-rainshadow patterns are completely missing from datasets greater than 5 km in both WUS and Andes. Resolving the patterns are required to correctly partition snow water storage between windward and leeward sides of mountain ranges for make right water resources decisions.
3) Snow water storage uncertainty and its drivers in the ablation season can be investigated for better estimating snowmelt timing and rate.

Aiming for resolving snow distribution over global mountains regardless of availability of in situ sites, snow assimilation using remote-sensed data provides a promising path forward. It would be beneficial to assimilate future spaceborne SWE measurements at high- to moderate-resolution to constrain snow estimates over the globe.

Appendix A

Supporting information for Characterizing snow-streamflow droughts in the Western U.S. and the unpredictable case of water year 2021

A.1 Aggregation window of snow metric

The aggregation window of snowmelt is chosen to be OCT to JUL. Diagnosing wet/dry years based on peak SWE or 1 April SWE can be misleading for WYs with dramatic changes in snow water conditions within a WY (e.g., Figure A.1a, WY 1991). The non-negligible snowmelt between multiple peaks and those that occur prior to 1 April may thus not be captured from single-day snow metrics (e.g., Figure A.1a, WY 2021). In the example years shown, a non-negligible amount of snowmelt and streamflow may occur prior to 1 April (Figure A.1b).

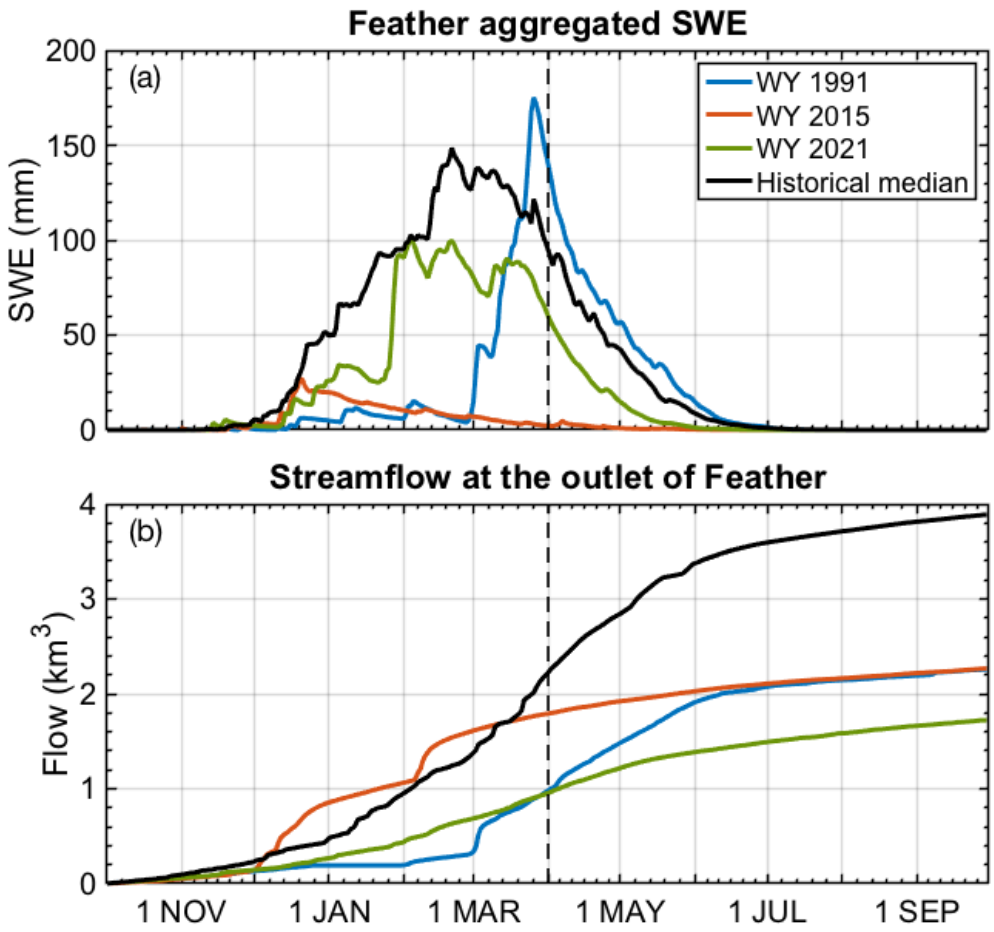

Figure A.1 (a) Seasonal SWE integrated across the Feather watershed in Water Years (WYs) 1991 (late peak), 2015 (early peak), 2021 (multi-peak) and the historical median. (b) Cumulative streamflow at the outlet of the Feather watershed across the same years. The dashed vertical lines represent the 1 April. Herein SWE and streamflow are analyzed over OCT-JUL since non-negligible snowmelt and streamflow can occur prior to 1 April (e.g., in WY 2015).

A.2 Datasets

Streamflow data is collected from the California Data Exchange Center (daily full natural flow) for sites in the SN, and from the United States Geological Survey (monthly adjusted streamflow volumes) for sites in Headwaters and Gunnison from the Snow Telemetry network (SNOTEL; Table A.1).

To illustrate the role of VWC in regulating snow contributions to streamflow, in situ VWC and SWE are collected at Forestdale (in SN) and Berthoud Summit (in UCRB) from SNOTEL/SCAN, and streamflow are collected at downstream sites from USGS (Table A.2).

Table A.1 Streamflow site information in SN and UCRB.

#	Site ID	Watershed	Lat	Lon	Station Name	Period with Data (WYs)
Naturalized daily streamflow in SN						
1	CLE	Trinity	40.801	-122.762	TRINITY LAKE	1987 - 2021
2	EXC	Merced	37.58500	-120.27000	NEW EXCHEQUER-LK MCCLURE	1989 - 2021
	ISB	Kern	35.64600	-118.47300	ISABELLA DAM	1988 - 2021
4	MKM	Upper Mokelumne	38.31300	-120.71900	MOKELUMNE-MOKELUMNE HILL	1989 - 2021
5	NAT	American	38.65000	-121.18300	LAKE NATOMA (NIMBUS DAM)	1988 - 2021
6	NML	Stanislaus	37.94810	-120.52500	NEW MELONES RESERVOIR	1988 - 2021
7	ORO	Feather	39.54000	-121.49300	OROVILLE DAM	1988 - 2021
8	PNF	Kings	36.83300	-119.32500	PINE FLAT DAM	1988 - 2021
9	SCC	Upper Tule	36.06100	-118.92200	SUCCESS DAM	1989 - 2021
10	SHA	Upper Sacramento	40.71876	-122.42112	SHASTA DAM (USBR)	1988 - 2021
11	SJF	San Joaquin	36.98439	-119.72431	SAN JOAQUIN RIVER BELOW FRIANT	1988 - 2021
12	TLG	Tuolumne	37.66600	-120.44100	TUOLUMNE R-LA GRANGE DAM	1985 - 2021
13	TRM	Kaweah	36.41500	-119.00200	TERMINUS DAM	1988 - 2021
14	YRS	Yuba	39.23517	-121.27412	YUBA RIVER NEAR SMARTVILLE	1988 - 2021
Naturalized monthly streamflow in UCRB						
15	CH (09095500)	Colorado Headwaters	39.23915	-108.26619	Colorado River Near Cameo	1985 - 2021
16	GR (09152500)	Gunnison	38.98332	-108.45064	Gunnison River Near Grand Junction	1985 - 2021
17	SJ (09379500)	San Juan	37.14695	-109.86484	SAN JUAN RIVER NEAR BLUFF	1985 - 2021
18	NF (09205000)	New Fork	42.56717	-109.93015	NEW FORK RIVER NEAR BIG PINEY	1985 - 2021
19	SR (09328500)	San Rafael	38.85000	-110.36667	SAN RAFAEL RIVER NEAR GREEN RIVER	1985 - 2021
20	WH (09306500)	White	39.96666	-109.16667	WHITE RIVER NEAR WATSON	1986 - 2021

Table A.2 Soil moisture and snow sites at Forestdale and Berthoud, and downstream streamflow sites.

Site name	Watershed	Source	Lat	Lon	Data
California					
Forestdale Creek (1049)	Upper Carson	SNOTEL	38.68245	-119.95970	VWC, SWE
Carson river at Woodfords (10310000)		USGS	38.76963	-119.83379	Streamflow
Colorado					
Berthoud Summit (335)	Colorado Headwaters	SNOTEL	39.80364	-105.77786	VWC, SWE
Fraser river near winter park (09022000)		USGS	39.83333	-105.75000	Streamflow

Appendix B

Supporting information for Spatiotemporal snow water storage uncertainty in the midlatitude American Cordillera

B.1 Description of products compared to WUS-SR and Andes-SR

B.1.1 HR product

SNODAS (NOHRSC, 2004) outputs daily SWE from WY 2004 at 1 km over CONUS. Although SNODAS is available starting from WY 2004, data assimilation was only regularly performed from WY 2005. Therefore, it is suggested to exclude SNODAS data in WY 2004 for analysis. SNODAS SWE is generated the from NOHRSC Snow Model, an energy and mass balance model forced with downscaled forcings from numerical weather prediction (NWP) models. Assimilation of ground-based snow data, airborne SWE from gamma radiation snow surveys, and satellite snow cover is performed via Newtonian nudging.

B.1.2 MR products

The UA daily SWE dataset (P. Broxton et al., 2019; Zeng et al., 2018) at 4 km over CONUS is generated from analysis and interpolation of in situ measurements including SWE from SNOTEL, snow depth, air temperature and precipitation from COOP stations, and gridded estimates including air temperature and precipitation from PRISM. The ordinary kriging method is used for interpolating the ratio of SWE to net snowfall at in situ sites to the PRISM grid. The interpolated ratio is then multiplied by gridded 4-km PRISM net snowfall to get gridded SWE. At in situ sites, precipitation falls as snow on days when snow depth change is positive. As a

result, snowfall may be overestimated on rain-on-snow days when both rainfall and snowfall occur, but precipitation is entirely recorded as snowfall. The temperature threshold to partition PRISM precipitation into snowfall and rainfall is interpolated from in situ threshold determined by each site (P. D. Broxton, Dawson, et al., 2016; P. D. Broxton, Zeng, et al., 2016). Net snowfall is estimated by the difference in accumulated snowfall and accumulated ablation which is a function of degree days above 0 °C. A new snow density parameterization (Dawson et al., 2017) was developed to convert snow depth at COOP stations to SWE. Precipitation and air temperature for UA are taken from PRISM (Daly et al., 1994).

ERA5 (Hersbach et al., 2020) outputs hourly SWE globally at 0.25° using the H-TESSEL model. An optimal interpolation (OI) method is used to update the grid-averaged snow depth from a maximum of 50 in situ measurements within a radius of 250 km from a given grid cell. In situ snow depth observations from SYNOP and GTS are used as assimilated measurements, and 4-km snow extent from NOAA/NESDIS is applied at elevation lower than 1500 m since 2004. However, SNOTEL/SCAN/COOP snow depth in the WUS are not currently used in the snow assimilation system. Though there might be some sparsely distributed in situ sites that measure snow depth which were assimilated in the WUS and Andes, the impact of data assimilation on SWE in both regions appears to be negligible. The binary snow extent is converted to snow depth at grids below 1500 m, assuming 5 cm of snow depth when snow cover is 1. The conversion is not conducted at elevations above 1500 m to avoid improper terrain information from coarse spatial resolution in mountainous area. SWE is set to 10 m at permanent snow and ice grids. Beyond snow observations, 4-km precipitation data from NCEP stage IV over the U.S. was assimilated in ERA5 using 4D var data assimilation method (Lopez, 2011). NCEP precipitation data is produced radar and gauge observations (Lin & Mitchell, 2005). Hence it is

reasonable to assume that ERA5 precipitation may be more accurate over the WUS than the Andes where such data is not assimilated.

B.1.3 CR products

ERA5-Land (Muñoz-Sabater et al., 2021) hourly SWE globally at 0.1° is generated from the same land surface model as ERA5 (with different versions) but driven by downscaled and lapse rate corrected forcings from ERA5 at higher spatial resolution. Specifically, shortwave, longwave, liquid, and solid precipitation are downscaled using a linear triangular mesh interpolation. Other variables such as air temperature, specific humidity, relative humidity, and surface pressure are adjusted to account for differences in elevations between the two spatial resolutions. No additional data assimilation is involved in generating the ERA5-Land SWE.

The suite of GLDAS 2.1 products consist of daily SWE since WY 2001 from four globally distributed products (Rodell et al., 2004). The four products are generated from three LSMs and at two spatial resolutions (i.e., Noah LSM at 0.25°: GLDAS – NOAH025; Noah LSM at 1.0°: GLDAS – NOAH10; VIC LSM at 1.0°; GLDAS –VIC10; Catchment LSM at 1.0°: GLDAS – CLSM10). The same meteorological forcings from multiple sources, including NOAA/GDAS, GPCP1.3, and corrected AGRMET, are employed to generate the four products. Adjustments for forcings are conducted to account for the elevation differences between GLDAS at 1.0° and 0.25°. No snow data assimilation is conducted in generating the products, whereas input forcings include sources from in situ measurements.

MERRA2 outputs hourly SWE globally at 0.625° x 0.5° resolution using the Catchment LSM (Reichle et al., 2017). The Catchment LSM is forced by bias-corrected precipitation using Climate Prediction Center (CPC) unified gauge-based analysis of global daily precipitation

products. Similar to the GLDAS set, no snow data assimilation is involved in generating the MERRA2 dataset, whereas in situ precipitation measurements are involved in deriving the SWE.

B.2 Domain masks, and persistent snow and ice masks

The domain masks (Figure B.1 and B.2, gray area) are derived based on the reference datasets (WUS-SR and Andes-SR) using an approach similar to Liu et al. (2022). Domain masks at reference resolutions are aggregated to the resolution used in each product.

The persistent snow and ice mask for WUS-SR is derived using the same method from Liu et al. (2021). If the annual minimum SWE of a pixel is greater than 10% of its annual maximum SWE more than once over the data period, the pixel is classified as a persistent snow and ice pixel. The persistent snow and ice for Andes-SR is from Landsat (Cortés & Margulis, 2017). The persistent snow and ice masks from reference datasets are then aggregated to the native resolution of each product (Figure B.1 and B.2, red area).

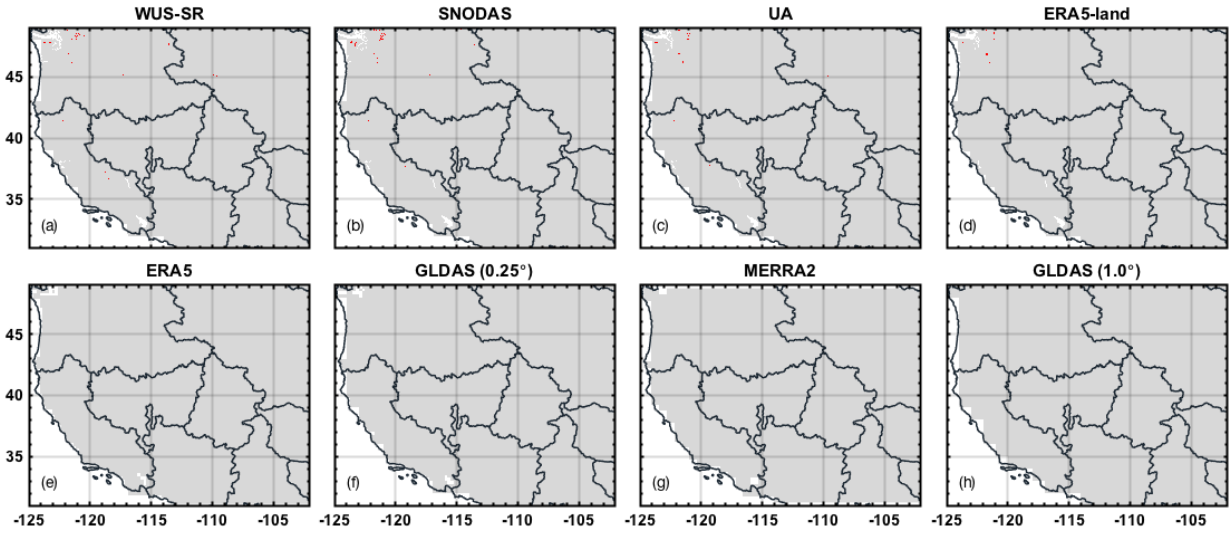

Figure B.1 WUS domain masks (gray) and glacier masks (red) for each product.

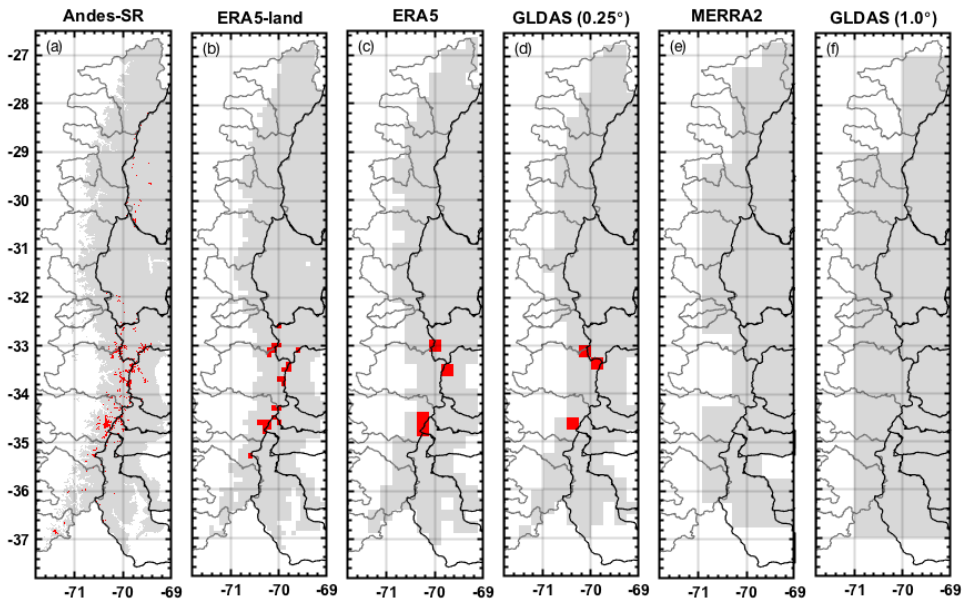

Figure B.2 Andes domain masks (gray) and glacier masks (red) for each product. For the Andes-SR, SWE was only estimated for locations above 1500 m.

B.3 Windward and leeward watersheds

For analysis related to windward-leeward SWE storage gradients, the analysis is applied at the relevant watershed scale. For moderate and coarse resolution products, a single pixel may be partially inside two different watersheds. To account for this, windward and leeward watershed masks are derived by intersecting the watersheds and product grids. For high resolution products (Andes-SR, WUS-SR and SNODAS), the centered coordinates of a pixel are used to determine if the pixel is inside a windward or leeward watershed. The fractional areas of pixel within the windward or leeward watersheds are shown in Figure B.3 and B.4.

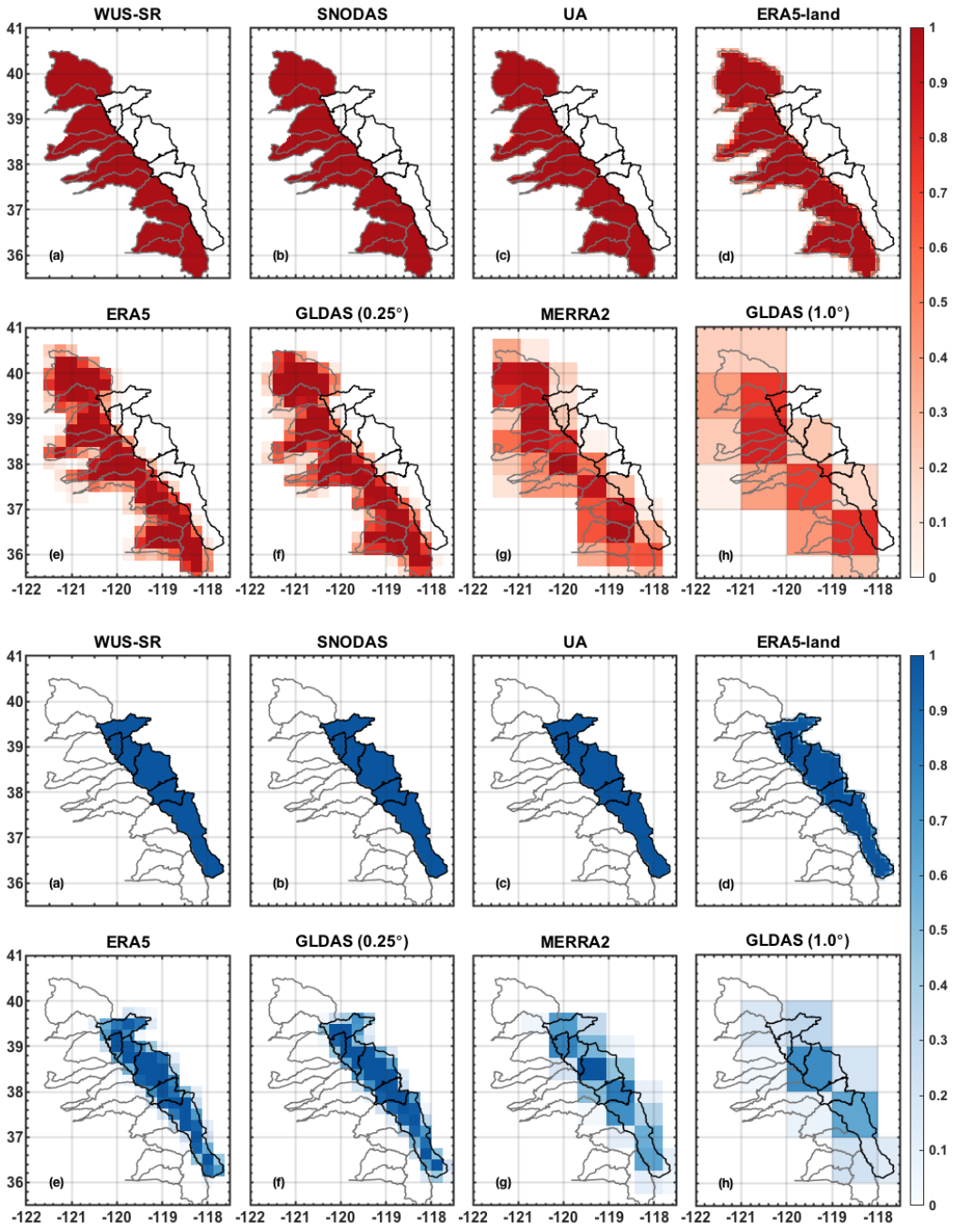

Figure B.3 Fractional areas of each native pixel covering windward (red) and leeward (blue) watersheds in the Sierra Nevada.

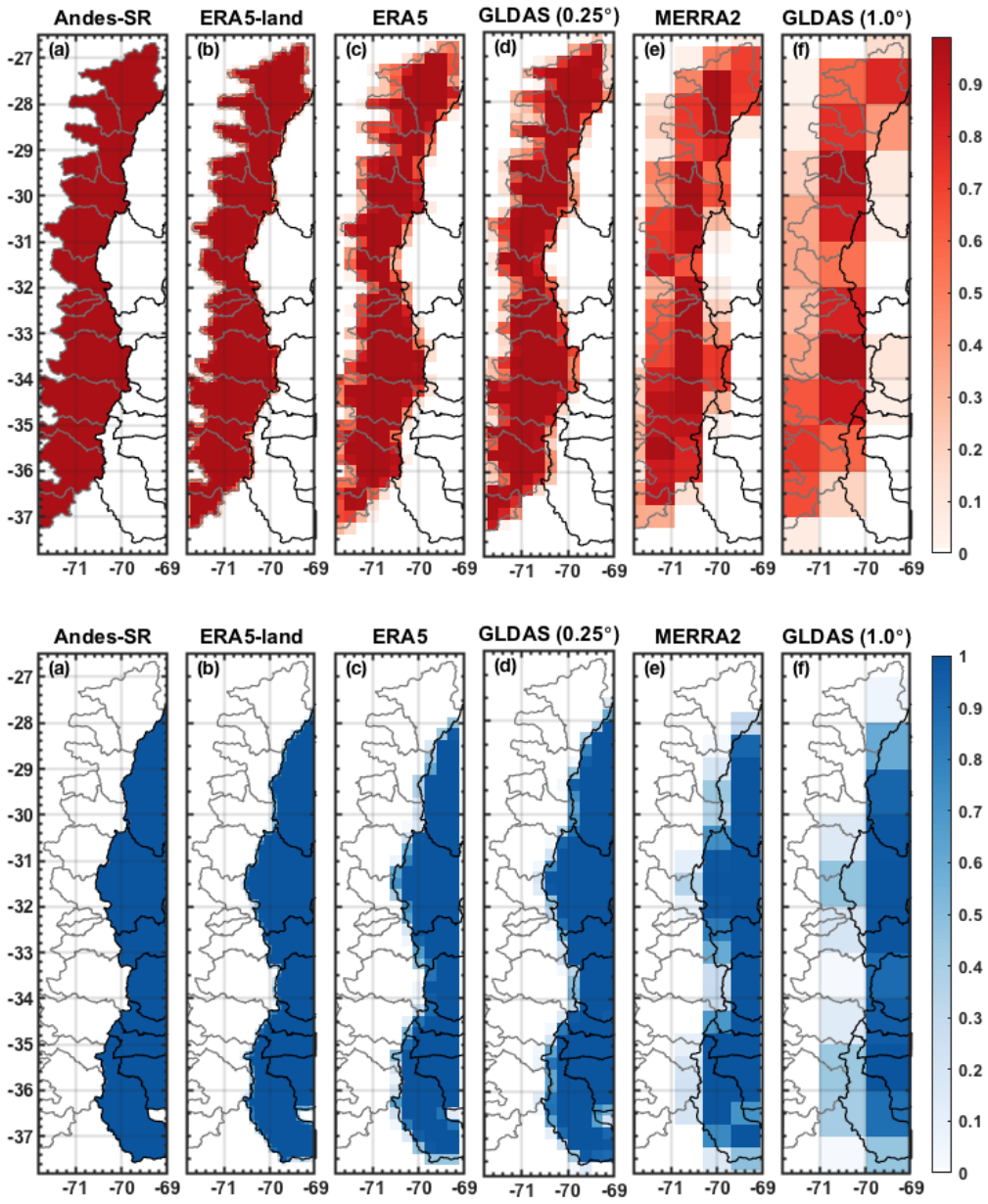

Figure B.4 Fractional areas of each native pixel covering windward (red) and leeward (blue) watersheds in the Andes.

B.4 Bibliography

Broxton, P. D., Dawson, N., & Zeng, X. (2016). Linking snowfall and snow accumulation to generate spatial maps of SWE and snow depth. *Earth and Space Science*, *3*(6), 246–256. https://doi.org/10.1002/2016EA000174

Broxton, P. D., Zeng, X., & Dawson, N. (2016). Why Do Global Reanalyses and Land Data Assimilation Products Underestimate Snow Water Equivalent? *Journal of Hydrometeorology*, *17*(11), 2743–2761. https://doi.org/10.1175/JHM-D-16-0056.1

Broxton, P., Zeng, X., & Dawson, N. (2019). *Daily 4 km Gridded SWE and Snow Depth from Assimilated In-Situ and Modeled Data over the Conterminous US, Version 1*. https://nsidc.org/data/nsidc-0719/versions/1

Cortés, G., & Margulis, S. (2017). Impacts of El Niño and La Niña on interannual snow accumulation in the Andes: Results from a high-resolution 31 year reanalysis. *Geophysical Research Letters*, *44*(13), 6859–6867. https://doi.org/10.1002/2017GL073826

Daly, C., Neilson, R. P., & Phillips, D. L. (1994). A Statistical-Topographic Model for Mapping Climatological Precipitation over Mountainous Terrain. *Journal of Applied Meteorology and Climatology*, *33*(2), 140–158. https://doi.org/10.1175/1520-0450(1994)033<0140:ASTMFM>2.0.CO;2

Dawson, N., Broxton, P., & Zeng, X. (2017). A New Snow Density Parameterization for Land Data Initialization. *Journal of Hydrometeorology*, *18*(1), 197–207. https://doi.org/10.1175/JHM-D-16-0166.1

Hersbach, H., Bell, B., Berrisford, P., Hirahara, S., Horányi, A., Muñoz-Sabater, J., Nicolas, J., Peubey, C., Radu, R., Schepers, D., Simmons, A., Soci, C., Abdalla, S., Abellan, X., Balsamo, G., Bechtold, P., Biavati, G., Bidlot, J., Bonavita, M., … Thépaut, J.-N. (2020).

The ERA5 global reanalysis. *Quarterly Journal of the Royal Meteorological Society*, *146*(730), 1999–2049. https://doi.org/10.1002/qj.3803

Lin, Y., & Mitchell, K. E. (2005). 1.2 the NCEP stage II/IV hourly precipitation analyses: Development and applications. *19th Conference Hydrology, American Meteorological Society*, *10*.

Liu, Y., Fang, Y., Li, D., & Margulis, S. A. (2022). How Well do Global Snow Products Characterize Snow Storage in High Mountain Asia? *Geophysical Research Letters*, *49*(16), e2022GL100082. https://doi.org/10.1029/2022GL100082

Liu, Y., Fang, Y., & Margulis, S. A. (2021). Spatiotemporal distribution of seasonal snow water equivalent in High Mountain Asia from an 18-year Landsat–MODIS era snow reanalysis dataset. *The Cryosphere*, *15*(11), 5261–5280. https://doi.org/10.5194/tc-15-5261-2021

Lopez, P. (2011). Direct 4D-Var Assimilation of NCEP Stage IV Radar and Gauge Precipitation Data at ECMWF. *Monthly Weather Review*, *139*(7), 2098–2116. https://doi.org/10.1175/2010MWR3565.1

Muñoz-Sabater, J., Dutra, E., Agustí-Panareda, A., Albergel, C., Arduini, G., Balsamo, G., Boussetta, S., Choulga, M., Harrigan, S., Hersbach, H., Martens, B., Miralles, D. G., Piles, M., Rodríguez-Fernández, N. J., Zsoter, E., Buontempo, C., & Thépaut, J.-N. (2021). ERA5-Land: A state-of-the-art global reanalysis dataset for land applications. *Earth System Science Data*, *13*(9), 4349–4383. https://doi.org/10.5194/essd-13-4349-2021

NOHRSC. (2004). *Snow Data Assimilation System (SNODAS) Data Products at NSIDC, Version 1*. https://nsidc.org/data/g02158/versions/1

Reichle, R. H., Draper, C. S., Liu, Q., Girotto, M., Mahanama, S. P. P., Koster, R. D., & Lannoy, G. J. M. D. (2017). Assessment of MERRA-2 Land Surface Hydrology Estimates. *Journal of Climate*, *30*(8), 2937–2960. https://doi.org/10.1175/JCLI-D-16-0720.1

Rodell, M., Houser, P. R., Jambor, U., Gottschalck, J., Mitchell, K., Meng, C.-J., Arsenault, K., Cosgrove, B., Radakovich, J., Bosilovich, M., Entin, J. K., Walker, J. P., Lohmann, D., & Toll, D. (2004). The Global Land Data Assimilation System. *Bulletin of the American Meteorological Society*, *85*(3), 381–394. https://doi.org/10.1175/BAMS-85-3-381

Zeng, X., Broxton, P., & Dawson, N. (2018). Snowpack Change From 1982 to 2016 Over Conterminous United States. *Geophysical Research Letters*, *45*(23), 12,940-12,947. https://doi.org/10.1029/2018GL079621